1-1-2017

Study Of Periodical Flow Heat Transfer In An Internal Combustion Engine

Xi Luo
Wayne State University,

Recommended Citation

Luo, Xi, "Study Of Periodical Flow Heat Transfer In An Internal Combustion Engine" (2017). *Wayne State University Dissertations*. 1840.
https://digitalcommons.wayne.edu/oa_dissertations/1840

STUDY OF PERIODICAL FLOW HEAT TRANSFER IN AN INTERNAL COMBUSTION ENGINE

by

XI LUO

DISSERTATION

Submitted to the Graduate School

of Wayne State University,

Detroit, Michigan

in partial fulfillment of the requirements

for the degree of

DOCTOR OF PHILOSOPHY

2017

MAJOR: MECHANICAL ENGINEERING

Approved By:

Advisor

ACKNOWLEDGMENTS

First of all, I would like to give my deepest and sincere gratitude to my advisor Prof. Marcis Jansons for his guidance and supports thought the years of my study and research. Without his wisdom, I could not be such success.

I would like to thank Prof. Naeim A. Henein, Prof. Ming-Chia Lai, and Prof. Mark Cheng for their service in my doctoral committee. Their valuable advices help me to improve my dissertation.

I would like to express my appreciation to all the members, Taewon Kim, David L. Gatti, Rachel E. Berlin-Allaire, Genan Ling, Andrew Abdulnour, Xin Yu, Alexander Meissner, Kan Zha, Jinqiao Wang, Alexander Davidson for their assistance with experiments. I also want to thank all the members of Center for Automotive Research Center for their help and support. I would also give my thanks to Prof. Chris. White, Dr. Ebadi, Alireza from University of New Hampshire for sharing their knowledge in turbulent theory.

I would like to acknowledge the technical and support from Automotive Research Center (ARC) in accordance with Cooperative Agreement W56HZV-04-2-0001, and U.S. Army Tank Automotive Research, Development and Engineering Center (TARDCE), US Department of Energy (DOE) Vehicle Technologies Office (VTO) and the National Science Foundation (NSF), Award No: CBET-1258594,.

Last but not least, I want to thank my family for their unconditional support during my study in the U.S.

TABLE OF CONTENTS

LIST OF FIGURES

LIST OF TABLES

CHAPTER 1 : MOTIVATION

Energy consumption is a foundation of human society, and it has a direct impact on the world economy. In addition, energy consumption has increased exponentially in the last century. In 2015, the US consumed 33,798 trillion Btu of energy [1], of which transportation consumed nearly 26%, as shown in Figure 1.1.

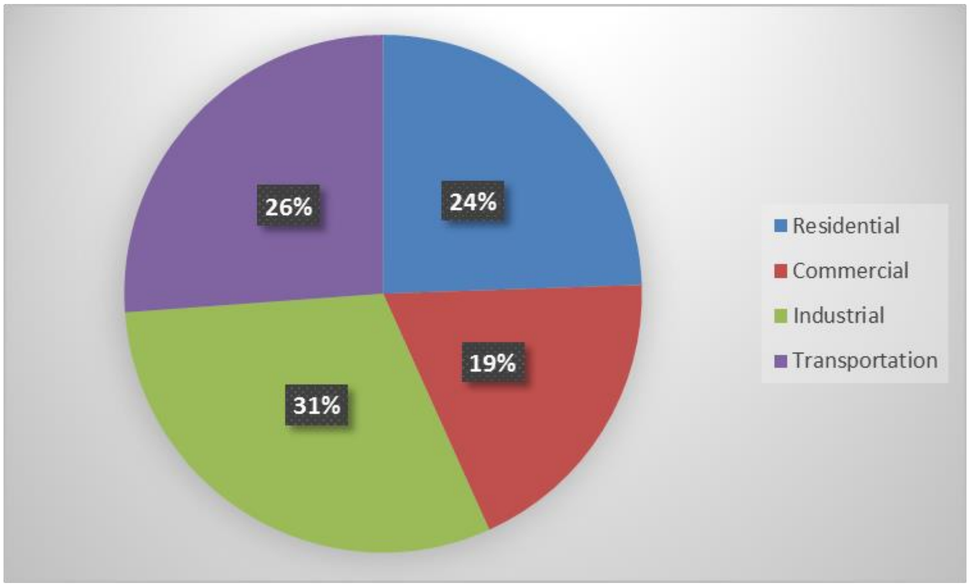

Figure 1.1: Energy consumption by sector using data provided by U.S. Energy Information Administration [1]

Also, fossil fuels have been the dominant source of energy for the last 150 years. In the US, petroleum, natural gas, and coal make up over 81% of total energy consumption, and the US Department of Energy (DOE) has predicted this number could remain at 76.6% in 2040 [2]. Figure 1.2 shows energy consumption by source in the US, from 1776 to 2015. It is interesting to note that the recent decline in petroleum usage had a direct relation to the economic crisis in 2008, and petroleum consumption recovered with the economy. In addition, natural gas has replaced coal to become the second largest energy source.

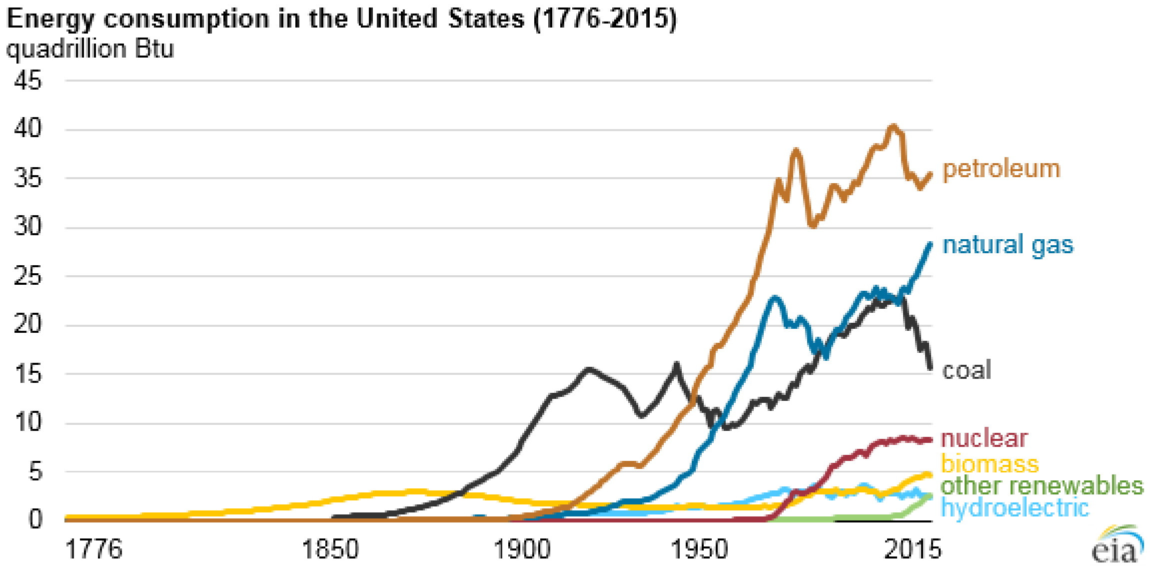

Figure 1.2: Energy consumption by source using data provided by U.S. Department of Energy [2].

The internal combustion (IC) engine is one of the main ways to convert the chemical energy in fossil fuels to mechanical work with great efficiency. However, the use of fossil fuels has created an impact on the environment which could affect human health. Therefore, emission regulation has become ever more stringent in recent years. Also, to counter global warming, carbon dioxide has been heavily regulated. As shown in Figure 1.3, with in next 10 years, the US government plans to reduce CO2 emission by 30%. Reducing emissions is a serious challenge for engine designers and researchers. To achieve this goal, it is essential to investigate engine behavior, and in-cylinder heat transfer is one of the most critical physical behaviors which has a direct influence on engine-out emission and thermal efficiency.

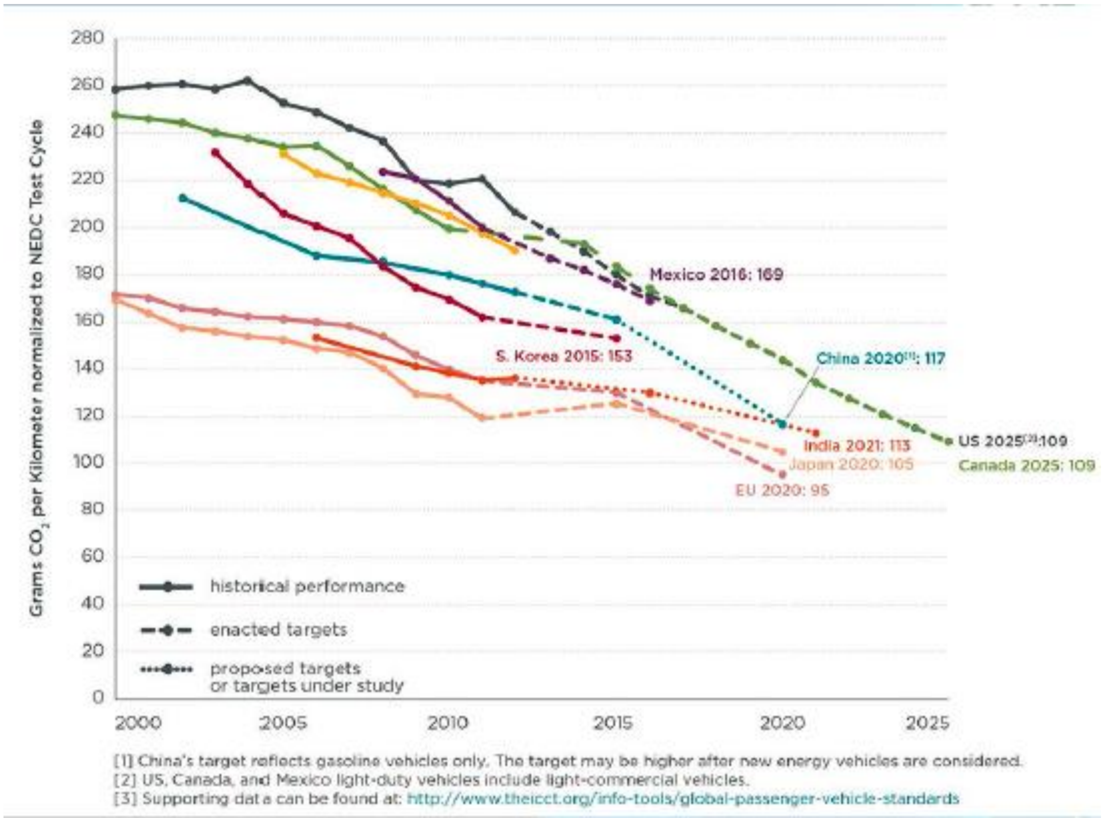

[1] China's target reflects gasoline vehicles only. The target may be higher after new energy vehicles are considered.
[2] US, Canada, and Mexico light-duty vehicles include light-commercial vehicles.
[3] Supporting data can be found at: http://www.theicct.org/info-tools/global-passenger-vehicle-standards

Figure 1.3: National CO2 emission reduction targets of major countries [3]

High wall temperature can reduce volumetric efficiency. The intake wall can increase the charge temperature, lowering density. Low air density limits the amount of mass flow into the cylinder. In the compression stroke, estimating gas-to-wall heat transfer becomes increasingly important because it influences the bulk gas temperature which affects the ignition delay for compression ignition (CI) engines and knock for spark ignition (SI) engines. For direct injection CI engines, ignition delay includes both physical delay and chemical delay. Heat transfer affects both. The fuel evaporation rate is directly proportional to the gas-liquid heat transfer rate. Droplet breakup, boiling heat transfer, and turbulent heat flux make the physical part of ignition delay extremely difficult to model. For the chemical part, gas temperature influences the chemical reaction rate exponentially. A 10% difference in bulk gas temperature can result in over a 100% difference in chemical reaction rate. It is also well known that end-gas heat transfer has a direct impact on knocking [4]. Therefore, heat transfer in the compression stroke greatly affects on engine performance for both SI and CI engines in terms of power and efficiency. The largest heat loss occurs during the combustion and expansion stroke. About 10%-15% of total fuel energy is lost during this period [5]. It is also very important to maintain the local maximum wall temperature under 175 °C because most motor oil can start to degrade at this temperature and stop providing lubrication [6]. In a worst case scenario, the motor oil can oxidize and form sludge, which may cause mechanical damage to the engine [6]. Also, engine designers utilize aluminum alloys for engine parts to reduce weight. However, aluminum alloys have much lower temperature resistance than steel. Also, wall temperature cannot be too cold. Low wall temperature results in higher UHC emission and more heat loss. Researchers have found out that the wall temperature has a strong impact on the flame structure, and low wall temperature can increase laminar flame quenching distance [7, 8]. However, most research is based on laminar flames. Turbulent boundary layer effects on flame quenching are not well understood. Therefore, wall temperature has to be precisely controlled to achieve high efficiency and low emission. However, this cannot be done without knowing gas-side heat flux.

CHAPTER 2 : BACKGROUND AND LITERATURE REVIEW

2.1 Introduction

Heat transfer in internal combustion is very complex. First, it varies from near zero to more than 10 MW/m^2 and back down again to near zero in a single engine cycle. Inside the engine cylinder, some areas are exposed to 100% more heat flux than other locations [9, 10], which creates a high-temperature gradient on the cylinder wall. Also, the pattern of heat transfer differs from cycle to cycle due to the effects of turbulence. In addition, the complex geometry and the turbulent flow with rapidly varying temperature and pressure make the environment challenging for modelers and researchers to study. However, the effects of heat transfer are too important for engine designers to ignore. Inside the engine cylinder, heat transfer is a function of convection, conduction, radiation, and energy generation. Conduction and energy generation can be relatively accurately analyzed and predicted by numerical solutions. However, many aspects of convection and radiation remain poorly understood.

2.2 General Equations and Definitions

At the micro level, temperature is a physical term to describe the kinetic energy of molecules, and this energy can be transferred by molecular motion and vibration in the process we call heat transfer. For conduction, the heat transfer per unit area, q''_{cd}, is given by:

$$q''_{cd} = -k\frac{\mathrm{dT}}{dx}$$

Equation 2.1

Where k is the thermal conductivity, and dT/dx is the temperature gradient. Thermal conductivity is a material property.

For engine heat transfer, conduction occurs through the cylinder head, wall, piston and other solid parts. On the other hand, convection occurs between a gas and a solid, and the convection heat transfer per unit of area, q''_{cv}, is given by:

$$q''_{cv} = h(T_g - T_w)$$

Equation 2.2

Where h is the convection coefficient, and T_g and T_w are the core gas and wall temperature, respectively. Unlike thermal conductivity, the convection coefficient is not only a function of molecular properties but also a function of the flow motion. In addition to convection and conduction, energy can also be transferred by radiation. The radiation heat transfer per unit of area, q''_r, is given by:

$$q''_r = \varepsilon\sigma(T_g^4 - T_w^4)$$

Equation 2.3

Where ε is emissivity of the wall, and σ is the Stefan-Boltzmann constant, $5.67*10^{-8}$ $W/m^2{\cdot}K^2$. In the engine, most radiation heat transfer occurs during combustion, and about one-third of heat lost in a diesel engine is through radiation [4], but some recent studies suggest that radiation heat loss is less than 1% of total engine heat loss [11]. The problem is that it is very hard to distinguish convection heat transfer and radiation heat transfer in experimental heat flux measurements. Therefore, in this study, convection experiments are executed under motored engine condition without combustion to eliminate radiation heat transfer.

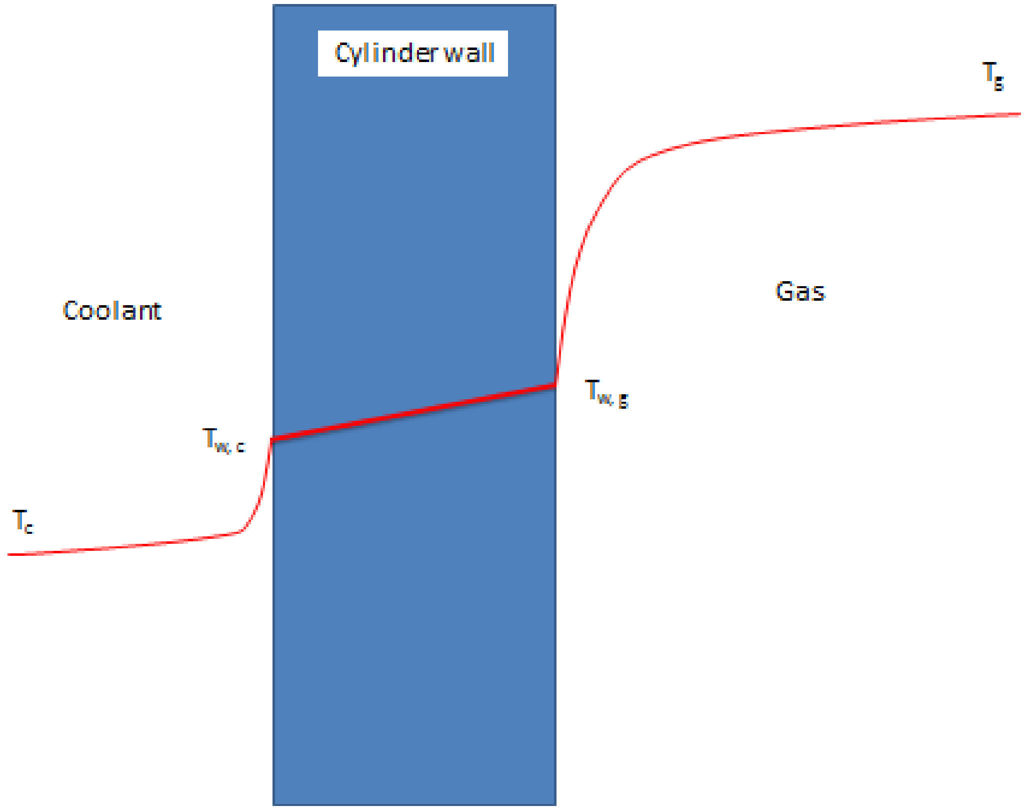

Figure 2.1: Diagram of in-cylinder temperature distribution

Figure 2.1 shows a one-dimensional heat flux transfer through the cylinder wall at a steady state. Researchers have discovered that one-dimensional heat flux applies to most areas of the engine cylinder, except the edge of the cylinder and piston bowl [5, 12-14]. On the coolant side, a convection coefficient is a large number, and the coolant carries out all the heat transfer from the wall almost instantly. It is a good assumption that the wall surface temperature on the coolant side is maintained at a constant temperature. On the other hand, heat transfer on the gas side is much more complex even for one-dimensional heat transfer.

2.3 Non-Dimensional Models

Researchers did experiments in a constant volume combustion bomb to study convection heat transfer in an engine. Based on such work, Annand has developed a description of the convection heat transfer coefficient [15]:

$$h = a(1 + 1.24c_m)\sqrt[3]{p^2T}$$

Equation 2.4

Where c_m is the mean piston speed, and P and T are the gas pressure and gas temperature, respectively. The value of "a" is 0.99 in the original paper [15]. However, later on, researchers found the value of "a" changes with the location inside the combustion bomb. Annand's model is based on the Nusselt formula [15], but the prediction can differ from the experimental result as much as 200%. Based on Annand's work, Woshchni developed a new model. Different than Annand, Woshchni did a total energy balance for the full engine cycle and assumed that the mean flow velocity is proportional to the mean piston speed [16]. Therefore, Woshchni proposed a non-dimensional convection heat transfer correlation [16]:

$$h = 110d^{-0.2}p^{0.8}T^{-0.53}[C_1c_m + C_2\frac{V_sT_1}{p_1V_1}(p - p_0)]^{0.8}$$

Equation 2.5

Where d is the diameter in meters of the engine piston, and p_0 is the cylinder pressure in bars when the engine is motoring. T_1, p_1, and V_1 are reference gas temperature, reference gas pressure, and reference volume, respectively. V_s is engine displacement volume. C_1 and C_2 are constant coefficients. Research has found that C1 equals 2.28 during compression and expansion, and 6.18 during the gas exchange; C_2 equals $3.24 \cdot 10^{-3}$ during combustion, and otherwise it equals 0 [4]. cm is mean piston speed. The Woshchni correlation is very important for understanding the general concept of in-cylinder heat transfer. It shows the relation between the convection coefficient and the in-cylinder primary gas properties, which are gas temperature, gas pressure, and flow speed. In addition, the Woshchni correlation also includes the combustion effects on convection heat transfer, and it is a popular method to estimate the engine total heat loss. In addition, some modifications have been made by other researchers to make better predictions for some of the more advanced combustion modes, such as HCCI, RCCI, and DI engine [10, 17-19]. However, the Woshchni correlation and its modifications does not include the local turbulence effects, which is the primary reason that the Woshchni correlation fails to predict the local heat transfer.

2.4 Boundary Layer & Law of the Wall

Boundary layer behavior has to be considered to predict the local heat transfer. The boundary layer exists in wall bounded viscous flow. Because of the viscosity, shear stress exists between the solid wall and flow. For non-slip incompressible flow, assuming a steady state condition, the total shear stress is given:

$$\tau(y) = \rho \nu \frac{d\bar{U}}{dy} - \rho \overline{u'v'}$$

Equation 2.6

Where u is the velocity parallel to the wall, and υ is velocity in the wall normal direction. ν and ρ are the kinematic viscosity and density of the working fluid. y is the distance in the normal direction. $\rho \nu \frac{d\bar{U}}{dy}$ is viscous stress, and $\rho \overline{u'v'}$ is Reynolds stress.

applying a non-dimension analysis, researchers have developed a scaling law to study the boundary layer. The wall shear stress is defined as:

$$\tau_w \equiv \tau(0) = \rho\nu(\frac{d\overline{U}}{dy})_{y=0}$$

Equation 2.7

Moreover, friction velocity is defined as:

$$u_\tau \equiv \sqrt{\tau_w/\rho}$$

Equation 2.8

Also, the viscous length-scale, δ_v is defined as:

$$\delta_v \equiv v\sqrt{\frac{\rho}{\tau_w}} = \frac{v}{u_\tau}$$

Equation 2.9

The distance from the wall using the viscous length-scale is given in wall units, which are defined as:

$$y^+ \equiv \frac{y}{\delta_v} = \frac{u_\tau y}{v}$$

Equation 2.10

Figure 2.2.2 shows structures for both the hydrodynamic boundary layer and the thermodynamic boundary layer. It is clear they are almost mirror images, different only in scale units. Where δ_T^+ and y_T^+ are defined as follows, respectively.

$$\delta_T^+ \equiv \frac{\delta_T U_\infty}{v}\sqrt{St}$$

Equation 2.11

$$y_T^+ \equiv \frac{yU_\infty}{v}\sqrt{St}$$

Equation 2.12

St is the Stanton number, and it is defined as:

$$St \equiv \frac{h}{\rho U_\infty c_p}$$

Equation 2.13

Hydrodynamic and thermodynamic boundary layers are coupled together in a turbulent flow. First, in the hydrodynamic boundary layer, the sublayer closest to the wall is the viscous sublayer where viscous stress is the main force acting on the flow. The viscous sublayer consists of two sections, which are linear sublayer and buffer layer. In the linear sublayer, viscous stress is the only force acting on the flow, and the thickness of the linear sublayer is a function of the surface friction coefficient Cf. For smooth surfaces, the thickness of the linear sublayer is found to be approximately $y^+ \approx 3$ [20]. In the buffer layer, the Reynolds stress begins to affect the flow.

The heat transfer closest to the wall is primarily driven by conduction. Similar to the hydrodynamic boundary layer, the sublayer closest to the wall is the conductive sublayer, and it has two sections, the linear sublayer and the thermal buffer layer. In the linear sublayer, the heat is transferred only by conduction heat transfer because flow acts more like a solid body when there is no fluid motion. When the Reynolds stress starts increasing in the buffer layer, the turbulent heat flux $< T'v' >$ also starts increasing, and both convection effects and conduction effects need to be considered in the buffer layers.

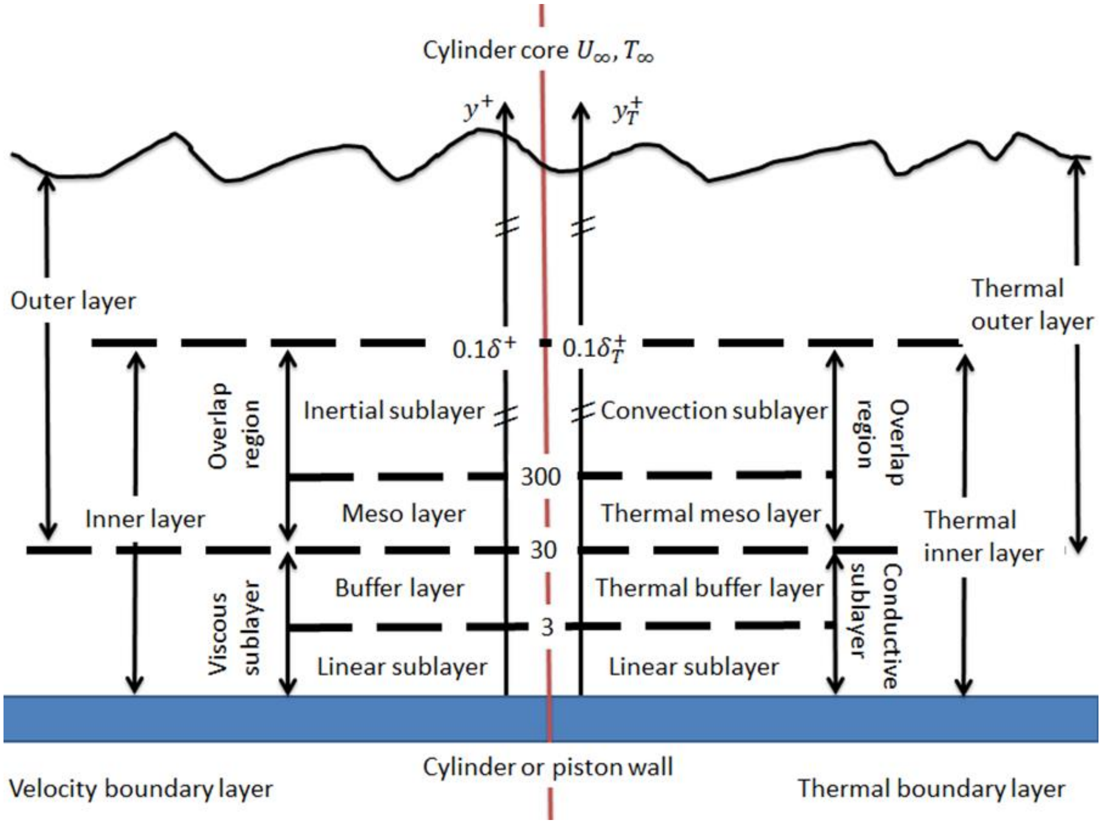

Figure 2.2.2: Schematic boundary layer

In the linear sublayer, by balancing the momentum for the steady state condition, the following equation can be obtained:

$$\rho\nu\left(\frac{d^2\overline{U}}{dy^2}\right) = 0$$

Equation 2.14

Integrating Equation 2.14 twice, the following equation can be obtained:

$$u^+ = y^+$$

Equation 2.15

Where u^+ is defined as:

$$u^{+} \equiv \frac{\overline{U}}{u_{\tau}}$$

Equation 2.16

For the thermodynamic boundary layer, a similar equation can be obtained near the wall:

$$k\left(\frac{d^{2}\overline{T}}{dy^{2}}\right) = 0$$

Equation 2.17

Integrating twice.

$$\theta^{+} = \frac{v}{\alpha} y^{+} = Pry^{+}$$

Equation 2.18

Where α is thermal diffusivity:

$$\alpha = \frac{k}{\rho c_{p}}$$

Equation 2.19

C_p is specific heat, and the θ^{+} is defined as:

$$\theta^{+} = \frac{T_{w} - \overline{T}}{T_{\tau}}$$

Equation 2.20

Where T_τ is the wall conduction temperature,

$$T_{\tau} = \frac{q_{w}''}{u_{\tau} \rho c_{p}}$$

Equation 2.21

Eq. 2.15 and 2.18 are matched well with experiments when $y^{+}<5$ [21]. However, it has a poor prediction in the buffer layer, where Equation 2.14 and Equation 2.17 are no longer valid. Beyond the buffer layer, there is a meso layer whose presence was experimentally confirmed in the early 1980s [22, 23]. In fact, it is a very important sublayer regarding physical phenomena. In the meso layer, viscous stress is small, and it has a negligible effect on mean momentum equations. However, viscosity still affects all turbulence scales of motion, and the meso layer effects can create two logarithmic regions rather than the classic one logarithmic region theory [24]. However, the meso layer effects can be weak for internal flow, such as pipe and channel flow. Beyond the meso layer, there are the inertial sublayer and convection sublayers for the hydrodynamic boundary layer and thermodynamic boundary layer, respectively. In the inertial sublayer, the flow is almost viscous free, and the velocity profile becomes independent of the Reynolds number. For a large Reynolds number, researchers have found that the temperature profile becomes independent of the Reynolds number, as the Reynolds number goes to infinity [25, 26]. The linear sublayer, buffer layer, meso layer, and inertial sublayer form an inner layer in which the total shear stress is practically constant. The outer layer is where the viscous stress's effect is negligible. For the inner sublayer, the mean velocity must satisfy the Prandtl law [27]:

$$\overline{U}(y) = u_\tau f(y^+)$$

Equation 2.22

In addition, for large Reynolds numbers, the outer layer must satisfy Karman's velocity defect law [28]:

$$\overline{U}_0 - \overline{U}(y) = u_\tau f_1(\frac{y}{\delta})$$

Equation 2.23

and:

$$\overline{U}_0 = u_\tau f_2(\frac{u_\tau \delta}{v})$$

Equation 2.24

f_1 *and* f_2 is out layer function and inner layer function. If the Reynolds number is large enough, an overlap layer could exist between the inner layer and the outer layer, as shown in Fig. 2.2, The following equation can be obtained from Eq. 2.23- Eq. 2.24:

$$f(y^+) + f_1\left(\frac{y}{\delta}\right) = f_2(\frac{u_\tau \delta}{v})$$

Equation 2.25

This equation was first obtained by Karman [29]. The general solution follows:

Inner layer scale: $f(y^+) = Aln(y^+) + B$

Outer layer scale: $f_1(\eta) = -Aln(\eta) + B_1$

Intermediate layer scale: $f_2(\zeta) = Aln(\zeta) + B + B_1$

Equation 2.26

Where A=1/ꝁ, and ꝁ is the Karman constant and has a valve ꝁ=0.41. B = 5.2 according to Cole’s work [30]. B_1 is 2.35 for flat plate flow and 0 for pipe or channel flows [31]. η is Outer layer scale. ζ is intermediate layer scale. In addition, more recent experimental results have suggested that the value of ꝁ can be as low as 0.38 [32] and as high as 0.45 [33]. One researcher even suggested ꝁ=1/e [34]. Therefore, the log law can be obtained by substituting the first equation of Eq. 2.27 back to Eq. 2.23:

$$u^+ = Aln(y^+) + B$$

Equation 2.27

Eq. 2.28 and 2.16 are known as the Law of the wall for velocity profiles. For temperature profiles, the law of the wall was first obtained by Kader and Yaglom in the 1970s [31]. They applied the Prandtl -Nikuradse skin friction law to the the pipe and channel flow. For thermodynamics, using similar laws, the thermal diffusion equation was obtained:

$$\overline{T_w} - \overline{T(y)} = T_\tau g(y^+, Pr)$$

Equation 2.28

The thermal diffusion law was first obtained by Squire in the 1950s [35]. In addition, the outer layer must satisfy the thermal defect law:

$$\overline{T_\infty} - \overline{T(y)} = T_\tau g_1(\frac{y}{\delta_T})$$

Equation 2.29

$$\overline{T_w} - \overline{T(y)} = T_\tau g_2(y^+, Pr)$$

Equation 2.30

Similar to the hydrodynamic boundary layer, for large Reynolds and Peclet numbers, an overlap layer can exist between the inner and outer layers; therefore, using Eq. 2.29-2.31, the following equation can be obtained:

$$g(y^+, Pr) + g_1\left(\frac{y}{\delta_T}\right) = g_2(y^+, Pr)$$

Equation 2.31

The general solution of this equation can be written as:

Inner layer scale: $g(y^+) = {C_A}^* ln(y^+) + \beta(Pr)$

Outer layer scale: $g_1(\eta) = -{C_A}^* ln(\eta) + \beta_1$

Intermediate layer scale: $g_2(\zeta) = {C_A}^{*} ln(\zeta) + \beta(Pr) + \beta_1$

Equation 2.32

Where $C_A = Pr/ꝁ$, and finally submit the Eq. 2.33 back to Eq. 2.29, the law of the wall for thermodynamics can be written as:

$$\theta^{+} = {C_A}^{*} ln(y^{+}) + \beta(Pr)$$

Equation 2.33

It is important to know there is a difference in the condition to satisfy the law of the wall of thermodynamics and hydrodynamics. The equilibrium of the turblent kinetic energy does not guarantee thermal equilibrium, and the thermodynamic law of the wall requires both equilibriums, which means the thermodynamic log law has more restrictions. This Reynolds-analogy is used by many engine modelers [36-40], and it may create some error for gas-side heat flux predictions. In fact, many modelers have begun to develop new scaling laws for the thermodynamic boundary layer [41, 42]. Although most of the development is based on pipe/channel flow, those newly developed scaling law could be useful for engine simulation.

2.5 Universal or Non-universal?

For a long time, the Law of the Wall was said to be universal, which means the velocity profile/temperature profile with over lap region is “unique”, and it is independent form follow parameters, such as Re number. In other word, the $u^{+} or\ \theta^{+}$is only functions of y^{+}in the over lap region. However, many researchers have had different opinions in the last 20 years. The controversy between the log law and the power law remain inconclusive. The power law is given as:

$$u^+ = C * (y^+)^a$$

Equation 2.34

Where C and α are coefficients depending on the Reynolds number, and for pipe flow;

$$C = 0.7053 \ln(Re) + 0.3055$$

Equation 2.35

$$a = \frac{1.085}{\ln(Re)} + \frac{6.535}{\ln(Re)^2}$$

Equation 2.36

Equation 2.35 and Equation 2.36 were first developed by Zagarola, Perry, and Smits in 1997 [43]. In terms of the velocity profile, the differences between the log law and the power law are small, about 5% [43-45]. However, the power law is a non-universal solution, because the power solution depends on follow's Reynolds number as shown in Equation 2.35 and Equation 2.36. Power law can have 25% error in terms of predicting wall shear stress [45]. This inconsistency has led to many discussions and studies in the past 20 years. Although the argument remains, some conclusions can be obtained. A universal log profile does exist in a pipe flow and a channel flow, and has better agreement with experimental results at extremely large Reynolds numbers [33, 46]. On the other hand, the power law theory is more logical with fewer assumptions, and it has better agreement with experimental results for the turbulent boundary layer that develops along a flat plate [34, 43, 47]. In addition, there is evidence that shows the log law also applies to developing boundary layers [32]. For pipe flow, the logarithmic overlap region is about $500<y^+<0.1\delta$, and the Power-law region is about $40<y^+<0.1\delta$ [43]. In other words, the Power-law region covers the meso layer, where the log law may not be valid. In terms of practical use, the log law has more advantages for numerical simulation because of the universal solution. On the other hand, the principles of the power law are useful for studying the effects of pressure gradient [48, 49]. As discussed above, there is no clear winner between the power law and the log law, and this work is not about which one is correct. In fact, we can expect that neither the log law or the power law is valid in the engine, because of the flow's complexity. However, it is worth proving or disproving the existence of the universal boundary layer to contribute to understanding of the basic phenomenon of engine flow.

2.6 Reynolds-Analogy

The similarities between flow momentum and fluid temperature pose a hypothesis that velocity and temperature have similar distributions in the boundary layer. In fact, Reynolds has postulated an analogy between wall shear and heat flux [50]. The Reynolds analogy is stated as:

$$\frac{|q_w|}{\tau_w} = \frac{k}{\mu}\left|\frac{dT}{du}\right|_w$$

Equation 2.37

We can rewrite Equation 2.37 in terms of the dimensionless coefficient:

$$\frac{2St}{c_f} = \frac{1}{Pr}\frac{(T - T_w)/(T_\infty - T_w)}{u/U_\infty}$$

Equation 2.38

Where c_f is the skin friction coefficient and Pr is the Prandtl number. For Pr=1, Equation 2.38 can be reduced to

$$\frac{2St}{c_f} = 1$$

Equation 2.39

Although the exact equation is rarely used today, an extended Reynolds analogy is more commonly used. An expression for c_f can be stated as [51]:

$$c_f = \frac{0.664}{Re_x^{1/2}}$$

Equation 2.40

Moreover, for constant wall temperature, the Stanton number, St can be expressed as:

$$St = \frac{0.332}{Re_x^{1/2} Pr^{2/3}}$$

Equation 2.41

Combining Equation 2.40 and Equation 2.41, the following expression can be obtained for zero pressure gradient, and it is often referred as the extended Reynolds analogy or the Colburn relation [52].

$$\frac{2St}{c_f} = \frac{1}{Pr^{2/3}}$$

Equation 2.42

In Equation 2.42, the Reynolds number is canceled out. Therefore, the Reynolds analogy is independent of the Reynolds number, and it has been proved by experimental results[53]. This physical phenomenon reflects a universal law of the wall to some degree. Although the Reynolds analogy factor increase with the positive pressure gradient, the idea that heat flux is an analogy to momentum flux is used in many studies [41, 54, 55]. However, the Reynolds analogy has been found to be invalid under reverse flow conditions [56]. Also, recent PIV and CFD results have proved the existence of reverse flow at the expansion stroke and gas exchange period in an engine cylinder [57, 58]. Thus, validation of the Reynolds analogy for engine flow is questionable.

2.7 Near Wall Treatment in CFD

Engine designers and researchers need a way to accurately predict spatial gas-side heat flux. Multidimensional numerical simulation is the most promising way to solve this problem. In fact, direct numerical simulation (DNS) can predict spatial gas-side heat flux, but it is simply too computationally expensive to have any practical use even with the availability of supercomputers. Other than DNS, the most widely used numerical simulation methods are large eddy simulation (LES) and Reynolds Averaged Navier-Stokes (RANS). Both methods require solving the Navier-Stokes equations. For an IC engine, the in-cylinder flow speed is on the order of 10 m/s. Therefore, it is a low-Mach number flow. The instantaneous governing equations for low-Mach number flow include the continuity equation (Equation 2.43), the momentum equation (Equation 2.44), and the energy equation (Equation 2.45) [59].

$$\frac{\partial \rho}{\partial t} + \frac{\partial}{\partial x_i}(\rho u_i) = 0$$

Equation 2.43

$$\frac{\partial (\rho u_i)}{\partial t} + \frac{\partial}{\partial x_j}(\rho u_i u_j + p\delta_{ij} - 2\mu S^*{}_{ij}) = 0$$

Equation 2.44

$$\frac{\partial (\rho T)}{\partial t} + \frac{\partial}{\partial x_j}(\rho T u_j + u_j p - \alpha \frac{\partial T}{\partial x_j} - 2\mu u_i S^*{}_{ij}) = 0$$

Equation 2.45

Where p and ρ pressure and density. u_i is instantaneous velocity in the x_i direction. μ is dynamic viscosity, and δ_{ij} is the Kronecker delta. The strain rate is defined as follows:

$$S^*{}_{ij} \equiv \frac{1}{2}\left(\frac{\partial u_i}{\partial x_j}+\frac{\partial u_j}{\partial x_i}\right)-\frac{1}{3}\frac{\partial u_k}{\partial u_k}\delta_{ij}$$

Equation 2.46

However, because of the nature of the boundary layer, the dynamic motions and length scale become much smaller as the Reynolds number increases. For Equation 2.45 to resolve the “inner” boundary layer, the required grid number $N \propto {Re_L}^{1.8}$ was first proposed by Chapman [60] in 1979, but a more recent study shows that the required number of cells can be as high as $N \propto {Re_L}^{2.4}$ [61]. The number of required nodes approaches DNS level ($N \propto {Re_L}^{3.2}$), which is too expensive to have any practical use. Therefore, an additional wall model is necessary to reduce computing time. In other words, both LES and RANS apply an assumed form of a solution to the wall boundary layer without solving ordinary differential equations, so a less dense grid can be applied near the wall. This is a great challenge for turbulence researchers because the Navier-Stokes equations have not yet been direct solved.

The Log-law and Power-law are the most common solutions that have been applied to the boundary layer. It is worth mentioning that it has been over 20 years since the introduction of the Power-law [62]. The argument between the Log-law and the Power-law has never stopped [43, 63-65]. The difference between the Log-law and the Power-law is 5% to 10% in LES simulations [45]. In addition, the Log-law is independent of Reynolds number, which makes the Log-law much easier to apply and more commonly used for numerical simulation. However, both the Log-law and the Power-law are based on equilibrium boundary layer assumptions, and recent in-cylinder micro-PIV results show that those assumptions do not hold in the engine [57, 66]. Furthermore, the thermodynamic law of the wall has more sensitivity to variations of the mean flow and temperature field than the hydrodynamic law of the wall [67, 68]. However, the current law of the wall does not reflect this phenomenon. In fact, researchers have found several cases where the hydrodynamic law of the wall holds true, but the thermodynamic law of the wall does not. Therefore, a remodel is needed for thermodynamic near wall- functions.

For RANS, there are many approaches for Log-law functions; the most widely used wall functions are proposed by Launder and Spalding [69], where u^+ and y^+ are modelled as:

$$U^* \equiv \frac{U_p C_\mu^{1/4} k_p^{1/2}}{\tau_w / \rho}$$

Equation 2.47

$$y^* \equiv \frac{y_p C_\mu^{1/4} k_p^{1/2} \rho}{\mu}$$

Equation 2.48

Therefore, the Log-law can be rewritten as:

$$U^* = \begin{cases} y^*, & (y^* < 11) \\ \dfrac{1}{\kappa} \ln(E^* y^*), & (11 < y^* < 0.1\delta) \end{cases}$$

Equation 2.49

Where E^{*} = 9.793 is an empirical constant. $C_{\mu} = 0.09$ is a model constant for turbulent viscosity. The subscript “p” denotes the value for a cell point. The $\mathscr{k}_p$ is turbulent kinetic energy that can be solved as a boundary condition:

$$\left.\frac{d\mathscr{k}_p}{dy_p}\right|_{y_p=0} = 0$$

Equation 2.50

In Equation 2.49, the equilibrium assumption is adopted, which means the production of the turbulence kinetic energy equates to the dissipation. For k-ε models, the production of kinetic energy Ƥ_k can be calculated based on the Boussinesq approximation [70]:

$$\text{Ƥ}_k = \frac{{\tau_w}^2}{\text{ƙ} C_{\mu}^{1/4} \mathscr{k}_p^{1/2} \rho y_p}$$

Equation 2.51

and the dissipation rate ε is calculated from:

$$\varepsilon = \frac{C_{\mu}^{3/4} \mathscr{k}_p^{3/2}}{\text{ƙ} y_p}$$

Equation 2.52

In addition, the buffer layer’s effects and the meso layer’s effects are not included in Equation 2.49. At $y^{*} \approx 11.225$, the linear equation is intercepted with the log equation. However, neither equation is valid within $5 < y^{*} < 30$. Currently, we do not have a good RANS model for buffer layer and meso layer calculations. A RANS-LES hybrid approach, based on a near-wall turbulent kinetic energy function and mix length equation, shows good potential for solving buffer layer velocity [71].

For temperature simulation, a Reynolds analogy assumption is implemented for most of the RANS simulation [72, 73]. A similar logarithmic law for mean temperature is employed with viscous heating.

$$T^* = \begin{cases} Pry^* + \dfrac{1}{2}\dfrac{{U_p}^2 C_\mu^{1/4} k_p^{1/2} \rho Pr}{\dot{q}}, & (y^* < 11) \\ Pr_t[\dfrac{1}{\kappa}\ln(E^* y^*) + P_{Pr}] + \dfrac{C_\mu^{\frac{1}{4}} k_p^{\frac{1}{2}} \rho}{2\dot{q}}\left[Pr\,{U_p}^2 + (Pr - Pr_t){U_c}^2\right], & (11 < y^* < 0.1\delta) \end{cases}$$

Equation 2.53

$$T^* \equiv \frac{(T_w - T_p) C_\mu^{1/4} k_p^{1/2} \rho c_p}{\dot{q}}$$

Equation 2.54

For air, $Pr = 0.7$and $Pr_t = 0.9$, and the function P_{Pr} i computed by Jayatilleke for the smooth wall and the rough wall, respectively [74].

Smooth surface: $P_{Pr-smooth} = 9.24\left[\left(\frac{Pr}{Pr_t}\right)^{\frac{3}{4}} - 1\right](1 + 0.28e^{-0.007Pr/Pr_t})$

Rough surface: $P_{Pr-rough} = 3.15Pr^{0.695}(\frac{1}{E'} - \frac{1}{E^*})^{0.359} + (\frac{E'}{E^*})P_{Pr-smooth}$

Equation 2.55

Where E' is defined as:

$$E' = \frac{E^*}{f_r}$$

Equation 2.56

$$f_r = \exp(\kappa\Delta\mathrm{H})$$

Equation 2.57

Where ΔH is surface roughness (arithmetic average of the absolute height of a surface). The k-ω model is also a frequently used method for near wall simulation. In addition, researchers have recently studied and included the compressibility effect [75], free steam turbulence effects [76], and transient state engine condition effects [77]. Non-equilibrium wall functions were postulated by Kim and Choudhury [78]. The Log-law was extended to include the sensitization of the pressure-gradient effects.

$$\frac{\tilde{U} C_\mu^{1/4} k_p^{1/2}}{\tau_w/\rho} = \frac{1}{\kappa}\ln(E^* y^*)$$

Equation 2.58

Where $\tilde{U}$ is defined as

$$\tilde{U} = U_p - \frac{1}{2}\frac{dp}{dx}\left[\frac{\delta_v}{\rho\kappa\sqrt{k}} ln\left(\frac{y_p}{\delta_v}\right) + \frac{y_p - \delta_v}{\rho\kappa\sqrt{k}} + \frac{{\delta_v}^2}{\mu}\right]$$

Equation 2.59

The δ_v is the viscous sublayer thickness, and it is assumed as:

$$\delta_v = \frac{11.225\mu}{\rho C_\mu^{1/4} k_p^{1/2}}$$

Equation 2.60

Using Equation 2.58, the production of the kinetic energy and the dissipation rate for the wall-adjacent cell can be computed as:

$$Ƥ_k = \frac{{\tau_w}^2}{ƙ C_\mu^{1/4} \mathscr{k}_p^{1/2} \rho y_p} \ln(\frac{y_p}{\delta_v})$$

$$\epsilon = \frac{1}{y_p} [\frac{2\mu}{\rho \delta_v} + \frac{C_\mu^{\frac{3}{4}} \mathscr{k}_p^{\frac{1}{2}}}{ƙ} \ln(\frac{y_p}{\delta_v})] \mathscr{k}_p$$

Equation 2.61

From Equation 2.61, the value of $Ƥ_\mathrm{k}$ and ϵ can vary from cell to cell under pressure gradient conditions [78], which partially relaxes Equation 2.58’s velocity calculation from the equilibrium assumption. However, the temperature distribution is still solved by Equation 2.53 for non-equilibrium conditions. As discussed previously, we can expect some major error from Equation 2.53’s temperature calculation with non-equilibrium conditions because of the invalid Reynolds analogy assumption. In addition, Nicolas Dronniou and John Dec point out that the in-cylinder boundary layer is also affected by an unidentified phenomenon other than viscous heat, compression effect and pressure effect [79]. Therefore, an investigation is necessary to develop a new thermodynamic law of the wall which must include consideration of pressure-gradient effects.

2.8 In-Cylinder Surface Temperature Measurement

The study of in-cylinder heat transfer requires wall temperature measurements. Fast response surface thermocouples are widely used for in-cylinder temperature measurement. At least three types are described in the literature: the coaxial, the pair-wire, and the thin film type [80, 81]. The coaxial and pair-wire are usually used for measurement of metal surface temperature [17], whereas the thin film type is usually used to measure the surface temperature of in-cylinder ceramic coatings [81, 82]. The coaxial thermocouple is used for this work due to its highly dynamic behavior under compression. However, for accurate measurements, the thermal inertial $\sqrt{k\rho c_p}$ of the thermocouple should be matched to that of the wall material, where k is thermal conductivity, ρ is mass density, and c_p is specific heat [83]. Differences in thermal inertia exacerbate errors under rapidly changing heat flux conditions. The time constant of the thermocouples may limit the bandwidth of the temperature data being measured, and deposits are known to rapidly build up on the thermocouples exposed to cylinder gases, inducing errors [83]. Also, thermocouples have limited measurement location inside the cylinder, and it is hard to measure the temperature of moving engine parts, such as valves and pistons. More importantly, because of the thermal resistance between thermocouples and its surrounding wall, the thermocouple itself can interfere with the temperature field, which is not ideal for the study boundary conditions [84-86]. Another technique used to measure in-cylinder surface temperature is phosphorescence. Laser-induced phosphorescence (LIP) is an accurate and non-intrusive means of temperature measurement based on temperature-dependent fluorescence lifetimes of rare earth elements [87, 88]. In applying this method, the molecules of a thermographic-phosphor are brought to an excited electronic state by an ultraviolet source, typically a laser or photodiode. The subsequent red-shifted emission as the molecule decays to its ground state is observed with a sensor, the decay rate of which is temperature dependent. However, the sample rate is limited to that of the excitation laser or photodiode frequency. Using a typical Nd:YAG laser with a 10 Hz laser repetition rate, only one measurement per four-stroke engine cycle can be obtained at 1200 RPM. At this temporal resolution, instantaneous heat flux from phosphorescence measurements cannot be determined. In addition, temperatures of phosphor layers may not represent those of the substrate wall [88]. Thermographic phosphor can be painted on any surface to be investigated, which makes LIP much more flexible than thermocouples. However, the thermal resistance between the thermographic phosphor and the wall is more likely to disturb the temperature boundary layer [88]. There is a need to improve surface temperature measurement techniques in order to study highly dynamic heat flux problems.

2.9 Outline of the Dissertation

This dissertation can be divided into three parts: experimental technique development (Chapter 3 and Chapter 4), engine experiment (Chapter 5), and engine heat transfer model (Chapter 7). This study reports on the development of a technique suitable for engine in-cylinder surface measurement, as the traditional method is “hard to reach.” The engine experimental investigation was an experimental study of in-cylinder near wall temperature distribution. The gas-to-wall heat flux has been conducted utilizing simultaneous measurements of instantaneous surface temperature (using infrared (IR) diagnostic) and near-wall gas temperature distribution (using Planar Laser Induced Fluorescence (PLIF)). Further, a near wall velocity field measurement was established by in-cylinder micro-PIV at the same engine conditions as the temperature distribution measurement to validate the Reynolds analogy. Finally, a new engine heat transfer model is proposed based on the experimental results.

Following is a detailed outline for each chapter.

- Chapter 3: A laser induced phosphorescence technique was used to study in-cylinder wall temperature effects on engine out unburned hydrocarbons during the engine transitional period (warm up). A linear correlation was found between the cylinder wall surface temperature and the exhaust unburned hydrocarbon concentration at medium and high charge densities. At low charge density, no clear correlation was observed because of missfire events. However, the laser induced phosphorescence technique was not suitable for studying engine instantaneous heat flux because the laser induced phosphorescence technique had a low sampling rate.
- Chapter 4: A new auto background correction infrared (IR) diagnostic was developed to measure the instantaneous in-cylinder surface temperature at 0.1 CAD resolution. A numerical mechanism was designed to suppress relatively low-frequency background noise and provide an accurate in-cylinder surface temperature measurements with an error of less than 1.4% inside the IC engine. In addition, a proposed optical coating reduced time delay errors by 50% compared to more conventional thermocouple techniques.
- Chapter 5: A new cycle-averaged $\overline{Re_s}$ number was developed for an IC engine to capture the characteristics of engine flow. Comparison and scaling between different engine flow parameters are available by matching the averaged $\overline{Re_s}$ number. From experimental results, the engine flow motion was classified as intermittently turbulent, and it is far different from the original fully developed turbulent assumption, which has previously been used in almost all engine

simulations. The intermittent turbulence could have a great impact on engine heat transfer because of the transitional turbulence effect.

- Chapter 6: A new multi zone heat transfer model is proposed for IC engines only. The model includes pressure work effects and improved heat transfer prediction compared to the standard Law of the Wall model. An engine 3D CFD model further proves the existence of transitional turbulent flow.
- Chapter 7: The summary and conclusions are given. Suggested future work is discussed.

CHAPTER 3 : IN-CYLINDER WALL TEMPERATURE INFLUENCE ON UNBURNED HYDROCARBON EMISSIONS DURING THE TRANSITIONAL PERIOD

3.1 Introduction

Diesel engines are attractive due to their high thermal efficiencies although meeting ever more stringent emissions regulations remains challeng. Of concern are emissions of unburned hydrocarbons (UHC), which are typically generated in elevated quantities during the starting process when after-treatment devices are below operating temperatures. Varying boundary conditions during engine starting may result in unstable combustion or high emissions. Emissions during starting are difficult to predict as ambient conditions vary by locale or season. Incomplete combustion and misfiring cycles can cause blue or white smoke, indicating high UHC emissions [89-91]. The phenomenon is difficult to investigate due to the complex nature of the transient process. Autoignition has classically been considered to be a function of charge temperature, mixture density, induction duration, and mixture composition [92]. Each of these factors can have a great impact on combustion phasing and emission. By influencing the mixture composition through fuel wall film evaporation rates, as well as the charge temperature by forming the boundary conditions for convective heat losses, surface temperatures can have a strong indirect effect on autoignition.

Laser induced phosphorescence is an accurate, high resolution, and non- intrusive means of temperature measurement based on temperature-dependent fluorescence lifetimes of rare earth elements [90]. Temperatures in a range from cryogenic up to1700 º C can be determined by the use of different phosphors. The technique has been used for measurement of the wall temperature in both internal combustion and turbine engines [93-95].

In this work, cylinder wall temperature and engine–out UHC emissions were measured during warm-up sequences in an optical engine over a range of charge densities. Laser induced phosphorescence was used for in-cylinder surface temperature measurement while simultaneous cycle-resolved engine-out UHC measurements are made. The temperature measurements were made at two locations on windows mounted in the piston bowl and in the squish zone region. The effect of thermal boundary conditions on cycle-to-cycle variation can thus be investigated during the starting process of an optical engine, providing insight into their effect on combustion phasing and engine UHC emission. Although the wall temperatures were measured in an engine having non-metallic parts (quartz windows), trends observed in the optical engine are believed to qualitatively represent those of metallic engines. Similar engines have been shown to closely match the near-TDC thermodynamic conditions and emissions of a metal engine [96].

Laser induced phosphorescence is a temperature measurement technique based on the detection of phosphorescence from thermographic phosphors. In the experiments, the phosphor La2O2S:Eu was used. Excited by a pulsed UV laser, the resulting phosphorescence was observed, the emission intensity of which decays exponentially according to the following relation:

$$I = I_0 \cdot e^{-\frac{t}{\tau}}$$

Equation 3.1

where I_0 is the initial emission intensity, t is time, and τ is the time constant of the phosphorescence decay [94]. The time constant is temperature-dependent and is a property of the laser-excited thermographic phosphor. By measuring the decay rate of the emission intensity, the surface temperature could therefore be determined. Measurement error using this technique has been reported to be less than 1% [89]. Typical phosphorescent emission curves are shown in Figure 3.2, illustrating that decay rates increase with higher temperature.

The emission processes of phosphor La2O2S:Eu are caused by energy transitions within the Eu3+ atom. Transitions from 5D2, 5D1, and 5D0 states result in emission at 512 nm, 538 nm, and 624 nm wavelengths that are highly sensitive to temperature [97].

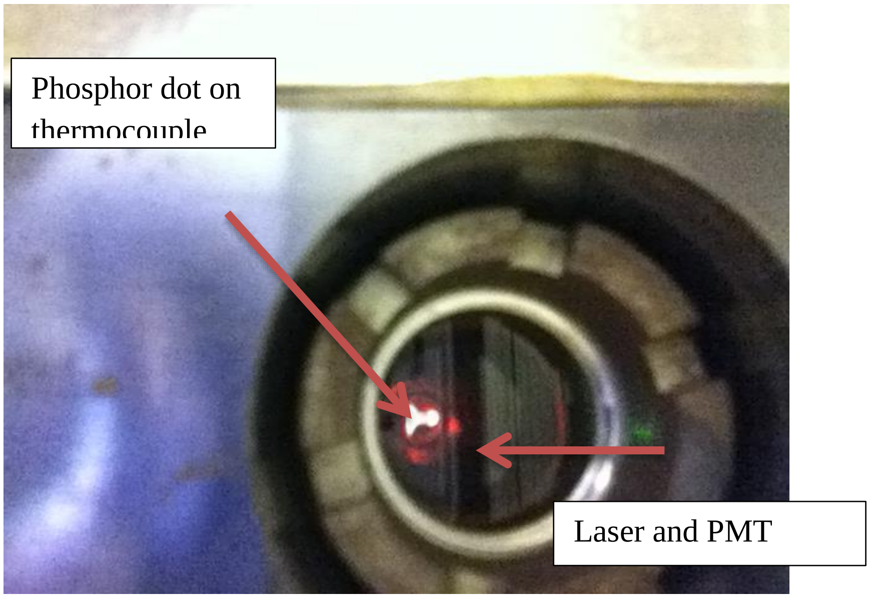

Figure 3.1: Inside view of phosphor calibration set up

The 538nm emission line was chosen for observation in the experiments due to its high-temperature sensitivity in the 100 °C to 300 °C range. A photo-multiplier tube (PMT) (Hamamatsu model H10721) was used to detect the phosphorescence emission.

A band-pass filter with 540 nm center wavelength and a full-width half maximum of 10 nm was placed in front of the PMT to minimize interference from the other bands. In addition, a quartz glass lens (focal length = +100 mm) was used to focus the phosphorescence onto the PMT. Prior to the engine experiments, the phosphor was calibrated under controlled temperature conditions. A K-type thermocouple junction was coated with a mixture of phosphor and HPC binder, and located in a chamber having a geometry similar to that of the engine cylinder, as shown in Figure 3.1. The entire thermally insulated chamber was heated to the desired feedback-controlled set point temperature by an electric resistance heater (2000 W). The third harmonic of a Nd:YAG laser (Spectra-Physics INDI-HG-10S) was used to provide a 7 ns-long pulsed, 8 mm diameter beam of 355 nm wavelength, which was directed at the thermocouple bead and served as the UV excitation source for the phosphor. The laser was introduced to the calibration chamber through a quartz window mounted on its side. For both calibration and experiment, the phosphorescence following laser excitation was observed from the same window which was used to introduce the excitation laser beam into the calibration chamber and cylinder, using a long pass filter to avoid introducing the laser output into the PMT. The PMT gain was set to 0.5 V for all experiments. The PMT current output signal was conditioned with a hardware low-pass filter before being terminated with a 100 Ω load resistor. A 1 GHz recording oscilloscope (Agilent MSO8104A) was used to sample the signal voltage across the load resistor. Time constants were then fit to the measured phosphorescence emission. Calibration was performed in the range of temperatures between 375 and 525 K. Figure 3 shows the resulting calibration curve of the time constant versus the temperature. Each data point on the graph is an average of 10 measurements. The standard deviation is less than 2%.

During engine experiments, the repetition rate of the laser was maintained at 10 Hz. The laser energy was kept at 200 µJ for all experiments, an energy level deemed sufficiently low such that laser heating of the wall can be neglected.

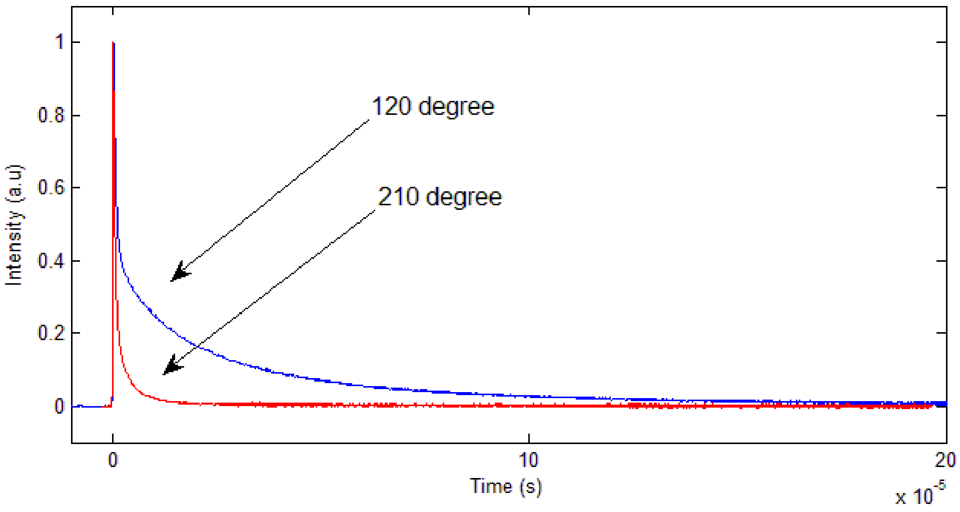

Figure 3.2: Phosphorescent emission intensity (538 nm) following a UV laser pulse at 120 °C and 210°C

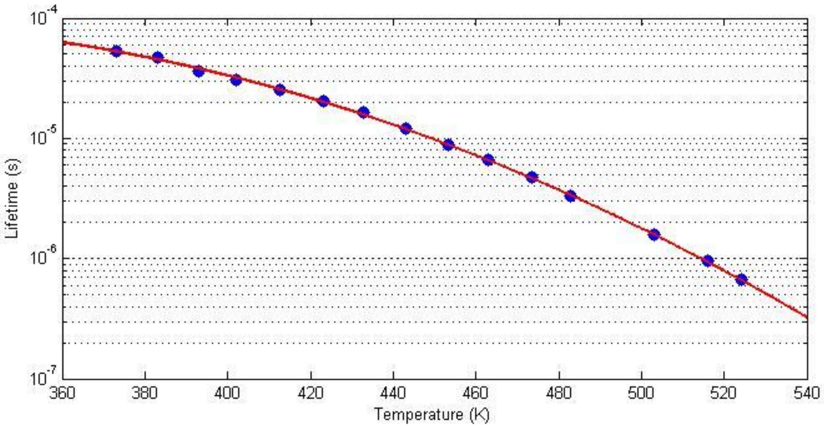

Figure 3.3: Phosphorescence time constant vs. temperature for La2O2S:Eu at 538 nm wavelength.

The phosphor was applied on two quartz windows. The non-fluorescent ZYP HPC binder and the ZYP LK binder were mixed in 1:1 (vol/vol) proportions. The phosphor and binder were mixed at a ratio of 0.2:1 (vol/vol) and then painted onto the clear quartz windows. The phosphor-painted windows were dried for 12 hours prior to being cured at a temperature of 150 °C [90].

3.2 Engine Operation Procedure

A single-cylinder, direct-injection optical research engine (AVL 5402) was used in these experiments. The specifications of the engine are shown in Table 1. Table 2 shows the injector specifications.

Table 3.1: Engine Specifications

Number of cylinders	1
Cycle	4-stroke
Displacement	510 cm^3
Bore	85 mm
Stroke	90 mm
Connecting rod length	148 mm
Compression ratio	15:1

Bowl diameter	40 mm
Bowl depth	14.5 mm
Number of intake valves	2
Number of exhaust valves	2
Intake valve opening/closing	330°/-152° ATDC
Exhaust valve opening/closing	145°/-355° ATDC
Injection system	Bosch common rail
Swirl Ratio	2.0 to 4.5
Fuel	n-heptane

Table 3.2: Injector specifications

DI injector type	Continental-Piezo
Design	VCO-Nozzle
Number of holes	7

Hole diameter	0.115 mm
Angle of fuel-jet axis (inclusive)	142°

The measurements were taken at 1200 rpm engine speed. Before the first firing cycle, the engine was motored to reach a steady state temperature. The engine was preconditioned by circulating coolant and lubricant oil at a temperature of 60 °C. Intake air temperature was controlled and held constant at 30 °C. The start of fuel injection and the injection duration were -5 CAD BTDC, and 0.3 msec, respectively. Injection pressure was maintained at 800 bars. Fuel quantity injected per cycle based on injection calibration was 8.77 mg/cycle. Unlike other optical engine experiments, the engine was continuously firing, and data from the first 65 continuous firing cycles were recorded. Before each measurement, the engine was motored for 30 minutes to ensure similar conditions for all experiments. The engine was fueled with neat n-heptane, a standard reference fuel.

The cylinder pressure was measured by an un-cooled piezoelectric pressure transducer (AVL GH 12D) mounted in the cylinder head, and a strain gauge pressure transducer (AVL Sl31D-2000) was used to monitor fuel line pressure. Apparent heat release rates were calculated from the high-resolution pressure data applying the analysis of Heywood [92]. The cycle-resolved engine out UHC emission was recorded by a flame ionization detector (FID), the output of which was averaged over the crank angle period when the exhaust valves were open to provide a single representative value per engine cycle.

A sonic nozzle was used to control the intake air mass flow rates, which at constant engine speed translates to controlling charge density at a given piston or crank angle position. Experiments were run for TDC charge densities of 19.2, 20.8, and 24.1 kg/m^3. In addition, a closed-loop feedback temperature controller and a 2.5 kW heater were used to control the intake temperature.

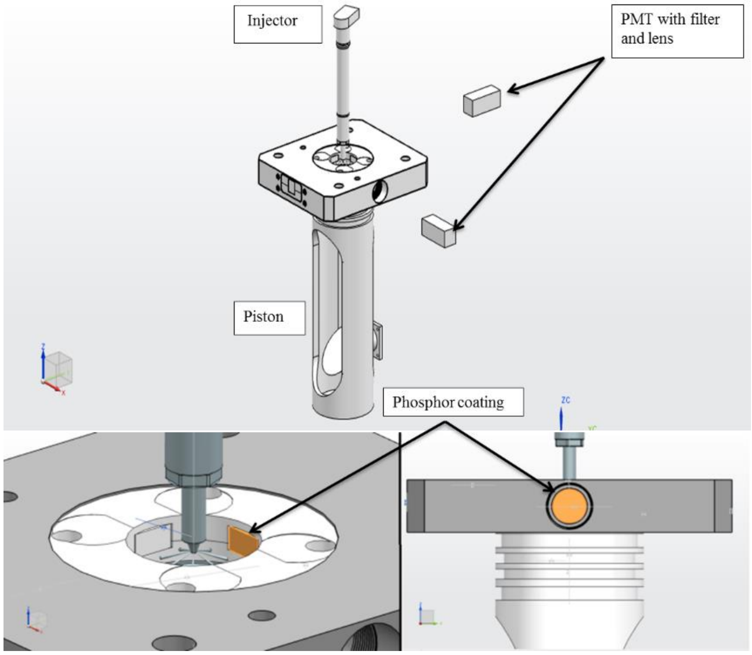

Figure 3.4: Experimental setup for laser induced phosphorescence in an optical engine

As shown in Figure 3.4, the phosphor was painted onto surfaces in two different locations. One location is the side window inside the piston bowl, and the other the window in the cylinder wall, in the squish zone. The laser was introduced through the window onto which the phosphor was painted, thus exciting the phosphor from the side that is adhered to the window. This is believed to provide results that are more representative of wall temperatures than when exciting the phosphor layer from the combustion gas side [98]. The fuel injector was oriented such that one of the jets was aligned with the phosphor dot. To avoid the measurement capturing evaporative cooling effects following fuel wall impingement, the timing of the laser excitation and measurement was chosen to coincide with the injection command signal just prior to the start of injection, at -5° ATDC. While this injection timing was not optimized for thermal efficiency, it was selected as the angle where the piston bowl and the cylinder access window align, providing optical access to the phosphor for both the laser and PMT.

3.3 Results and Discussion

The laser induced phosphorescence technique was applied to an optical engine to measure the cylinder wall temperature during warm up processes. The first 65 continuous firing cycles were recorded. The temperature was measured at two different locations. One was measured on the surface of a piston window inside the piston bowl, and another one was measured on a side window located in the squish zone. The intake air temperature was fixed at 30 °C for all the experiments, run at 19.21 kg/m^3, 20.75 kg/m^3, 24.14 kg/m^3 charge densities, as calculated at TDC. Simultaneously, the engine-out UHC was measured by the FID. This made it possible to the study wall temperature influence on the engine out UHC emissions at different charge densities.

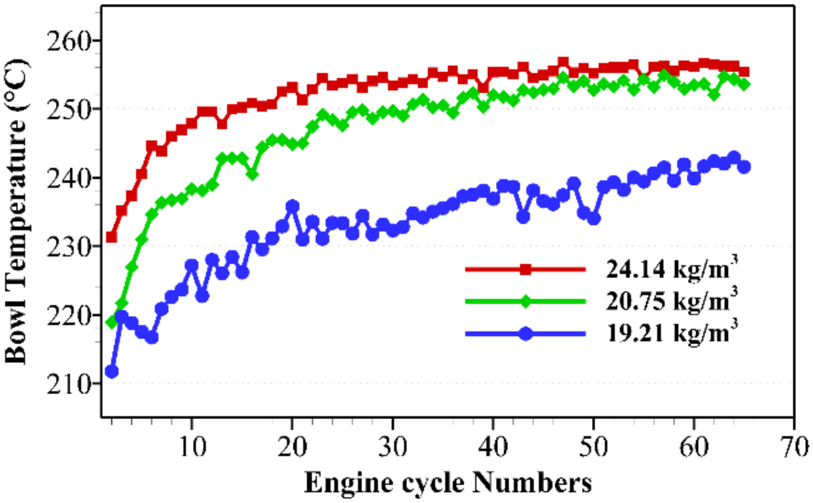

Figure 3.5: In-bowl temperature measurements at -5 CAD ATDC during warm up process with different charge densities.

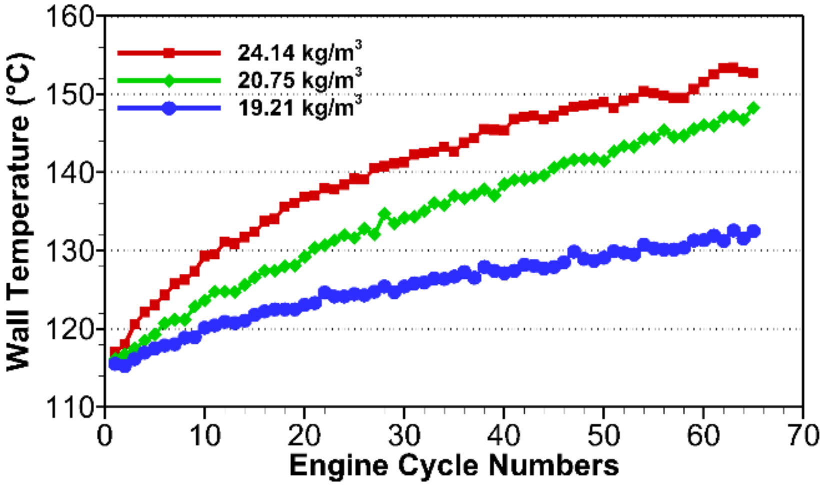

Figure 3.6: Squish zone wall temperature measurements at -5 CAD ATDC during warm up process with different charge densities.

Figure 3.5 and Figure 3.6 show the cycle by cycle phosphor surface temperatures. It is clear that higher charge densities result in greater wall temperature rise rates. The behavior is examined in the context of the commonly used Equation 2.5, the Woschni correlation, describing heat convection coefficients. An isentropic assumption applied to the charge core bulk temperature during compression implies that at a given crank-angle, the gas temperature is the same for all charge densities when the intake temperature remains fixed. However, the cylinder pressure increases with charge density. Since the convection coefficient in Equation 2.5 nearly scales with the pressure, the result is more heat is lost from the gas to the cylinder wall at higher charge densities. However, high convective heat transfer rates can also be seen to more quickly warm up the engine.

Figure 3.5 and Figure 3.6 show that the in-bowl temperature increases at a faster rate than the squish-zone cylinder wall temperature. The bowl temperature increases rapidly at first over several cycles, then the rate of the temperature rise decreases, except at the lowest charge density, which exhibits a near-constant temperature rise rate. The bowl temperature increased more than 20 °C during the warm up process. In addition, the steady state temperature for both high and medium charge densities was the same, roughly 257 °C. It also appears likely that at low charge densities, the bowl temperature will reach the same steady state temperature given a longer observation time. In other words, the final steady state bowl temperature is less sensitive to in-cylinder pressure. However, for higher charge densities, the bowl temperature reaches steady state temperature sooner.

The evaporative cooling effects of the fuel wall jet impingement are considered as possible factors influencing surface temperature rise rates. Since higher charge densities reduce liquid penetration lengths, such cooling effects can be expected to be suppressed as charge densities are increased. However, earlier Mie scattering liquid length measurements at similar conditions suggest wall impingement does not occur. That the asymptotic steady temperatures are similar for both intermediate and highest charge density supports the conclusion that the observed differences in temperature rise rates are convective effects.

More than a 100 °C difference was observed between the bowl temperature and the squish zone cylinder wall temperature. Moreover, the squish zone cylinder wall temperature increased at a lower rate than the bowl temperature, requiring a longer time to reach steady state temperature, as shown in Figure 3.6.

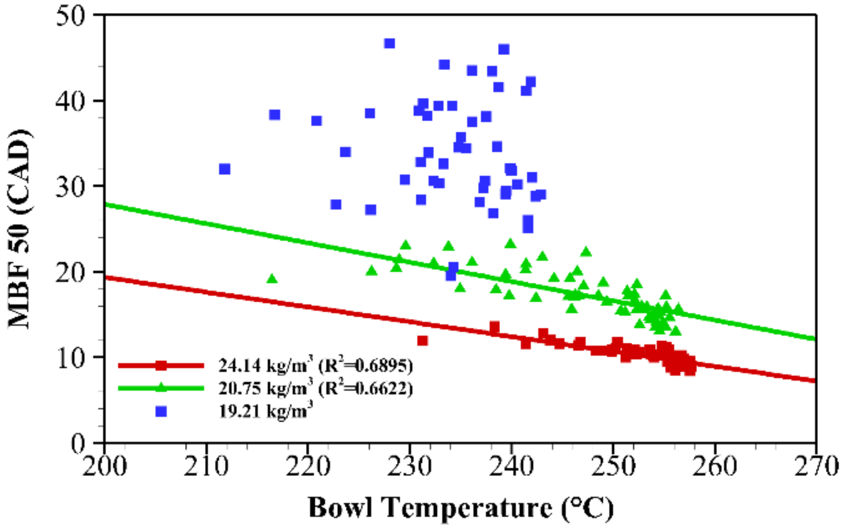

Figure 3.7: In bowl temperature measurements at -5 CAD ATDC vs. the MBF50 (except misfiring cycles) for different charge densities.

Figure 3.7 shows the effect of the piston bowl surface temperature on combustion phasing. Both the high bowl temperature and the in-cylinder pressure are seen to advance combustion phasing. However, at low charge densities, the correlation between combustion phasing and bowl temperatures is lost. A possibility is that the reaction rates of the pressure-dependent reactions are slowed by the lower pressure (density), extending ignition delay into the expansion stroke and contributing to combustion instabilities. The observation is made that combustion phasing keeps advancing despite measured bowl temperatures attaining steady values. This suggests that surface temperatures in locations other than the piston bowl, which undergoes slower transient heating, play a role in combustion phasing.

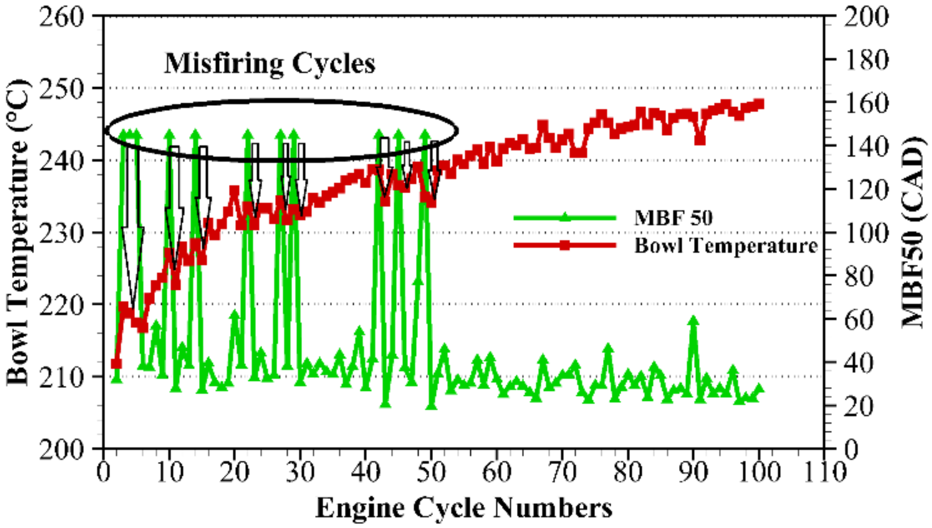

Figure 3.8: In bowl temperature measurements at -5 CAD ATDC set into relation to the MBF50 during warm up process at 19.21 kg/m3charge density.

Figure 3.8 shows the bowl temperature for low charge density and its corresponding cycle-by cycle MBF 50. Clearly, misfiring cycles caused the bowl temperature to drop for the following cycle, as indicated by the arrows in the Figure 3.8. In addition, misfiring was more frequent at lower bowl temperature. However, elevated bowl temperatures do not preclude the occurrence of misfires. Three misfires are evident between cycles 40-50, by which time the temperature has been considerably raised. Beyond cycle 5, misfires mostly are followed by cycles having combustion more advanced than immediately prior to the misfired cycle. A plausible explanation is that the availability of the remaining residual fuel unconsumed by the misfired cycle creates a richer, more reactive mixture that shortens the ignition delay. This effect appears to dominate over the lower surface temperatures evident following the misfires.

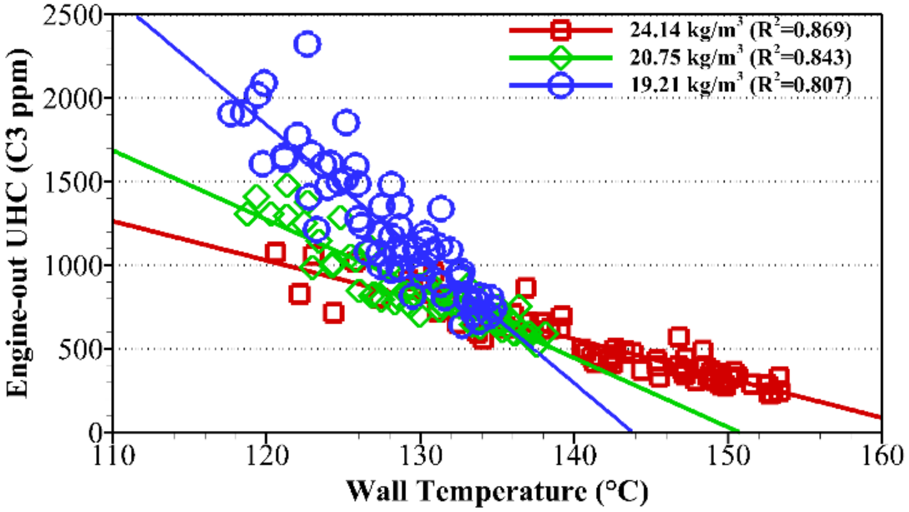

Figure 3.9: Engine out UHC (except misfiring cycle) vs. squish zone wall temperature with different charge densities.

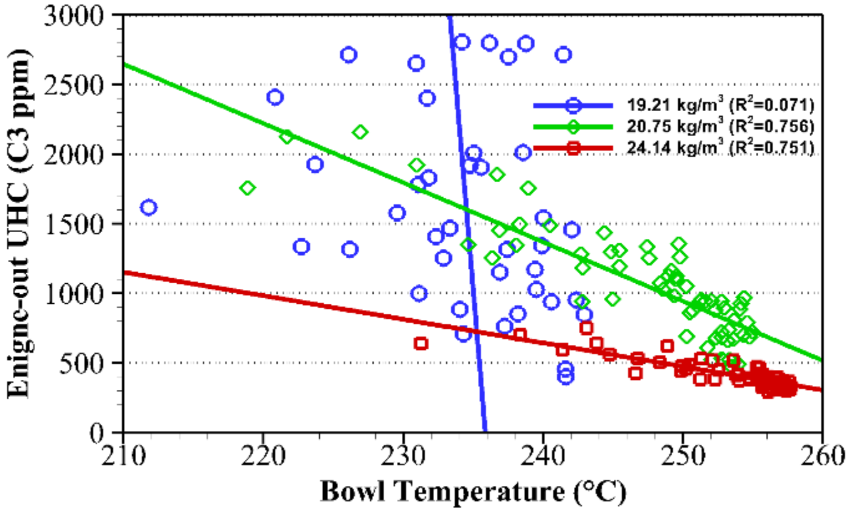

Figure 3.10: Engine out UHC (except miss firing cycle) vs. bowl temperature with different charge densities.

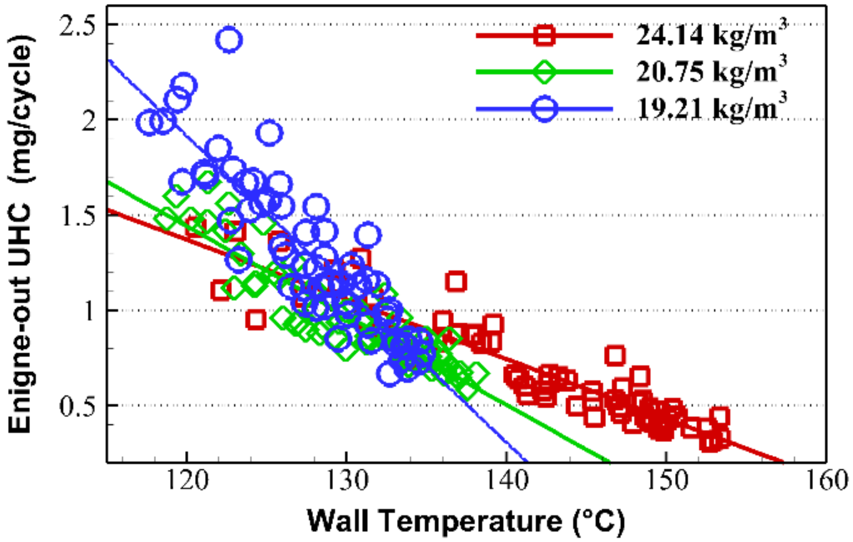

Figure 3.11: Mass base engine out UHC (except misfiring cycle) vs. squish zone wall temperature with different charge densities.

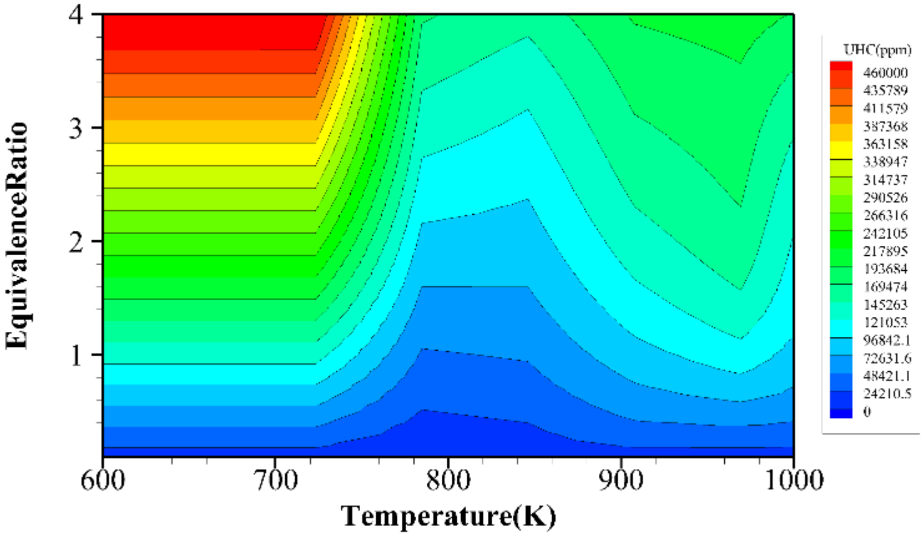

Figure 3.12: Simulation result from Chemkin for UHC.

From Figure 3.9, it is obvious that the squish zone cylinder wall temperature has a strong effect on the engine out UHC. Engine-out UHC mole fractions significantly decrease as the squish zone temperatures rise. This result is consistent with reported observations that for combustion phasing retarded beyond that for optimum thermal efficiency, the engine-out UHC mainly comes from the squish volume [99]. As seen in Figure 3.9, the sensitivity of the engine out UHC, on a mole fraction basis, to the cylinder wall temperature decreases as the charge densities are increased. Figure 3.10 shows how engine out UHC relates to the bowl temperature during the warm-up process. In comparison to Figure 3.9, UHC has less dependence on the bowl surface temperature, particularly at low charge densities where no correlation between the parameters exists.

Total engine-out UHC values for the different charge densities are calculated considering the measured mole fractions and respective intake air mass flow rates. Figure 3.11 shows a relation between the mass-based UHC and the squish zone wall temperature. Similar to Figure 3.9, the mass-based UHC emission at higher charge densities is less sensitive to the wall temperature. However, low charge density produces less engine out UHC mass when the wall temperature is 135 °C or higher. These results suggest that a strategy for the reduction of UHC emission may be comprised of an elevated boost (high charge densities) early in the starting process, with the boost decreasing for lower charge densities as the engine warms.

From previous studies, it is known that significant UHC emissions can result at low load. However, increasing load has little effect on UHC formation in the squish volume [99]. In addition, low charge densities also cause overall equivalence ratios to increase. In other words, high charge densities would have leaner mixtures. Therefore, Figure 3.9 also illustrates that the UHC emission of rich mixtures is more temperature sensitive than for leaner mixtures. A CHEMKIN kinetic simulation was conducted to support this observation. Figure 3.12 shows the calculated UHC result of a CHEMKIN constant volume homogeneous reactor simulation over a sweep of the gas temperature. The results shown are for a reaction time of 1 msec. The colors are used to indicate the mole fraction of the UHC. In Figure 3.12, the temperature, in the 720 °C to 790 °C range, has more impact on UHC concentration at richer mixtures. This is evident by the steeper UHC gradients following a rich constant equivalence ratio line rather than existing along a lean equivalence ratio line in this temperature range. From the pressure trace, the bulk gas temperature is calculated to be in a similar range of 650 °C to 800 °C during the warm up process. The simulation results are consistent with the experimental observation.

CHAPTER 4 : DUAL BAND INFRARED DIAGNOSTIC APPLICATION IN AN OPTICAL ENGINE

4.1 Introduction

Heat transfer affects engine performance, emission, and efficiency. However, wall temperature measurements can be a challenge inside an internal combustion (IC) engine due to the hostile combustion environment, moving surface, and short time scale (10^{-3} s) [4, 100]. Various thermocouples are widely used for engine heat transfer studies. Coaxial thermocouple and a pair-wire thermocouples have been used for metal surfaces [82, 101], and a thin-film thermocouple has been applied to measure the temperature of an in-cylinder ceramic coating [17]. However, in general, thermocouples create some common problems for engine in-cylinder surface temperature measurement. It is very hard to measure the temperature of a moving surface, such as the piston and valve. Often, the thermocouple, which is installed on the piston, has less than 50% reliability and a poor signal-to-noise ratio [10]. In addition, the thermal inertia of the thermocouple can cause a time delay between the measurements and the actual surface temperature [102]. This is a particular problem for in-cylinder surface temperature measurement at high engine speed [4]. The thermal resistance between the instrument and wall will cause an over prediction of the surface temperature [102, 103].

Recently, laser induced phosphorescence (LIP) has become another technique used for surface temperature measurements in IC and turbine engines [77, 104]. Temperature measurement is based on the temperature-dependent lifetime of a thermographic phosphor fluorescence [77]. While this technique is capable of obtaining mean temperature of a moving surface, the temporal resolution of the measurement is limited by the inadequate repetition rate of the excitation light source. Therefore, LIP is not suitable for instantaneous gas-to-wall heat transfer measurements in the engine when using available laser with 10 Hz repetition rates. In addition, thermographic phosphor also introduces thermal inertia error and thermal resistance error, which are similar to problems with a thermocouple. Therefore, an improvement in the surface temperature measurement technique is needed to further develop IC engine heat transfer research.

Appling infrared technique for temperature measurement in an IC engine can be tracked back to the 1960s [105], but the accuracy of thoses earlier measurements is not clear. For engine wall temperature measurement, the infrared technique has several advantages which make it have great potential for measuring the temperature of a moving surface, such as engine piston and valve. First, the optical sensor, which is used in this work, has fast response timing ($10^{-8}\ s$), and can capture heat release characteristics of combustion. Second, the infrared measurement technique is a noncontact temperature measurement. This makes it simple to measure the temperature of a moving surface. Third, temperature measurement is based on the infrared signal, which directly come from the observed surface. Therefore, the instrument thermal inertial error and the thermal resistance error no longer exist for the infrared temperature measurement technique. In addition, the mid-infrared wavelength has been found to be most sensitive to the IC engine wall temperature range [106], which is around 400 K to 600 K.

The changes in emissivity and area of a moving surface can be compensated by using the two-color infrared method [107], which uses the ratio of two distinct spectral wavelength bands to determine the surface temperature. The target infrared radiation can be measured by two detectors with a beam splitter [108], a rotating filter wheel with a single detector [109], or a detector consisting of two different active regions [110]. However, applying the two-color infrared method can be difficult for IC engine wall temperature measurements. The diffuse emission and reflection from the cylinder walls and the closed volume geometry of an engine cylinder create a cavity, which has near blackbody behavior. Unfortunately, the engine wall temperature is non-uniform [100], and it generates background noise through an optical window. Therefore, a background correction is needed before applying the two-color infrared method. The physical background correction mechanism often requires a complex optical setup [109], and it is too bulky for an operating engine application.

In this work, a new numerical auto background correction method has been developed for the two-color infrared temperature measurement in an IC engine. First, this method was validated against a coaxial thermocouple and laser induced phosphorescence measurements in a motored engine. Then, the two-color infrared thermometer with numerical auto background correction was applied to measure the piston surface temperature of a diesel engine under various engine conditions.

4.2 Theory

Assuming Lambertian radiation, the electronic signal, which is generated by an IR detector with a narrow band-pass filter, is given by the following equation:

$$V(T,\lambda) = \iint_{\lambda_{min}}^{\lambda_{max}} S(\lambda)\cos(\omega) I_d \, d\lambda \, d\omega + \mathrm{V_b} = \bar{S}(\lambda_{center}, \omega) I_d + \mathrm{V_b}$$

Equation 4.1

Where $V(T,\lambda)$ is the electronical signal, and $\mathrm{V_b}$ is the "black current" signal. ω is the angle of the field of view, λ_{min} and λ_{max} is the band width of the narrow band-pass filter, and λ_{center} is the center wavelength of the narrow band-pass filter. $S(\lambda)$ is the overall sensitivity of the optical system, which can include the transmissivity of the narrow band-pass filter, the gain of the IR detector, and the reflectivity of the golden mirror. $\bar{S}(\lambda_{center},\omega)$ is the mean sensitivity over the filter bandwidth. For fixed λ_{center} and ω, $\bar{S}(\lambda_{center},\omega)$ can be found by calibrating the optical system against a blackbody source. $I_d$is the spectral intensity detected by the sensor. For a black body, it is given by Planck's Law:

$$I_b = \frac{2hc_o{}^2}{\lambda^5(exp\left(\frac{hc_o}{\lambda kT}\right) - 1)}$$

Equation 4.2

Where h is the universal Planck constant, and k is the universal Boltzmann constant. c_o is the speed of light in a vacuum. T is the surface temperature in Kelvin. Because of the natural of an operating engine, the infrared intensity measurement for a local surface is often heavily influenced by the background noise signal, which could potentially come from the diffuse emission and reflection of an engine component, optical window emission, and variant ambient environment. Therefore, the infrared intensity picked up by the detector can been considered as:

$$V(T,\lambda) = \bar{S}(\lambda_{center},\omega)I_d + \mathrm{V_b} = \bar{S}(\lambda_{center},\omega)\left[I_{surface}(\lambda,\mathrm{T})\sin\theta + I_{noise}\right] + \mathrm{V_b}$$

Equation 4.3

Where $I_{surface}$ is the radiation from the target surface, and θ is the incident angle of the view direction. I_{noise} is the infrared intensity from other sources, which is hard to eliminate with a physical background correction mechanism. However, $I_{surface}$ varies at high frequency (engine speed). Therefore, to eliminate the relative low frequency I_{noise}, we can derive the following relation: assuming $\frac{\partial \mathrm{V_b}}{\partial \mathrm{t}} = 0, and\ \frac{\partial I_{\boldsymbol{noise}}}{\partial t} \ll \frac{\partial I_{surface}(\lambda,\mathbf{T})}{\partial t}$:

$$\frac{\Delta V(T,\lambda)}{\Delta t} \approx \frac{\partial V(T,\lambda)}{\partial t} = \bar{S}(\lambda_{center},\omega)\ sin\theta \frac{\partial I_{surface}(\lambda,T)}{\partial t} + \bar{S}(\lambda_{center},\omega)\frac{\partial I_{noise}}{\partial t} + \frac{\partial V_b}{\partial t}$$

$$\approx \bar{S}(\lambda_{center},\omega)\ sin\theta \frac{\partial I_{surface}(\lambda,T)}{\partial t}$$

Equation 4.4

Where Δt is a finite time duration. Applying the two-color ratio method with Equation 4.4, the target surface infrared radiation can be simultaneously measured by two detectors with a beam splitter at two separate wavelengths. λ_1 and λ_2 are the center wavelength of the narrow-band filter, which is installed on the IR detectors. The ratio of the rates at which the electrical signals change can be written as:

$$\frac{\frac{\Delta V_1(T,\lambda_1)}{\Delta t}}{\frac{\Delta V_2(T,\lambda_2)}{\Delta t}} = \frac{\Delta V_1(T,\lambda_1)}{\Delta V_2(T,\lambda_2)} = \frac{\bar{S_1}(\lambda_1,\omega)\partial I_{surface}(\lambda_1,\mathrm{T})}{\bar{S_2}(\lambda_2,\omega)\partial I_{surface}(\lambda_2,\mathrm{T})}$$

Equation 4.5

At the measurement time instance, the rate of the surface temperature change is the same for both sensors, so $\frac{\partial I_{surface}(\lambda_{\mathbf{1}},\mathbf{T})}{\partial I_{surface}(\lambda_{\mathbf{2}},\mathbf{T})}$ can be rewritten as follows:

$$\frac{\frac{\partial I_{surface}(\lambda_1,T)}{\partial T}}{\frac{\partial I_{surface}(\lambda_2,T)}{\partial T}}=\frac{\partial I_{surface}(\lambda_1,T)}{\partial I_{surface}(\lambda_2,T)}=\frac{\bar{\varepsilon}(\lambda_1)\,exp\left(\frac{hc_o}{\lambda_1 kT_r}\right)\lambda_2^6\left(exp\left(\frac{hc_o}{\lambda_{2\mathrm{k}}T_r}\right)-1\right)^2}{\bar{\varepsilon}(\lambda_2)\,exp\left(\frac{hc_o}{\lambda_2 kT_r}\right)\lambda_1^6\left(exp\left(\frac{hc_o}{\lambda_1 kT_r}\right)-1\right)^2}$$

Equation 4.6

Where $\overline{\varepsilon}(\lambda_1)$ and $\overline{\varepsilon}(\lambda_2)$ are the mean surface emissivities across the narrow filter bandwidth. Assuming a gray surface, the ratio of $\overline{\varepsilon}(\lambda_1)$ and $\overline{\varepsilon}(\lambda_2)$ is assumed to be a constant and close to unity. Equation 4.5 and Equation 4.6 can be rewritten as:

$$\frac{\Delta V_1(T,\lambda_1)}{\Delta V_2(T,\lambda_2)}=\frac{\bar{S_1}(\lambda_1,\omega)\bar{\varepsilon}(\lambda_1)\,exp\left(\frac{hc_o}{\lambda_1 kT_r}\right)\lambda_2^6\left(exp\left(\frac{hc_o}{\lambda_2 kT_r}\right)-1\right)^2}{\bar{S_2}(\lambda_2,\omega)\bar{\varepsilon}(\lambda_2)\,exp\left(\frac{hc_o}{\lambda_2 kT_r}\right)\lambda_1^6\left(exp\left(\frac{hc_o}{\lambda_1 kT_r}\right)-1\right)^2}$$

$$=C(\lambda_1,\lambda_2,\omega)\frac{exp\left(\frac{hc_o}{\lambda_1 kT_r}\right)\lambda_2^6\left(exp\left(\frac{hc_o}{\lambda_2 kT_r}\right)-1\right)^2}{exp\left(\frac{hc_o}{\lambda_2 kT_r}\right)\lambda_1^6\left(exp\left(\frac{hc_o}{\lambda_1 kT_r}\right)-1\right)^2}$$

Equation 4.7

Where $C(\lambda_1,\lambda_2,\omega)$ is a constant coefficient, as long as $\lambda_1,\lambda_2,\omega$ remain unchanged. $C(\lambda_1,\lambda_2,\omega)$ can be calculated from $\frac{\overline{S_1}(\lambda_1,\omega)\bar{\varepsilon}(\lambda_1)}{\overline{S_2}(\lambda_2,\omega)\bar{\varepsilon}(\lambda_2)}$, but it is more accurate to determine $C(\lambda_1,\lambda_2,\omega)$ by calibrating the optical system with a known surface temperature. In this way, the combined uncertainty of the four parameters can be reduced to a single parameter of uncertainty.

By simultaneously measuring the ratio of the electrical signal changing rate from the two infrared detectors, the apparent temperature T_r can be solved with Equation 4.7. In addition, the geometric parameters are all eliminated in Equation 4.7, which improves the accuracy of the temperature measurement on a moving surface. For practical use, the voltage change rate, $\frac{\partial V(T,\lambda)}{\partial t}$, is calculated by applying the central difference numerical derivatives to discrete measurement data, $V(T,\lambda)$. To ensure that $\frac{\partial V(T,\lambda)}{\partial t}$ has a real physical meaning, the numerical step, $\Delta V(T,\lambda)$, must be 10 times greater than the electrical noise level. Therefore, the present method can only be applied to a dynamic system, and it will fail to measure a steady state surface temperature. Whereas an operating IC engine never has a steady state in-cylinder wall temperature, the present method could be useful for wall temperature measurement and the study of heat transfer.

4.3 Experimental Setup

Indium antimonide (InSb) sensors (Teledyne Judson, J10D-M204-R01M-10) were used to detect infrared radiation. The rise time of the InSb sensor is less than 10 ns. These detectors are photovoltaic and generate current when exposed to infrared radiation. They were cryogenically cooled to 77 K with liquid N2. The of the field of view angle, ω, was 11°. A transimpedence amplifier (Stanford Instruments, SR570) was used to condition the output from the InSb sensor. The amplifier gain setting of the preamplifier was 106 V/A, corresponding to a bandwidth from DC to 200 kHz. The data was recorded by oscilloscope (Agilent, MSO8104A) at a sample rate of 25 MHz. A blackbody source (Mikron, Model 310) was used for calibrating the optical system, as shown in Figure 4.1. The calibration temperature range, 90 °C to 300 °C, was selected for an operating engine wall temperature.

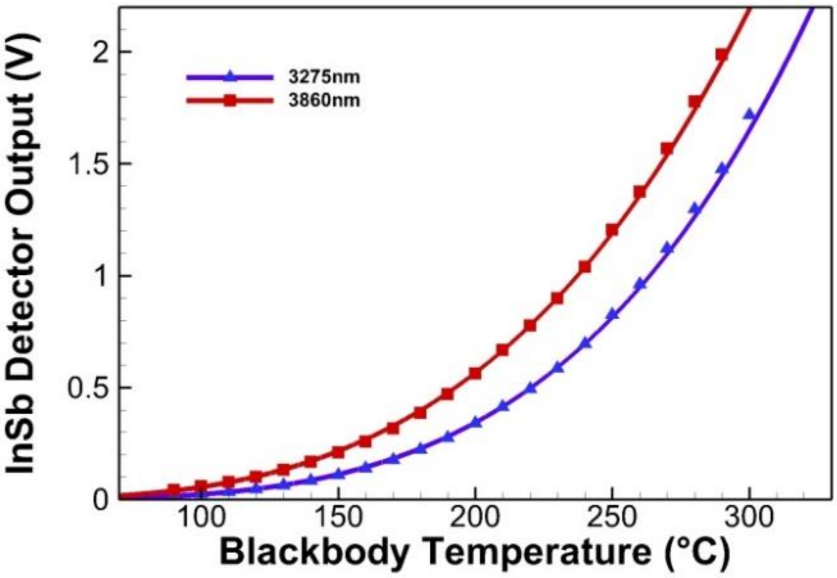

Figure 4.1: Infrared detector calibration curves. The measurement data points are curve fit using equation 1. The off set V_b has been deduced from measurement data.

As shown in Figure 4.2, a spherical mirror (f=200 mm) is used to gather light and focus it onto an InSb sensor through a 3.750 μm long pass filter which acts as a beam splitter. The signal gathered by the mirror is thus separated by wavelength and made incident to the two InSb detectors. At the focal point, the interrogated target area is estimated to be approximately 3 mm in diameter. The beam splitter, spherical mirror, and two InSb detectors are mounted to the same optical board in fixed positions to maximize alignment stability. The reflecting optics used are first surface gold coated, due to their high reflectivity (>90%) over a broad IR range. A 45-degree gold mirror is used on the engine and is also included in the optical path during calibration.

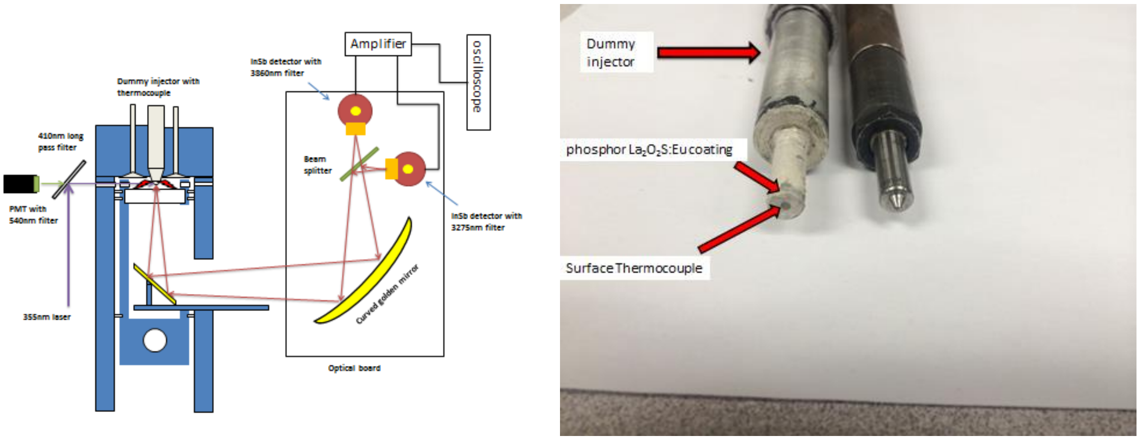

Figure 4.2: Simultaneous temperature measurements setup on engine

A concern when observing surface emission is interference from participating media along the line-of-sight, between the sensor and the surface. Among the major combustion species, both CO_2 and H_2O are IR active as a result of their having vibrational bands in the mid-IR range. Figure 4.1 shows a modeled CO_2 and H_2O emissivity spectrum generated from HITRAN model data [111]. From those spectra, it is clear that to avoid interference from these species, infrared emission should be observed at wavelengths between 3 µm and 4 µm, or longer than 4.8 µm. However, as shown in Figure 4.2, the sapphire window transmissivity cuts off at 4.8 µm. To avoid both the CO2 and water vapor emission bands, while retaining high transmissivity for the sapphire window, two filters of center wavelength 3.275 µm (bandwidth ±100 nm) and 3.860 µm (bandwidth ±80 nm) were selected, as shown in Figure 4.3. In addition, the wavelengths were selected to provide maximum temperature sensitivity at expected engine temperature, as shown in Figure 4.4.

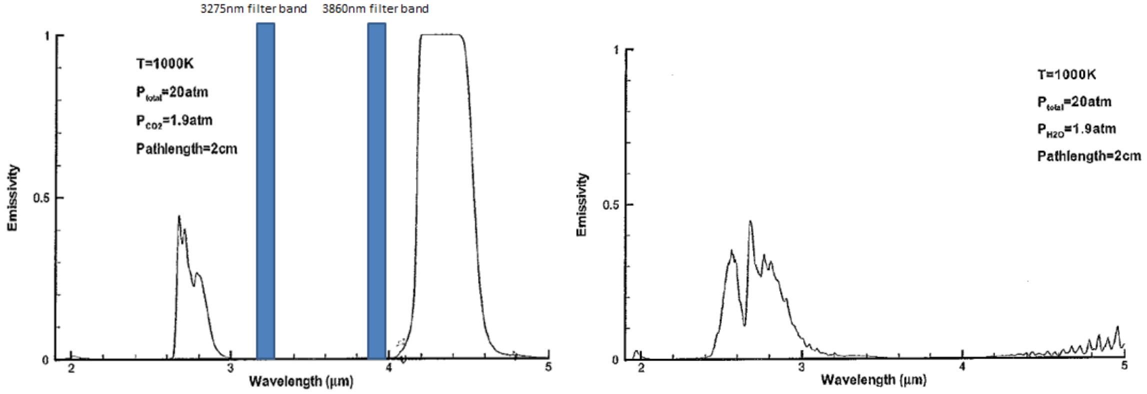

Figure 4.3: Emissivity of Isothermal Layer CO_2 and H_2O in Air Predicted by Line-by-Line Model using HITRAN Data [111]

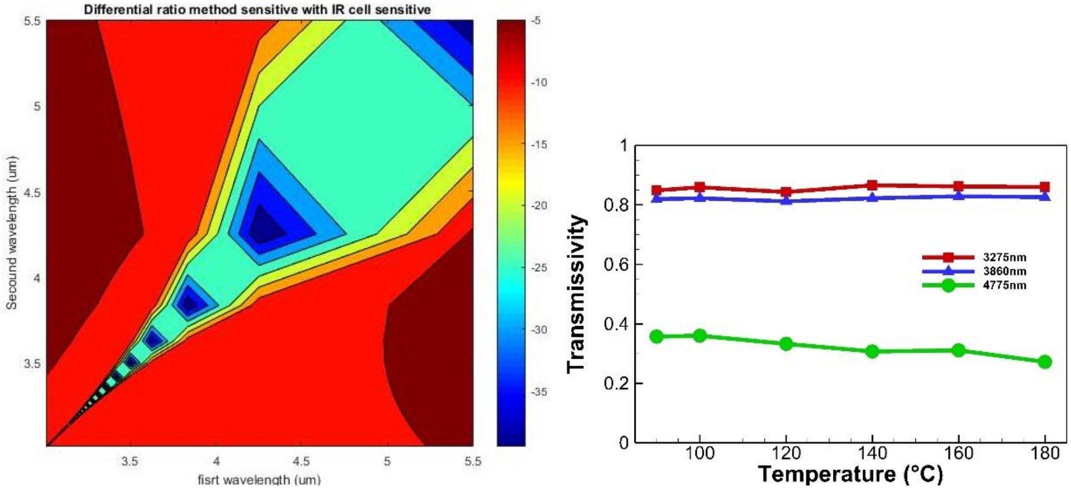

Figure 4.4: Left figure is differential ratio two-color method sensitivity at 100 ºC. Right is engine optical window transmissivity.

A single-cylinder, direct-injection optical research engine (AVL, 5402) was used in these experiments. The detailed engine specifications are shown in Table 3.1. The cylinder pressure was measured by an un-cooled piezoelectric pressure transducer (AVL, GH-12D) mounted in the cylinder head. Apparent heat release rates were calculated from high-resolution pressure data applying the analysis of Heywood [112]. The engine experiment were conducted at 1200 rpm engine speed. The engine was preconditioned by circulating coolant and lubricant oil at a temperature of 90 °C to simulate real vehicle thermal conditions. A sonic nozzle was used to control intake air mass flow rates. In addition, a closed-loop feedback temperature controller and a 2.5 kW heater were used to control the intake temperature. Experiments were run with a sweep of intake boost pressures of 1.1 bar, 1.25 bar, and 1.5 bar at constant intake temperature 60 °C. In addition, a closed-loop feedback temperature controller and a 2.5 kW heater were used to sweep the intake temperature between 60 °C, 80 °C, and 100 °C at a constant intake air mass flow rate of 6.25 g/s.

There were two steps of engine experiments. The first step was validation of the present two-color method by simultaneously measuring the surface temperature using a two-color thermometer, a fast-response coaxial thermocouple (Medtherm, model TCS-061-K-2.00-CR-GGS2-B1CSR-BA, K-type), and a laser induced phosphorescence method in a “motored” engine, in which the engine was driven by an electric motor without combustion. As shown in Figure 4.2, the coaxial thermocouple was mounted flush with a dummy injector tip (7 mm in diameter). The two-color thermometer was focused onto the thermocouple through a sapphire piston window having thermal properties similar to that of the metal piston. The thermocouple signal was amplified by an analog K-type thermocouple amplifier (Analog Devices AD8495). The bandwidth of the thermocouple signal was DC to 10 kHz, which had a relatively slow response compared to the two-color sensor. The differences between the IR measurements and the thermocouple measurements were compared to the theoretical uncertainty analysis. In addition to the surface thermocouple, a laser-induced phosphorescence (LIP) technique was also used to the measure surface temperature of the dummy injector tip.

For the second step of the experiment, the present two-color method was used to measure the piston surface temperature with engine combustion. A microscale multilayer optical window coating was developed that allows the optical measurement of in-cylinder surface temperature under combustion conditions. Figure 4.5 shows the optical window with the multilayer coating used in the present study. The surface roughness of the sapphire window was intentionally increased to 1.5 μm to reduce reflectivity. A 70 nm SiO2 layer was used as binder and stress relieving layer. The 0.9 μm Si3N4 layer acted as an anti-reflection coating, and the 1.1 μm Ti layer was used for blocking all emissions from combustion. On the top, a 300 nm SiO2 layer was used to protect the Ti layer from being oxidized by combustion gas. The SiO2 layer and Si3N4 layer were deposited by Plasma-enhanced chemical vapor deposition (PECVD), and the Ti layer was coated by electron beam (e-beam) deposition. The coated optical window was used as an engine piston, and IR sensors measured radiation of the coating through the sapphire side, while combustion emission was blocked by the coating. The transmissivity of the present coating is less than 1%.

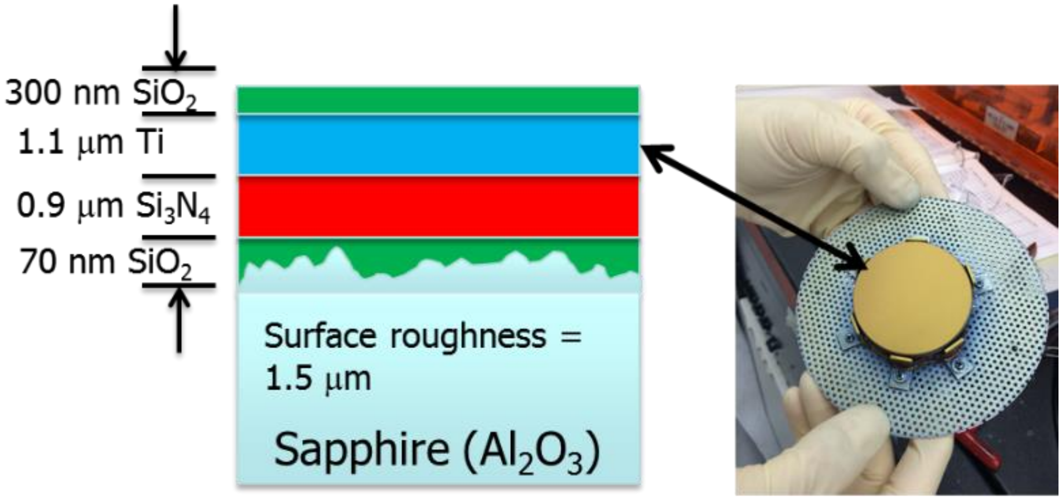

Figure 4.5: Multilayer coating on optical window

4.4 Results and Discussion

A. Uncertainty of two-color pyrometry

The uncertainty of the present two-color pyrometry can be considered as follows:

$$\epsilon_T = \sqrt{\left(\frac{\partial T}{\partial V_1}\epsilon_{V1}\right)^2 + \left(\frac{\partial T}{\partial V_2}\epsilon_{V2}\right)^2 + \left(\frac{\partial T}{\partial C}\epsilon_C\right)^2 + {\epsilon_n}^2}$$

Equation 4.8

Where $\boldsymbol{\epsilon_T}$ is the uncertainty in the temperature measurement. $\boldsymbol{\epsilon_{V1}}$ and $\boldsymbol{\epsilon_{V2}}$ are the electronic signal uncertainties due to electrical noise. $\boldsymbol{\epsilon_C}$ is the uncertainty in the calibration coefficient due to variation in the surface property during the experiments, and the calibration curve fit error. $\boldsymbol{\epsilon_n}$is the numerical error. The uncertainty of universal constants have been ignored.

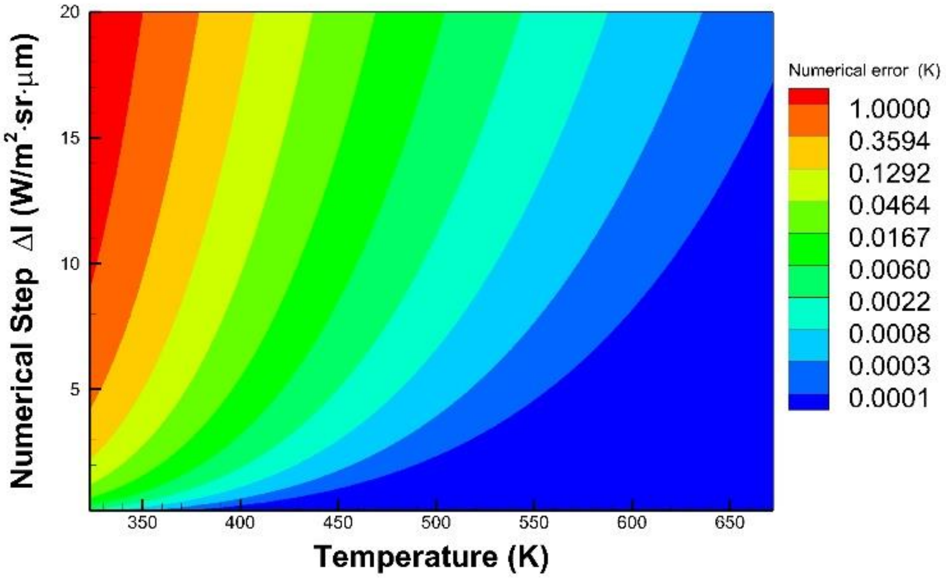

Figure 4.6: Numerical error

Figure 4.6 shows the calculated numerical error, ϵ_n, as a function of temperature and the numerical step, which is normalized with the optical system sensitivity. The numerical error increases exponentially as the numerical step increases. However, as mentioned previously, the numerical step has to generate an electrical signal 10 times greater than the electrical noise. For the constant numerical step, the numerical error decreases as the temperature increases. The numerical step, $\Delta I = 11.2\ \frac{W}{m^2 \cdot sr \cdot \mu m}$, was chosen for the present work (The equivalent $\Delta V = 0.02\ V$), and the numerical error, ϵ_n, is less than 0.5 K within the 363 K to 600 K temperature range.

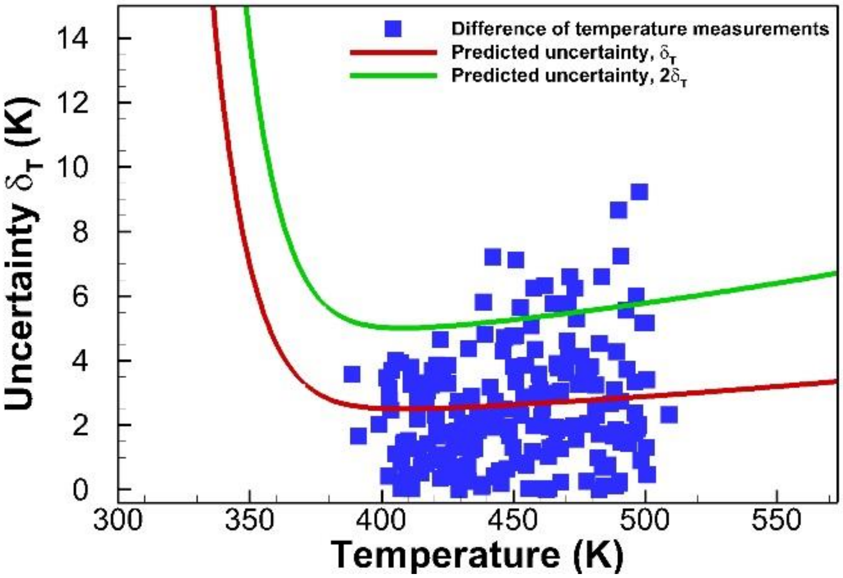

Figure 4.7: Temperature measurements uncertainty. The solid line is a prediction from equation 8. Dots are the temperature differences between the thermocouple and two-color pyrometry measurements.

As shown in Figure 4.7, the uncertainty of the two-color IR pyrometry is calculated from Equation 4.8. For temperature measurements, less than 370 K, the major uncertainty source is electronic noise, but the effects from electronic noise quickly decay as temperature increases. The lower limit of the present method is around 360 K, where the signal-to-noise ratio is less than 10. For high-temperature measurements, the major source of uncertainty is the calibration coefficient, $\boldsymbol{\epsilon_C}$, and its effects increase as the temperature increases. It is very hard to find the precise value of uncertainty in the calibration coefficient because the surface property may vary during the experiments. An empirical number, 3% uncertainty in calibration coefficient, was assumed in Equation 4.8 to calculate temperature measurement uncertainty for the present work. The two-color IR pyrometry and thermocouple have different response times, so the engine cycle average temperature is used to find the measurement difference between the two techniques. As shown in Figure 4.7: Temperature measurements uncertainty. The solid line is a prediction from equation 8. Dots are the temperature differences between the thermocouple and two-color pyrometry measurements. The maximum measurement difference is about 10 K. In addition, the measurement difference has a wide scatter at higher temperatures, where more uncertainty is expected. It may seem that the measurement difference is more sensitive to temperature compared to theoretical calculations. However, the measurement difference contains the 0.75% thermocouple uncertainty, which is not included in the two-color IR pyrometry uncertainty calculation. Over the examined temperature range (388 K to 508 K), about 57% of measurement data points are within the predicted $\pm\boldsymbol{\epsilon_T}$ range, and 93% of the measurement data points are within the predicted $\pm\boldsymbol{2\epsilon_T}$ range. Therefore, the error of the present two-color IR pyrometry is less than 1.4% for the engine in-cylinder wall temperature measurement.

B. Simultaneous surface temperature measurements

Figure 4.8 to Figure 4.10 show instantaneous surface temperature measurements using the three techniques under motored conditions at different inlet pressures but at the same inlet temperature of 60 °C. Several noteworthy observations can be made from the data. First, all three techniques are sufficiently sensitive to discern the different thermal conditions of the engine, and all temperature measurements agree within 12 °C. However, differences between the different temperature measurement techniques are clear. The thermocouple measurement shows the least temperature variation over an engine cycle; less than 5 °C, and temperature variation increases with the intake pressure.

In addition, the thermocouple measures the highest time-average temperature but also the lowest peak temperature.

On the other hand, the LIP measurements show the greatest temperature variation within the engine cycle and the highest peak temperature, which increases with the intake pressure. The temperature measured with LIP decreases more rapidly than that observed with the other two measurements. However, the maximum temperature occurred 5 degrees earlier than that observed by the other two measurements. This can partly be explained by the relatively coarse crank-angle resolution at which the LIP measurements were taken. The greater temperature variation from the LIP measurements is expected. Despite the thickness being less than an estimated 30 μm, thermal gradients exist within the phosphor layer. In these experiments, the LIP measurements represent the gas-side temperature of this layer since the laser excitation is incident to the phosphor from the side exposed to the cylinder charge. Due to the lower resolution of the temperature measurements, transient heat flux cannot be obtained from the LIP technique.

IR measurements have 20 °C to 25 °C temperature variations and have higher peak temperature than thermocouple measurements. Temperature measurements based on IR signals similarly show temperature range and mean values also increasing with the intake pressure as do the other temperature measurement techniques. Transient heat flux calculations from the IR ratio method are shown in Figure 4.11. The maximum transient heat flux is always greater than that based on thermocouple measurements, and it increases with the intake pressure. The phasing of the maximum flux is similar for each measurement. The features near 300 ATDC are believed to be a consequence of the intake valve opening.

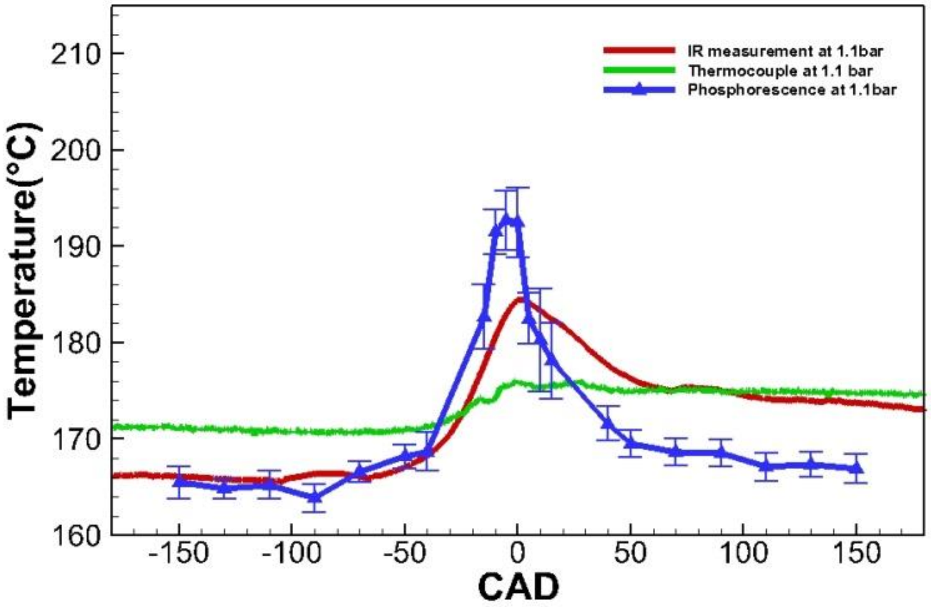

Figure 4.8: In-cylinder surface temperature measurement at1.1 bars intake pressure with constant intake temperature 60 °C

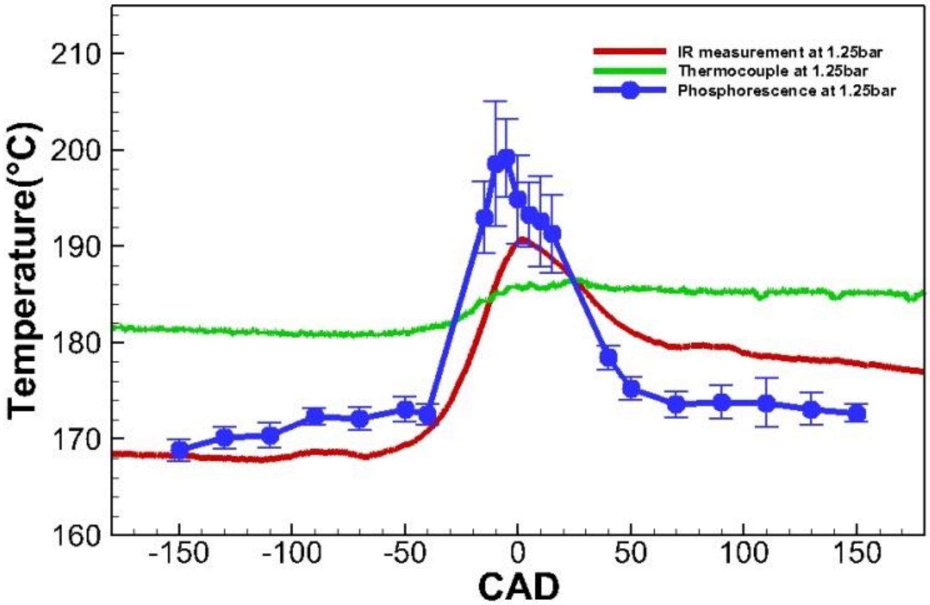

Figure 4.9: In-cylinder surface temperature measurement at1.25 bar intake pressure with constant intake temperature 60 °C

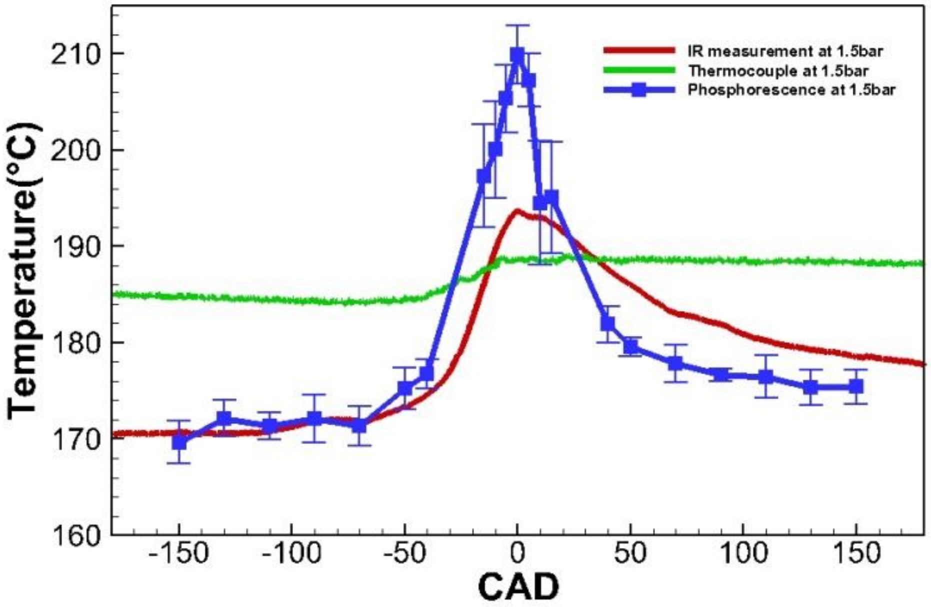

Figure 4.10: In-cylinder surface temperature measurements at 1.5 bars intake pressure with constant intake temperature 60 °C

As shown Figure 4.12, the transient heat flux calculated from the thermocouple measurements is very similar for the different engine intake pressures. According to these measurements, both the time-average temperature and the temperature range increase with the intake pressure. Therefore, according to Equation 4.1, both the steady-state and transient heat transfer component increase with the intake pressure at a constant intake gas temperature.

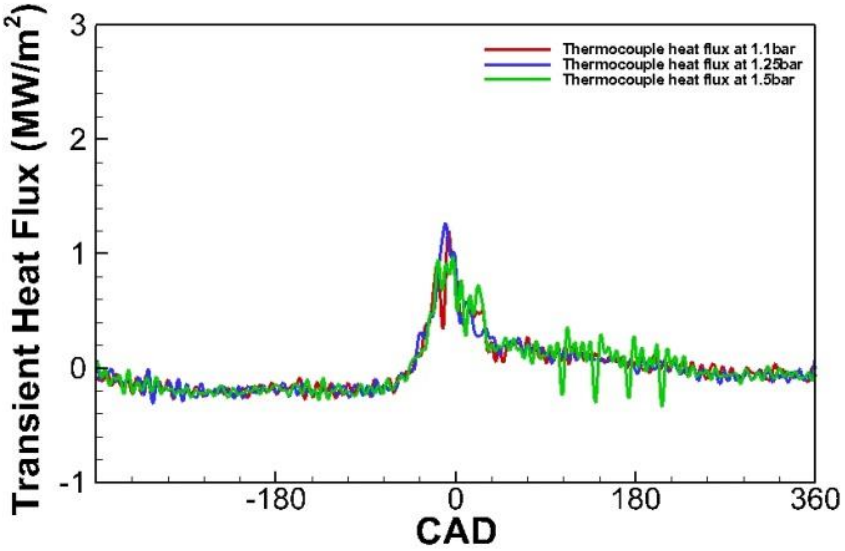

Figure 4.11: In-cylinder transient heat flux calculated from thermocouple at intake pressure 1.1 bars, 1.25 bar, and 1.5 bars with constant intake temperature 60 °C

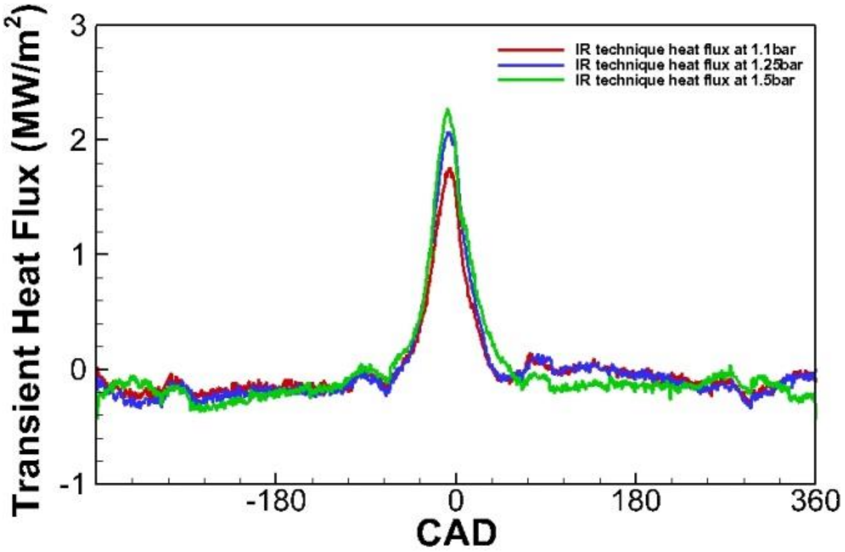

Figure 4.12: In-cylinder transient heat flux calculated from IR measurement at intake pressure 1.1 bars, 1.25 bar, and 1.5 bars with constant intake temperature 60 °C

The binder and phosphor used with the LIP technique effectively add a thermal resistance to the heat transfer process. As a result, the gas-side LIP-measured temperature variation is expected to be greater than that experienced by the actual surface. Physically, both the thermocouple and the LIP measure their own temperature. Representation of the in-cylinder surface temperature, however, requires matching of the thermal inertia, $k/\sqrt{\alpha}$, of the sensing material to that of the wall material, which can be difficult. On the other hand, InSb detectors measure the infrared intensity directly from the radiating surface and therefore can provide the actual surface temperature and heat flux.

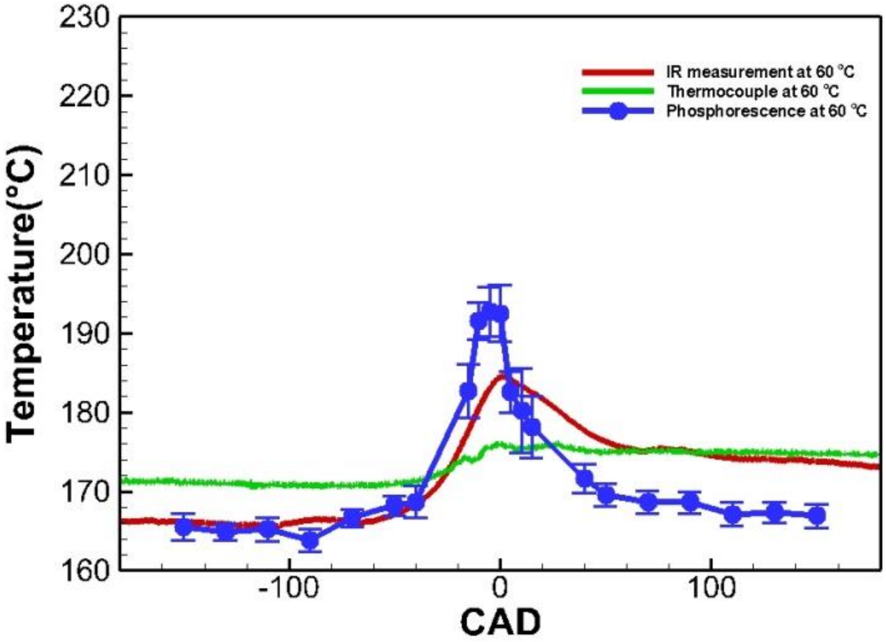

Figure 4.13: In-cylinder surface temperature measurements at intake temperature 60 °C with constant mass flow rate 6.45 g/s (19.25 kg/m^3 charge density at TDC).

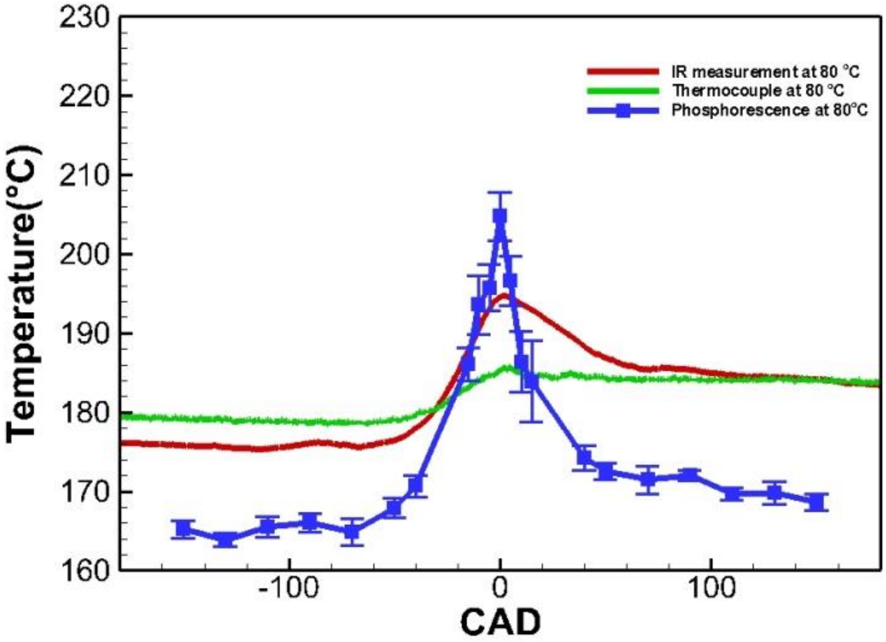

Figure 4.14 In-cylinder surface temperature measurements at intake temperature 80 °C with constant mass flow rate 6.45 g/s (19.25 kg/m^3 charge density at TDC).

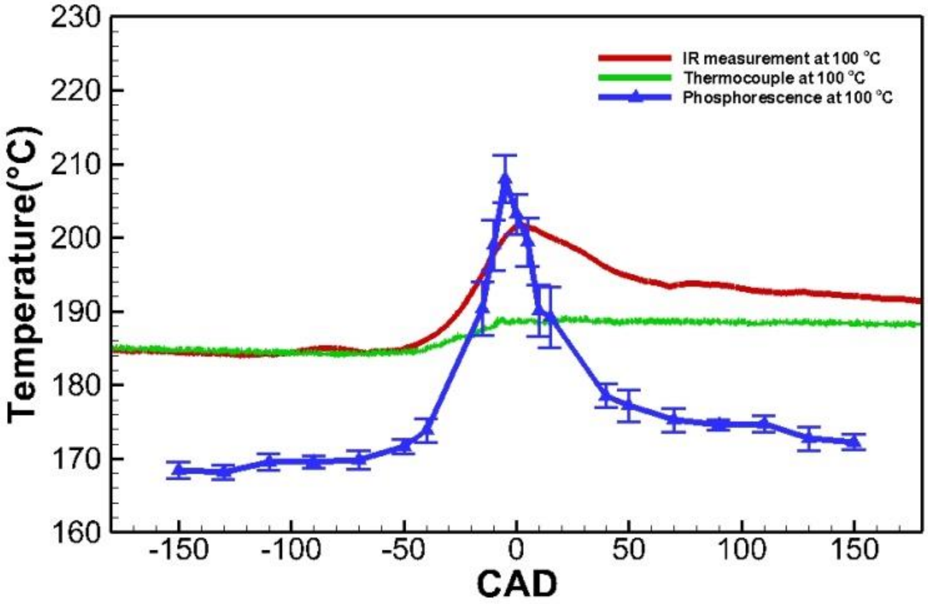

Figure 4.15 In-cylinder surface temperature measurements at intake temperature 100 °C with constant mass flow rate 6.45 g/s (19.25 kg/m^3 charge density at TDC)

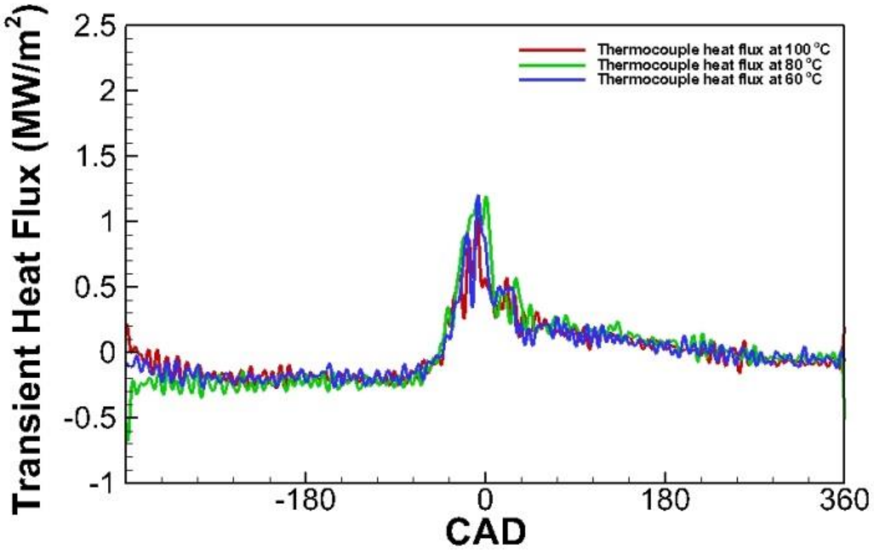

Figure 4.16: In-cylinder transient heat flux obtained from thermocouple measurement at intake temperature 60 °C, 80 °C, and 100 °C with constant mass flow rate 6.45 g/s (19 kg/m3 charge density at TDC).

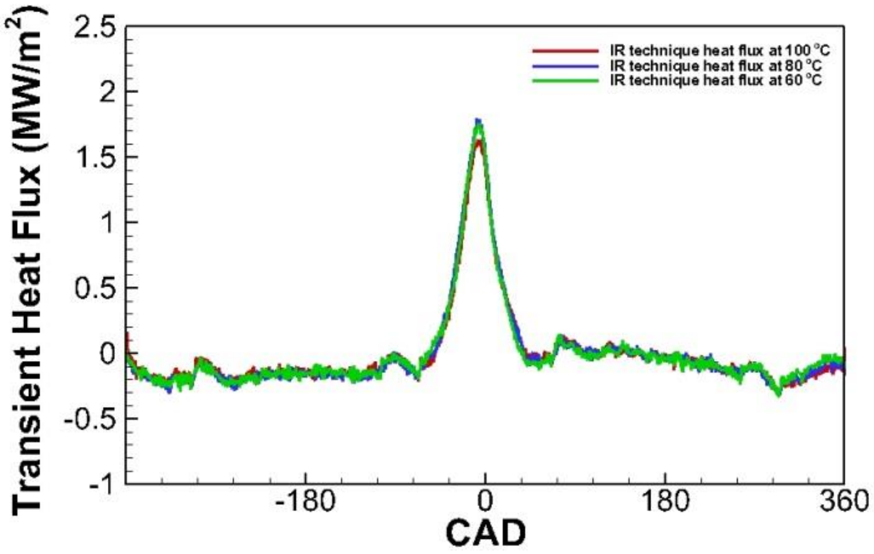

Figure 4.17: In-cylinder transient heat flux obtained from IR measurements at 60 °C, 80 °C, and 100 °C intake temperature with constant mass flow rate 6.45 g/s (19 kg/m^3 charge density at TDC).

Figure 4.13 to Figure 4.15 show the surface temperature measured during motored cycles at different inlet temperatures but with constant charge density 19 kg/m^3 at TCD. The thermocouple and IR measurements show a similar temperature range over the cycle for all three intake temperatures, 5 °C and 20 °C, respectively. The IR measurements show a monotonic increase with the intake temperature although the increase is less clear in the thermocouple and LIP results. All temperature measurements agree within 15 °C. Since the effect of temperature on the convection coefficient at a fixed density is minimal, transient heat flux does not change as the intake gas temperature increases, as shown in Figure 4.16 and Figure 4.17. The heat flux calculated from the IR diagnostic is similar for the different intake gas temperatures, with the peak heat flux slightly lower for the 100 °C intake gas temperature. Blowby occurring at the elevated temperatures is believed to be responsible for the reduced flux, as charge expansion reduces the temperature gradient between the gas and the surface, reducing flux. Similar behavior is found for the transient heat flux obtained from the thermocouple readings. Again, however, the maximum heat flux obtained from the thermocouple is less than that obtained from the IR diagnostic by nearly a factor of two.

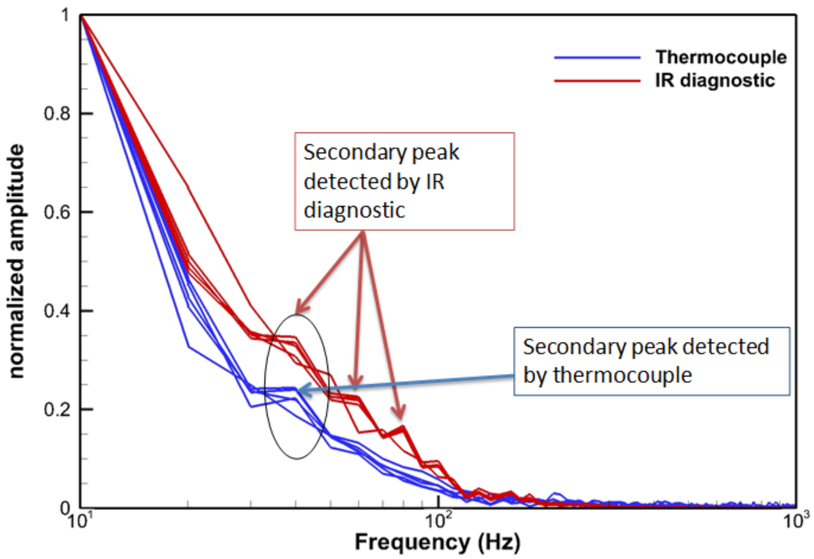

Figure 4.18: All temperature measurement results in a log scale frequency domain for thermocouple and IR diagnostic.

A significant advantage of the IR surface temperature diagnostic is its fast response time and ability to capture rapidly fluctuating temperature changes. To investigate the bandwidth of this technique with respect to the thermocouple, Figure 4.18 shows all the temperature measurements obtained by the thermocouple and the IR diagnostic in the frequency domain, plotted on a log scale. Signal magnitude decays with frequency, with thermocouple temperature decreasing at a greater rate than that measured by the IR diagnostic. The intake condition does not affect the surface temperature response in the frequency domain. For each technique, the results from different intake conditions overlap. The maximum magnitude is at 10 Hz, which corresponds to the fundamental or engine frequency. However, there are several secondary peaks at higher frequencies. In Figure 4.18, inside the circle, a secondary peak is evident at around 40~50 Hz, which is detected by both thermocouple measurements and IR diagnostic measurements. Only the IR diagnostic, however, detected several low magnitude peaks at higher frequencies. These were not captured by the thermocouple. This illustrates that the IR diagnostic has the capability to measure low amplitude, high-frequency temperature variations. For example, as shown in Figure 4.12 and Figure 4.17, IR measurements observe a negative heat flux near 300° ATDC, where cool intake gas starts to flow into the cylinder at high velocity. This feature is not observed by the thermocouple.

C. Measurements on a moving surface

The present two-color method is used to measure the piston surface temperature with diesel combustion. A sapphire optical window is installed on the engine piston, and the window is coated with multilayer IR blocking coating. The present coating has less than 1% (noise level) transmissivity at 1 µm to 4µm. Therefore, the combustion emission was blocked by the coating, and its effects on wall temperature measurement were ignored. In addition, the total thickness of the coating is about 2.3 µm, so the thermal inertia of the coating is very small.

Figure 4.19 shows the measurements of in-cylinder pressure and instantaneous piston surface temperature measurements. The engine crank angle degree (CAD) is an indication of the relative piston position, where 0 CAD means the position of a piston is farthest from the crankshaft. For constant 1200 rpm engine speed, the time for the piston to travel a unit CAD is equivalent to 128 µs. It is clear that instantaneous surface temperature is rapidly increasing, due to combustion, which can be captured by the present two-color IR pyrometry. A maximum 15 K temperature rise within 256 µs (2 CAD) was observed. In addition, the present two-color method is designed to suppress low-frequency background noises, but high-frequency electronic noise can still affect the temperature measurement. The instantaneous surface temperature measurement has a clear electronic noise spike, as shown in Figure 4.19. The electronic noise spike is believed to be caused by the discharge of the piezo injector because the corresponding timing is similar.

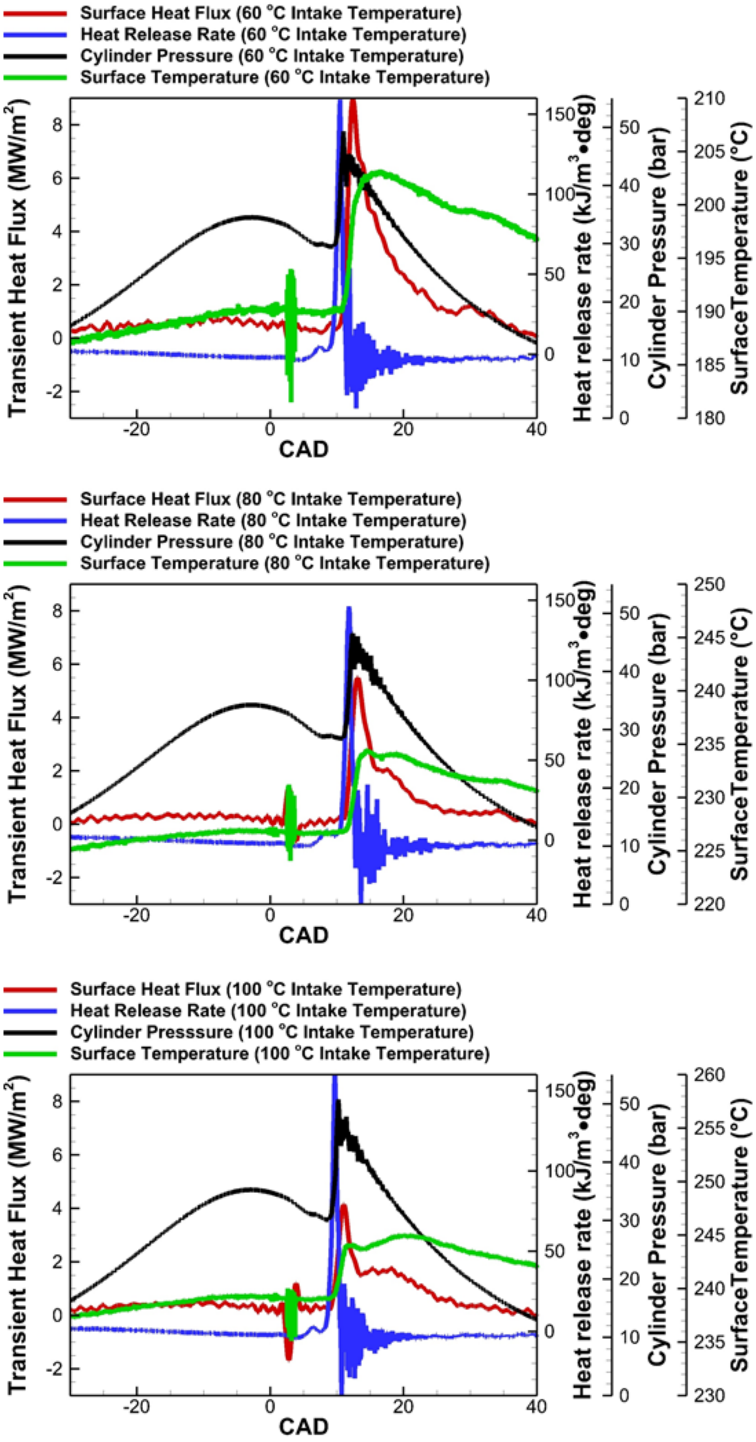

Figure 4.19: Engine in-cylinder pressure and piston surface temperature measurements versus engine crank angle degree (CAD). Transient heat flux is calculated from surface temperature base on fast Fourier transform analysis. Heat release rate is calculated from pressure measurement.

By varying the engine intake pressure, the present two-color IR pyrometry can capture the surface temperature change and varying surface heat flux under different engine loads. The magnitude of the surface heat flux increases with the heat release from the chemical reaction. It is important that a previous study using a thermocouple had difficulty distinguishing the surface heat flux when the difference of the engine load was less than 10% [113]. However, two-color IR pyrometry can distinguish the small difference in surface heat flux, as shown in Figure 4.20. Therefore, the present two-color IR pyrometry gives engine researchers and designers the capability to study the turbulent heat transfer inside and engine cylinder, which is very difficult to achieve by any other technique.

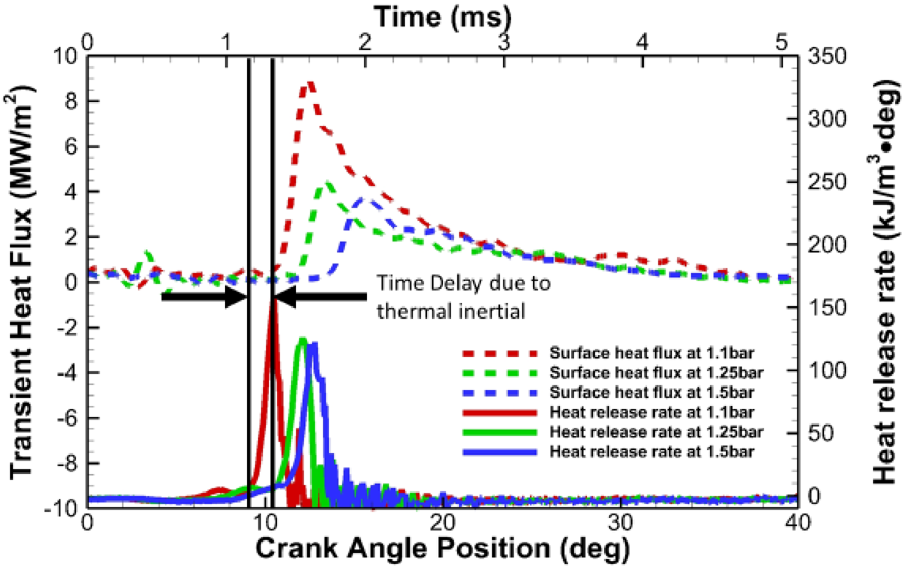

Figure 4.20: Time delay between combustion heat release and heat flux through the wall surface.

A time lag exists between the combustion heat release and the measured heat flux through the wall surface. The maximum time delay is about 0.3 ms (or equivalent 2.3

CAD at 1200 rpm). Some of the more recently designed fast response thermocouples have a reported maximum time delay of 0.64 ms (or equivalent 5 CAD at 1200 rpm) for in-cylinder surface temperature measurements under similar engine conditions [113]. Compared to those types of thermocouples, the time delay error reduced over 50% when applying the present optical coating and two-color pyrometry. This can be very helpful for measuring temperatures at high engine speed, where the same time delay error could cause a larger error in terms of the crank angle position. The source of the time delay error is mainly due to the thermal inertia of the optical coating. Increasing the thickness of the optical coating will increase the measurement error.

D. Optical Coating Failure

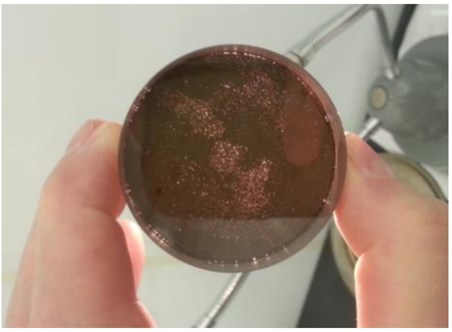

Figure 4.21: Defects on coated window after engine experiment

In practice, the present optical multilayer coating could completely block the combustion emission, but only for a limit time. After 2~3 hours of continuous engine operation, pin-hole defects appeared on the optical coating, as shown in Figure 4.21. It is obvious that combustion emissions can leak through pinhole defects and override all IR signal. There are several possible mechanisms of micro-defect formation. Nodules can grow in thick Ti coatings, and the pin holes are then initiated at the nodules when the coating is stressed by high in-cylinder engine pressure [114]. Edge delamination under comprehensive stress is due to mechanical force [115]. During an electron-beam process, molten splashing has been exacerbated by the low thermal conductivity of sapphire window, which creates nodules [116, 117]. Reducing surface roughness can minimize or eliminate nodular growth [114] and increase the life time of the coating. However, further work is needed to completely resolve optical coating failure under high pressure, high temperature, and the combustion environment.

CHAPTER 5 : NEAR WALL TEMPERATURE DISTRIBUTION FOR ENGINE RECIPROCATING FLOW

5.1 Introduction

The current Law of the Wall is based on steady state fully developed boundary layer flow. However, the IC engine flow speed is less than 10 m/s [118], and the mean flow speed can be as low as 1 m/s [118]. It is widely known that engine flow has a low Reynolds number. On the other hand, almost all engine CFD simulation is performed under the assumption that IC engine flow is a fully developed turbulence flow. This assumption may contradict the low Reynolds number flow condition. According to previous studies, researchers have to add compression efforts and non-isotropic flow to modify the Law of the Wall for IC engine simulation [119], but it has been pointed out that the prediction still does not fully agree with experimental measurements [120]. Therefore, it is very important to investigate the boundary layer phenomenon inside the engine. The planar temperature-map image offers a tool for understanding the nature of the engine in-cylinder thermal boundary layer.

Planar Laser-induced fluorescence (PLIF) is widely used for visualization of ignition centers in SI engines [121], flame propagation [122], the fuel-to-air ratio [122], and gas temperature inside IC engine [123]. Commonly used PLIF tracers for engine research include 3-pentanone, toluene, and acetone. In this study, toluene is chosen. The excitation wavelength of toluene is 240 nm~290 nm [124]. A 266 nm wavelength excitation source was used in this study. The properties of the $S_0 \rightarrow S_1$-transition in toluene vapor is temperature-dependent [124], so toluene fluorescence can be used in gas temperature measurements. Common PLIF temperature image technology uses the ratio of two different wavelength band image frames to eliminate the variation in intensity due to concentration, pressure, and excitation effects [123]. However, in this study, a spectrum-based single-line PLIF technique was used for good precision and reliability. The PLIF was used to measure and study the in cylinder near wall gas temperature profile at different CAD and gas densities. In addition, unlike the hydrodynamic boundary layer, the thermodynamics boundary layer profile requires not only measuring gas temperature, but also wall surface temperature, where the hydrodynamic boundary layer can simply assume that the velocity at the wall is zero for non-slip conditions. The wall temperature (boundary layer condition) was measured by the two-color IR technique.

The critical Re number is a very important concept for turbulence flow. When the local Re number is greater than the critical Re number, the turbulence is fully developed. On the other hand, laminar flow and transition flow have a local Re number that is less than the critical Re number. It is well known than the critical $Re\ (Ux/v) = 1 * 10^4$ for flat plate flow, and critical $Re\left(\frac{UD}{v}\right) = 2000$ for pipe/channel flow. However, neither Re number can be applied to the in-cylinder engine flow. Since the in-cylinder engine flow is wall bound in all directions, the in-cylinder engine flow is not an external flow (flat plate flow or boundary layer on a wing). In addition, the geometry of the cylinder and piston makes the in-cylinder engine flow complex, and a stable cross section of the flow does not exist [125]. Therefore, calculating the hydraulic diameter, D, for such a cross section is very difficult if not impossible. Previous studies have used $\frac{U\delta}{v}, \frac{k^{1/2}L}{v}, \frac{u_\tau\delta}{v}$ as the Re number to characterizable the in-cylinder flow. However, additional measurements or a model for the characterized length is required to calculate the Re number, which is not always available or practical for IC engine 3-D CFD simulation. Boundary layer thickness, δ, and boundary layer displacement thickness, δ^*, are commonly used as the characterized length scale for the boundary layer Re number [126]. Many near wall models have been developed based on the boundary layer Re number for adverse pressure gradient (APG) flow and zero pressure gradient (ZPG) flow [39, 41]. With experimental measured $\delta\, or/and\, \delta^*$ as the model input, those wall models can accurately predict the wall shear stress and gas-to-wall heat flux [41]. However, acquiring in-cylinder boundary layer thickness, $\delta\ and\ \delta^*$, requires complex experiments [127], which limits application of the Re number based the wall model, such as the power law. The turbulence length scale, L , is a quantity describing the size of the large eddies in a turbulent flow, and it is also used as the characterized length for the Re number. Turbulence length scale can be predicted by RNS or LES turbulence models and used to estimate the turbulence Re number. A reasonable prediction of the turbulence Re number can be achieved for isotropic turbulence flow, but an additional wall enhanced turbulence model is required for near wall boundary layer flow [128], such as $k-\omega$ model and mixing length model.

As described previously, traditionally defined Re numbers lack the ability to characterize in-cylinder IC engine flow. Without valid Re numbers, the scaling effects of IC engine flow cannot be appropriately obtained. Substantial studies have been done by Ozdemir and Akhavan on reciprocating flow [129-131]. Their studies concluded that four flow types exist in reciprocating flow [131]. Although their studies were based on the boundary layer on a smooth flat plate, which is an external flow condition, the Stokes Re number used in their studies may still be valid for IC engine flow [130].

$$Re_s = \frac{\bar{U}\sqrt{\frac{2v}{\omega}}}{v}$$

Equation 5.1

Where $\bar{U}$ is the mean velocity, which is parallel to the wall. v is the kinematic viscosity of the fluid, and ω is the angular speed of oscillation. The current study examined the near wall velocity and temperature profile under different Stokes Re numbers, and then the result was used to determine the turbulence level of engine reciprocating flow. The impact of this work is to improve the understanding of IC engine gas-to-wall heat transfer, investigate the scaling effect of engine flow, and helping establish a link between engine experiments and fundamental wind/water channel experiments for further development.

5.2 Theory

Because of the reciprocal motion of a piston, a periodic flow motion can be assumed to exist inside the engine cylinder. For periodic flow, Ozdemir and Akhavan have demonstrated five flow types to describe flow motion [131].

1. For $\overline{Re_s} < 280$, the flow motion is laminar [129]. The flow motion can be solved directly by Stokes' solution. The boundary layer only contains a viscous sublayer. No additional wall model is required to predict wall shear stress and gas-to-wall heat flux.

2. For $280 < \overline{Re_s} < \sim 500$, the flow motion is disturbed laminar [131]. Instantaneous velocity has small amplitude fluctuations, but the mean velocity profile maintains the laminar solution. The boundary layer contains the viscous sublayer, and the weak layer. The buffer layer exists in late accelerating and early decelerating phases of the cycle [132]. Although no wall model has been developed for buffer layer, the laminar Stokes solution is still a good predictor for wall shear stress and gas-to-wall heat flux.
3. For $\sim 500 < \overline{Re_s} < \sim 750$, the flow motion is a self-sustaining transition [131]. The mean velocity profiles depart from the laminar profile. However, a fully developed boundary layer does not exist. The boundary layer contains the viscous sublayer, the weak layer, and the buffer layer. A self-sustaining transition flow does not always exist within the given Re_s number range [129]. There are no completed theories about transition flow. The exact conditions, which are required by the self-sustaining transition, are under investigation. In addition, the turbulence Pr number increases non-linearly [133]. The log law is invalid for wall shear stress and heat transfer. Currently, the gas-to-wall heat flux cannot be predicted accurately without resolving the full boundary layer profile.
4. For $\sim 500 < \overline{Re_s} < 3460$, the flow motion is intermittently turbulent [131], the fully developed boundary layer starts to appear at the early decelerating phases of the cycle, and the rest of the cycle remains in transition flow. The law of the wall is valid for a fully developed boundary layer.

5. For $3460 < \overline{Re_s}$, the flow motion is fully developed turbulent [134]. The entire cycle has a fully developed boundary layer. The law of the wall can be used to predict the wall share stress and heat flux. The turbulence Pr number varies from 0.9~1.1 [135], which can be assumed to be constant over the entire cycle.

As described, the five flow types have been observed based on fundamental wind channel experiments. It is unclear if there is a boundary layer structure for transitional flow, but the mean velocity profile varies with the Re number. In addition, the transitional flow does not have a constant turbulence Pr number [133]. For validating the scaling effect, an average $\overline{Re_s}$ is required. For a naturally aspirated engine, it is assumed the mass flow rate is proportional to the engine speed, $\dot{m} \propto \omega$. The coordination, $\overline{U} = \left(\frac{A_{piston}}{A_{intake\ port}}\right)^n S_p$, can be applied [136] where $\overline{S_p}$ is the mean piston speed, $\frac{A_{piston}}{A_{intake\ port}}$ is the ratio between the piston cross-sectional area and the intake port cross-sectional area. The model coefficient n=0.8 was used in this study. The average $\overline{Re_s}$ for an IC engine can be rewritten as:

$$\overline{Re_s} = \frac{\overline{U}\sqrt{\frac{2v}{\omega}}}{v} = \left(\frac{A_{piston}}{A_{intake\ port}}\right)^{0.8} S_p \sqrt{\frac{2}{v\omega}} = \left(\frac{A_{piston}}{A_{intake\ port}}\right)^{0.8} \frac{l_{\text{Stroke}}}{\pi} \sqrt{\frac{2\omega}{v}}$$

Equation 5.2

Equation 5.2 revealed that $\overline{Re_s}$ is proportional to the stroke length, l_{Stroke}. The flow has more time to readjust in a reciprocal engine with a longer stroke length. For low to medium engine speed, the $\overline{Re_s}$ number is proportional to the square root of the engine angle velocity, ω. This is different from findings from the fundamental flat wall experiment because engine speed also affects the mean mass flow rate, and increasing engine speed will increase the overall velocity, which compensates for the shorter time scale. At high engine speed, the volumetric efficiency drops. The $\overline{Re_s}$ number becomse less sensitive to the engine speed, where Equation 5.2 is no longer valid. It is possible that the $\overline{Re_s}$ number decreases as the engine speed increases at extremely high engine speed, where the engine has choked flow.

To test the engine, the operation engine speed is about 600 rpm ~3200 rpm, and the estimated $\overline{Re_s}$ number for a “motored” engine is about 333 ~ 840 although combustion and injection events will increase the local Re_s number. The majority of in-cylinder near wall boundary layers are within intermittently turbulent or self-sustaining transition range. This is very different from the fully developed turbulent assumption, which most prior engine CFD simulations have assumed. To validate this theory, a comprehensive engine has been conducted to examine both the near wall velocity and the temperature profile at 1200 rpm with estimated $\overline{Re_s} = 516$.

5.3 Experimental Setup

The engine setup is described in Chapter 3. However, some piston modifications have been done to obtain the near-wall temperature and velocity profile measurements.

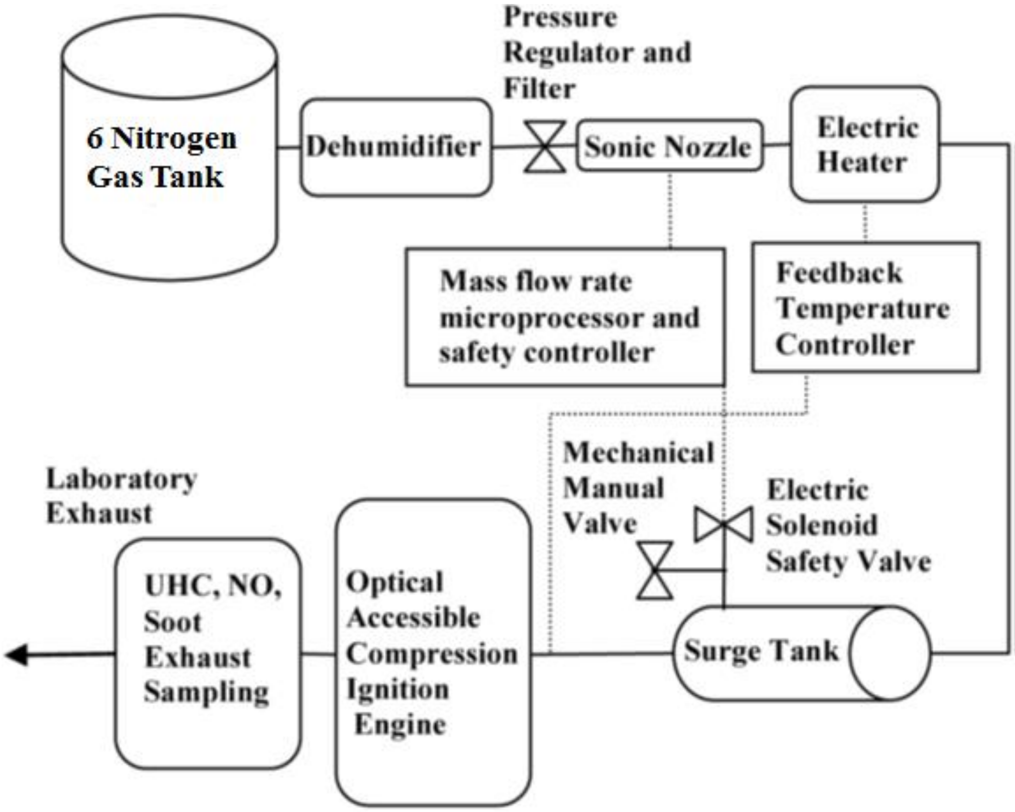

Figure 5.1: Schematic of the intake, engine, and exhaust sampling system.

Figure 5.1 shows the flow path and hardware configuration. A sonic nozzle and electric heater are used to control the inlet gas temperature and mass flow rate. six nitrogen gas cylinder are used to supply nitrogen, as shown in Figure 5.2. The nitrogen is used to eliminate oxygen quenching.

Figure 5.2: 6-cylinder N_2 and its manifold

A modified piston crown is used to allow optical access around TDC, as shown in Figure 5.3. The modified piston crown maintains similar piston blow geometry but has a 2 mm wide cjannel for laser access. After modification, the piston is 6 mm shorter, and the effective compression ratio is reduced to 7.5 from 13.8. (The geometries compression ratio is reduced to 9.1 from 15.)

Figure 5.3: Modified piston

PILF experimental setup

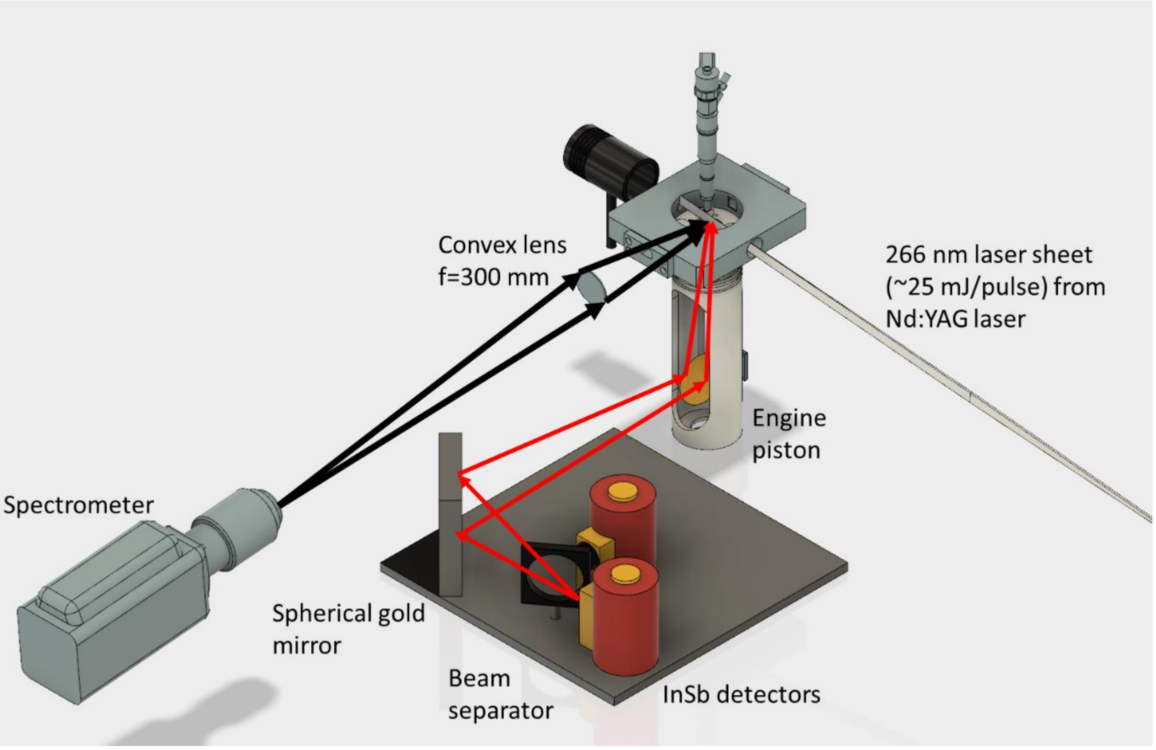

Figure 5.4: Schematic of optical setup for PILF measurements

Figure 5.4 shows the optical setup on the engine. A dual-band infrared diagnostic is used to measurement the wall surface temperature. Two indium antimonide (InSb) sensors were used to detect the infrared radiation from the engine fire deck. The InSb sensors were cryogenically cooled to 77 K with liquid N_2. The field of view angle, ω, was 11°. Two amplifiers were used to condition the output from InSb sensors, respectively. The amplifier gain setting of the preamplifier was 106 V/A, corresponding to a bandwidth from DC to 200 kHz. The data was recorded by oscilloscope at a sample rate of 25 MHz. A spherical mirror (f=200 mm) was used to gather light and focus it onto the InSb sensor through a 3.750 μm long pass filter which acts as a beam splitter. A gold first surface mirror inside the piston assembly at 45° relative to the cylinder axis reflected the IR radiation from the combustion chamber to the IR devices placed on a vibrationally isolated bench top. For more detail of the dual band infrared diagnostic temperature measurement, please refer to Chapter 4.

A 20 mm thick sapphire window is mounted in an extended piston for transmission of the IR, as shown in Figure 5.4. The top of the cylinder liner has two 12.5 mm×21 mm rectangular quartz windows in the camera view direction and two 17 mm diameter round quartz windows in the laser direction. Slotted graphite rings provide oil-less lubrication, and gapless bronze-Teflon rings are used for sealing. Compressed shop air is directed at the piston window to cool the assembly during engine operation. A 2-inch diameter UV lens combined with a camera lens magnifies the observed area. The focal length of the UV lens is 300 mm. The camera lens has a 115 mm focal length, and the aperture ratio is set to f/4.0. An ICCD camera (PI-MAX2) with a Czerny-Turner type spectrograph (Acton Research SpectraPro- 2150i) is used to measure the toluene fluorescence, and a 300 grove/mm grating is used for the measurements. The corresponding level of dispersion is 0.48 nm/pixel. The grating blaze wavelength is 500 nm. The experiments were performed with a central wavelength setting of 380 nm. The exposure time was 65 us. The spectrometer was calibrated for wavelength with a mercury light source whose spectrum is known. The spatial resolution was 50 µm/pixel. The 1200 RPM engine operating speed was chosen to match the nominal frequency of the pulsed laser, which is 10 Hz. The laser beam, characterized by a Gaussian profile, was formed into a horizontal laser sheet using a cylindrical planoconcave (f = −400 mm, Lattice

Electro Optics, UF-CC-1010-400) and spherical convex (f = 1000 mm, Lattice Electro Optics, UF-PX-50.8-1000) lens pair. Truncation of the light sheet edges with the iris served to minimize reflections within the side window mount cavities. A relatively uniform light sheet was created by isolating the middle section of the Gaussian beam profile. The laser sheet thickness was 0.77 mm prior to the engine cylinder, and the minimum laser sheet thickness was 0.25 mm at the focal point, which was inside the engine cylinder. This laser sheet was aligned to be perpendicular to the fire deck, and it passed through the channel on the piston top. In such a configuration, the spectrometer had a 100 µm×4 mm field of view inside the engine. For PLIF measurements, the 532 nm output from a pulsed Nd:YAG laser (SpectraPhysics QuantaRay Pro 270) was used with a 4th harmonic generator, which doubled frequency to 266 nm. The laser energy was 25 mJ/pulse prior to the engine, and the pulse duration was ~7 ns. The laser was used to excite the toluene vapor. The toluene was introduced by direct injection to the cylinder. The injection pressure was 800 bar, and injection timing was 250 CAD before firing TDC. In other words, toluene was injected at the intake stroke at high rail pressure, to produce a homogeneous toluene vapor could be created at measurement instant. The total injection mass was 7.2 mg/cycle. No additional additive was added to toluene, and the purity of toluene is 95%.

The toluene vapor released fluorescence when excited by 240 nm to 290 nm UV light [124]. The toluene fluorescence process is similar to that of OH PLIF.

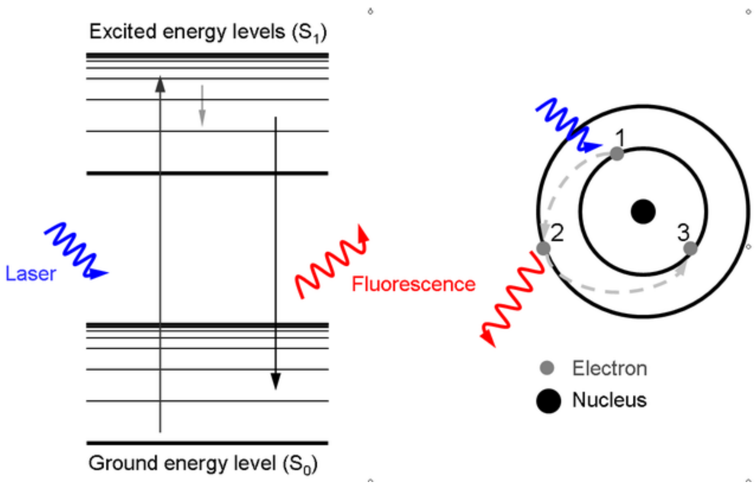

Figure 5.5: Schematic of toluene PLIF process [137]

A laser pulse excited a ground stage (S_0) toluene molecular, and the electron of the toluene molecule leapt to a higher energy orbits. The toluene molecule arrived at the excited stage (S_1). When the excited stage toluene molecule dropped to the ground state, the electron of the toluene molecule returns to its original orbit and releases a photon, as shown in Figure 5.5. The intensity of toluene fluorescence can be described by the following equation [123]:

$$S_{f,i}(T) = \frac{E}{hf_v} n\sigma(T) \int_{\Omega_\tau} \tau_i(\lambda)\phi(\lambda,T)\eta_i(\lambda)d\lambda$$

Equation 5.3

Where $S_{f,i}(T)$ is the collected intensity signal. E is the excitation laser energy, and f_v is the frequency of the excitation laser. h is Planck's constant. n is tracer number density, and $\sigma(T)$ is the absorption cross section. $\tau_i(\lambda)$ is optical device transmissivity, and $\eta_i(\lambda)$ is camera sensitivity. $\phi(\lambda,T)$ is the fluorescence quantum yield, and it is pressure-independent on the $P_{total}>0.8$ bar [88]. Ω_{τ} is the optical device bandwidth. To eliminate the effects of laser energy and toluene concentration on fluorescence intensity, a ratio method was used. A ratio of two intensities, observed at two wavelength bands, can be described as follows:

$$\mathrm{R}_{PLIF}(T) = \frac{S_{f,1}(T)}{S_{f,2}(T)} = \frac{\int_{\Omega_{\tau,1}} \tau_1(\lambda)\phi(\lambda,T)\,\eta_1(\lambda)d\lambda}{\int_{\Omega_{\tau,2}} \tau_2(\lambda)\phi(\lambda,T)\,\eta_2(\lambda)d\lambda}$$

Equation 5.4

As shown in Equation 5.4, the ratio of the PLIF intensity, $\mathrm{R}_{PLIF}(T)$, is only a function of temperature, when given a fixed optical bandwidth. Calibration of $\mathrm{R}_{PLIF}(T)$ can be used to measure the local gas temperature.

The calibration of PLIF was completed in a constant volume vessel, as shown in Figure 5.6. The constant volume has optical access similar to that of an engine. Two 12.5 mm×21 mm rectangular quartz windows were placed in the camera view direction, and one 17 mm diameter round quartz window was placed in the laser direction. The other round quartz window was replaced with a thermocouple for closed loop temperature control. The vessel was wrapped with 4 heat tape and additional heat insulation around the vessel, as shown in Figure 5.6. Each heat tape had 400 W output and was connected in parallel circuit, which gives a total 1600 W power output. A PID controller and an AC power relay were used to control and maintain a uniform gas temperature inside the vessel. The vessel was filled with 2500 ppm toluene in pure nitrogen. The vessel had 1.2 atm pressure to maintain a positive pressure balance

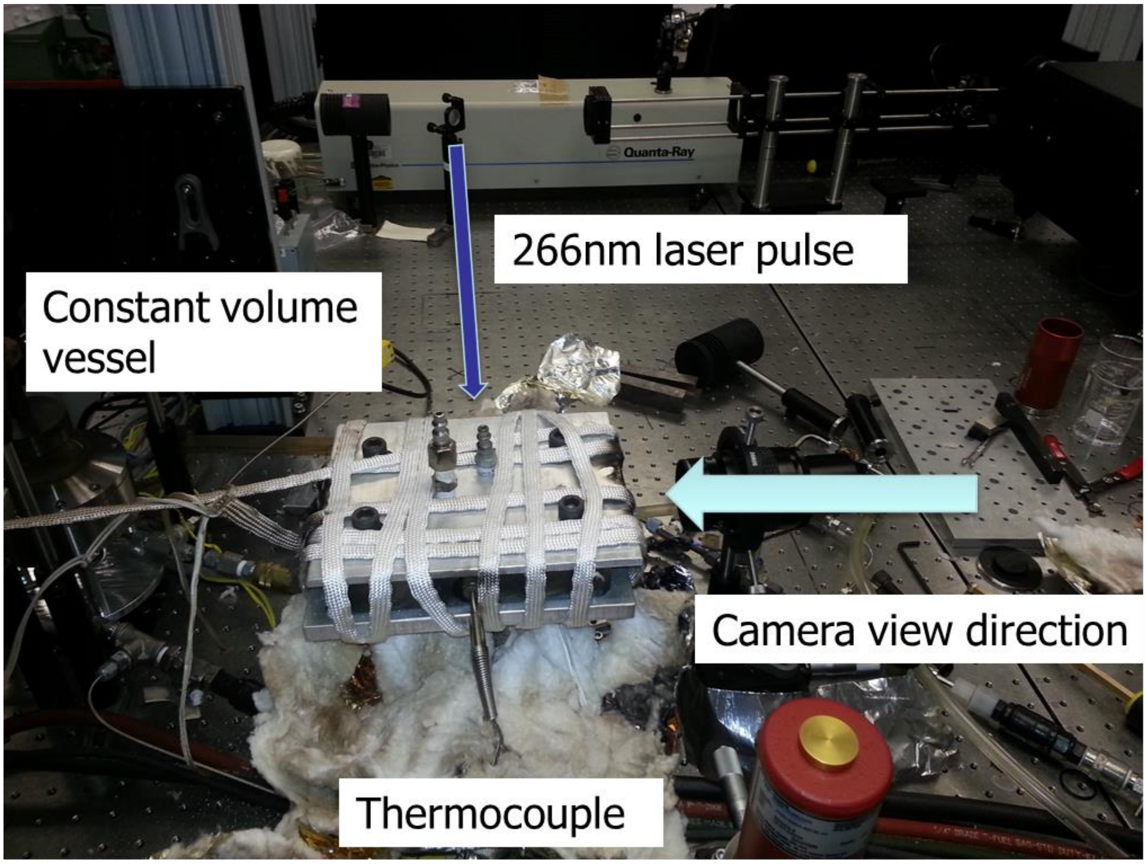

Figure 5.6: Constant volume vessel setup to calibrate toluene PLIF measurement.

Figure 5.7 shows the calibration of the toluene fluorescence spectrum. The spectrum measurements well reproduced toluene fluorescence spectrum published by early studies [124]. The toluene fluorescence red-shifts with increasing temperature, and the intensity decays with increasing temperature, as shown in Figure 5.7 and Figure 5.8.

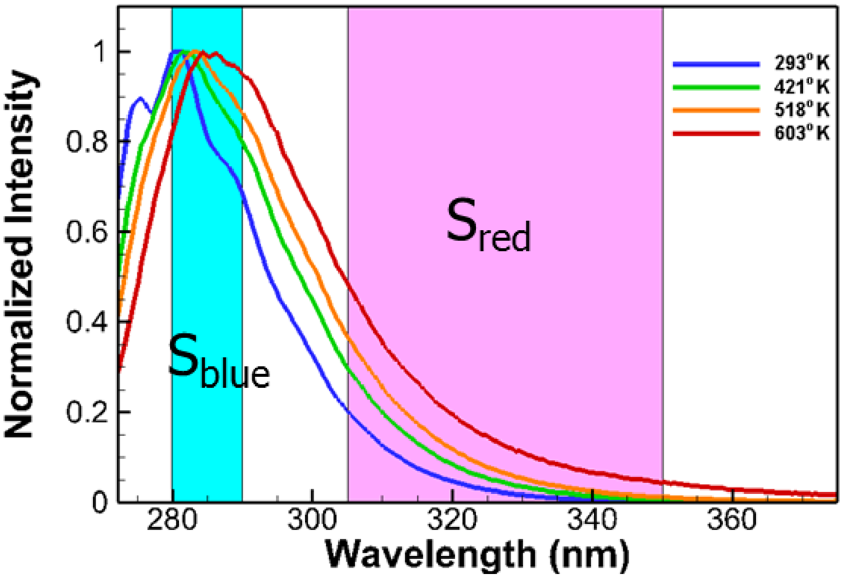

Figure 5.7: Calibration of toluene fluorescence spectrum at different temperature

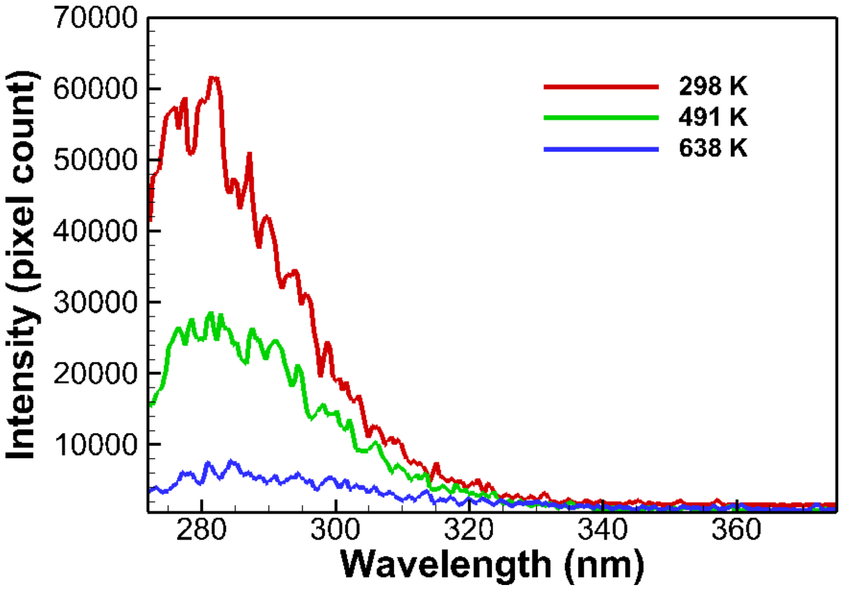

Figure 5.8: Intensity decays with increasing temperature

A ratio is calculated from S_{blue} and S_{red} . S_{blue} is the fluorescence signal integrated from 280 nm to 290 nm. S_{red} is the fluorescence signal originally integrated from 310 nm to 350 nm to obtain the linearity of the calibration curve, as shown in Figure 5.9. However, some later data was integrated from 290 nm to 320 nm for S_{red}, to obtain a ratio more sensitive to temperature near 400 K, as shown in Figure 5.9. The present PLIF measurements have ±17 K with 90% certainty for the homogeneous gas temperature.

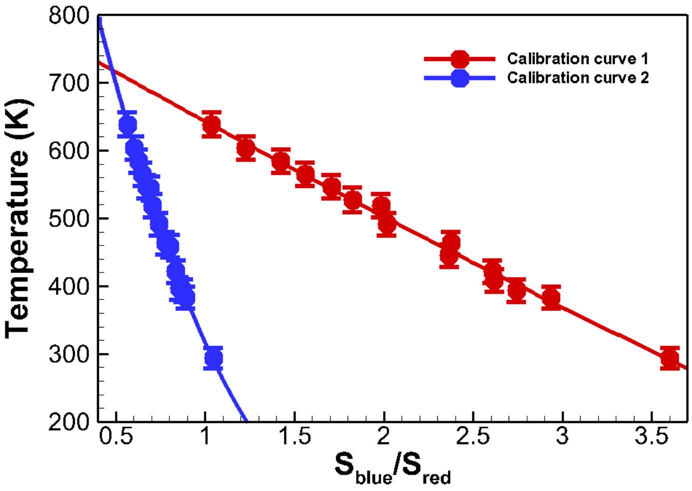

Figure 5.9: Temperature dependence of band ratio calibration curve 1. S_{blue} is fluorescence signal integrated from 280 nm to 290 nm. S_{red} is fluorescence signal integrated from 310 nm to 350 nm Temperature dependence of band ratio calibration curve 2. S_{blue} is fluorescence signal integrated from 280 nm to 290 nm. S_{red} is fluorescence signal integrated from 290 nm to 320 nm

The near wall temperature profiles are more difficult to observe than velocity profiles. Velocity at the wall can be assumed to be zero, while wall temperature requires additional measurements. In this study, the wall temperature and near wall gas temperature were simultaneously measured by the IR diagnostic and toluene PLIF, respectively. The synchronous system utilized two field-programmable gate array microprocessors (National Instruments cRIO/DRIVVEN Inc). One cRIO microprocessor was used to trigger a delay generator (Stanford Research DG535), and the delay generator then provided triggers for the laser Q-switch, and the laser lamp. The other cRIO microprocessor was used to trigger the ICCD camera gate, injection, and oscilloscope. The ICCD camera captured 100 frames for each CAD, and oscilloscope recorded 100 cycles of IR signals. The feedback of the camera signal was recorded by a high-speed data acquisition system (AVL IndiCom). The cylinder pressure was measured by an un-cooled piezo-electric pressure transducer (AVL-GH-12-D), and the injection pressure was measured by a strain gauge pressure transducer (AVL SL31D-2000). These sensor signals were also recorded by the IndiCom data acquisition system, which was triggered at 0.1 CAD intervals and synchronized to the engine position by an optical encoder wheel mounted on the crankshaft.

PIV experimental setup

The PIV experiment had the same general engine setup. A TSI PIV system was used in this experiment. As shown in Figure 5.10, the CCD camera observes the PILF signal through a telemicroscope, which has a 115 mm~300 mm adjustable focal length. The camera lens has 125 mm focal length, with the f-number set to f/2.8. The spatial resolution was 2.5 μm/pixel, and the effective field of view was 4.2 mm×4.6 mm. Same as in the PLIF experiment, the camera viewed from one of the rectangle quartz windows, as shown Figure 5.10. However, the laser sheet was introduced from the bottom 45-degree mirror and reflected up towards engine fire deck. The laser pulse was generated by the double pulse Nd:YAG laser (Evergreen). The pulse energy was 48mJ/pulse, and pulse duration was ~10 ns. between two laser pulse had a 10 μs time delay. The laser sheet was created by the same lenses setup as with PLIF. Both the laser and the camera was controlled by a synchronizer (LaserPulse™ Synchronizer Model 610036). The synchronizer itself was triggered by a cRIO microprocessor.

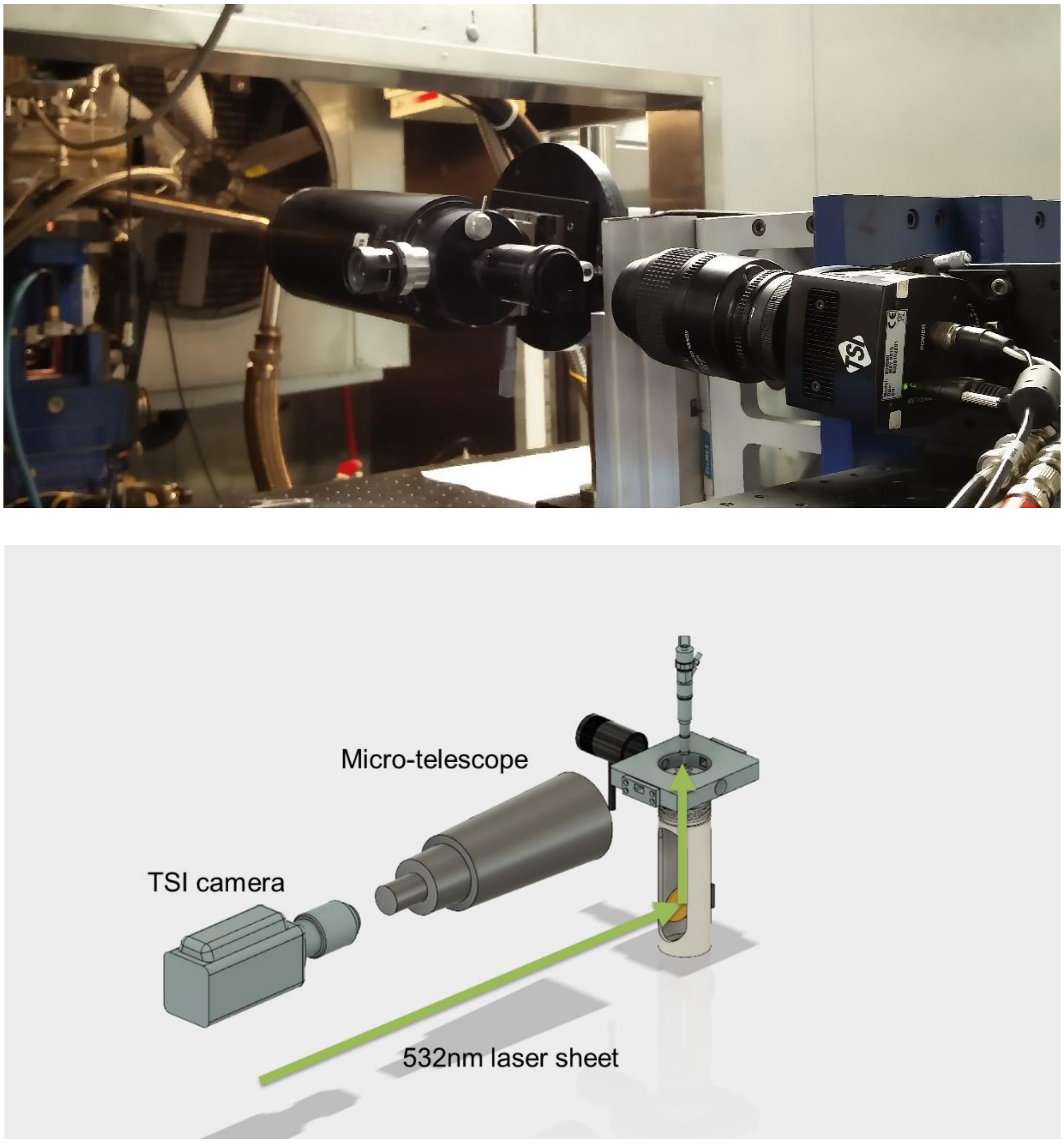

Figure 5.10: Schematic of Micro PIV optical setup

As shown in Figure 5.11, the experiment chose a flat surface near the fire deck, so a ZPG flow condition can be best represented. Both the PLIF and PIV laser sheets were on a plane vertical to the fire deck and 3.5 mm away from the center of engine cylinder, as shown in Figure 5.11. The single-line PLIF measured the near wall gas temperature 8 mm away from the center line to the right on the laser plane, and the PIV field of view covered the same area, as shown in Figure 5.11.

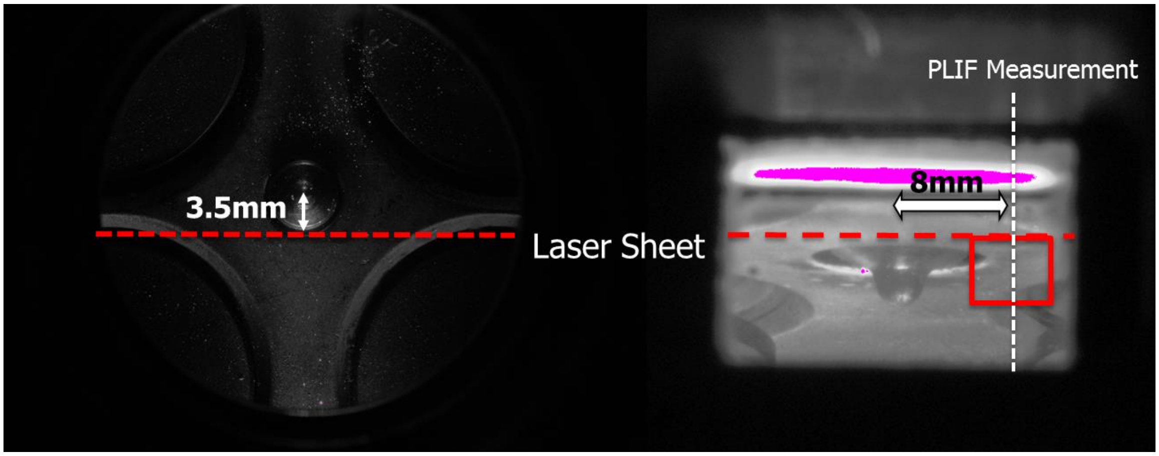

Figure 5.11: Measurements location

Diesel droplets were used as seed particles. The particles were directly injected into the cylinder at a 400 bar injection pressure, and the injection time was 250 CAD before firing TDC, which was the same as in the PLIF experiment. The estimated Stokes number was 0.034 at TDC. The other engine condition remained the same as in the PILF experiment setting for recreating the same engine flow condition. 50 pairs of PIV images were captured at each examined CAD. The image processing was done by commercial software INSIGHT™ 4G. For each examined CAD, background images were generated by a minimal pixel count of 100 images. A background subtraction was done at each examined CAD to reduce the effect of varying seed density. To further reduce wall reflection, the cylinder head was painted black, as shown in Figure 5.12. For best accuracy, the digital image correlation (DIC) method was used for image correlations.

Compared to fast Fourier cross-correlations, the DIC method has a slightly better performance in solving nonlinear correlations, but the DIC method is computationally more expernsive [138]. The interrogation window was 64×64-pixel with half overlap, so each interrogation window had at least 4 to 5 particles for image correlation. Additionally, for each interrogation window, the mean and root mean square values of velocity were calculated for the adjacent surrounding velocity fields. The vector would be removed if its deviation from the surrounding mean velocity was greater than the root mean square velocity. An interpolated mean velocity vector was used to replace the removed erroneous vector or fill any no-solution grid. Finally, the ensemble average velocity field was calculated by MATLAB code.

Figure 5.12: Cylinder head painted with black color.

5.4 Results and Discussion

All experiments had 1200 rpm engine speed, and the engine was fed with pure nitrogen. Figure 5.13 and Figure 5.14 show near wall temperature measurements at 0.8 bar intake pressure. The intake means the mass flow rate was 6.75 g/s, and the gas temperature was 60 ºC (333 K). The engine coolant and oil temperature were 90 ºC (363 K). The estimated $\overline{Re_s} = 446$ can be calculated with Equation 5.2. For this experiment, the slit on the piston had not yet been cut. Therefore, the optical access was not available near TDC at that time. Relatively smooth near wall temperature profiles were observed. This may partially be caused by the fact that the temperature was not sensitive to the ratio of the selected wavelength-bands in calibration curve 1. Therefore, the toluene PLIF was recalibrated, and the calibration curve 2, which is more sensitive to temperature, was adapted for later experimentation. y is the distance in the wall-normal direction. $\bar{T}$is the average temperature of 100 cycles. The gas temperature next to the wall, $\lim_{y\to 0^+} \overline{T(y)}$, varied toward the wall surface temperature, but it did not reach the wall surface temperature, as shown in Figure 5.14.

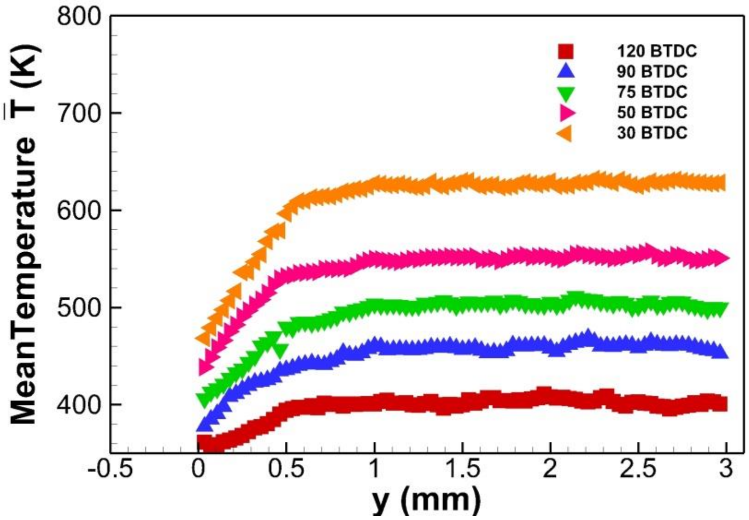

Figure 5.13: Near wall temperature measurements in compression Stroke, using calibration curve 1. The intake mass flow rate was 6.75 g/s and estimated $\overline{Re_s} = 446$

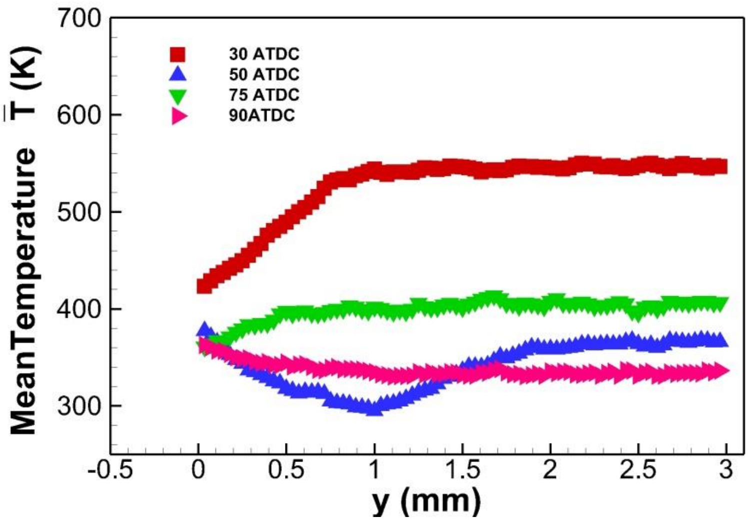

Figure 5.14: Near wall temperature measurements. Using calibration curve 1. The intake mass flow rate was 6.75 g/s, and estimated $\overline{Re_s} = 446$.

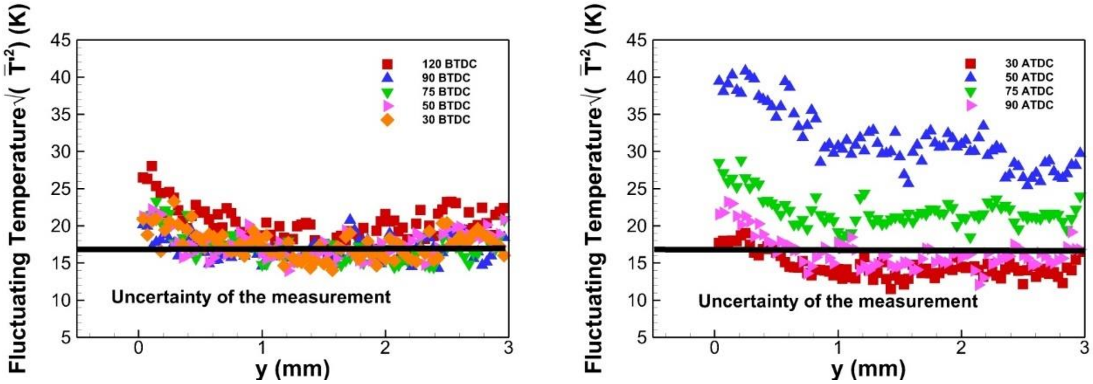

Figure 5.15: Instantaneous temperature varies from mean temperature.

Figure 5.15 shows that the instantaneous temperature varies from the mean temperature. In this study, the instantaneous temperature variation can be decomposed to turbulence temperature fluctuations ($T'_{turblnce}$), cycle-to-cycle variations (${T'_{cycle}}^2$), and experimental uncertainty ($\epsilon_{uncertainty}$).

$$T_{sd} = \sqrt{{T'_{turblnce}}^2 + {T'_{cycle}}^2 + {\epsilon_{uncertainty}}^2}$$

Equation 5.5

From all the examined crank angles, the spare mean root of the temperature variation collapsed on top of experimental uncertainty, except for 50 ATDC and 75 ATDC. Therefore, the experimental uncertainty, which is determined from homogeneous gas temperature measurements, was still valid in the engine experiment. However, with presenting PILF measurement accuracy, the turbulence temperature fluctuations cannot be calculated from the instantaneous temperature variation. On the other hand, the turbulence temperature fluctuations must be small enough to have little impact on instantaneous temperature variation. From the data is safe to estimate that turbulence temperature fluctuations were less than 17 K, except 50 ATDC to 75 ATDC. The potential temperature difference between gas and cylinder wall was about 300 K around TDC, so the percentage of turbulence temperature fluctuations, T', was less than 6% around TDC. This is significantly less than the 10%~20% turbulence velocity fluctuations, u', which were reported by other researchers [139]. The smaller turbulence temperature fluctuations mean that there is smaller turbulence heat flux, $< u'T' >$. This is evidence to prove that the near wall temperature profiles are not proportional to the near wall velocity profiles in the IC engine. The turbulence Pr number is also much smaller than 0.9, which is widely assumed for engine simulations. In addition, the mean temperature profile at 50 ATDC was much lower than expected, and the instantaneous temperature variation was much larger than the experimental uncertainty. It seems a non-uniform cold turbulence structure existed around 50 ATDC. A similar phenomenon was found by other researchers in an HCCI engine [140].

To further study this phenomenon, additional experiments were done at 8.24 g/s intake mass flow rate. A slit was cut for the laser sheet, as shown in Figure 5.3. The effective compression ratio was reduced to 7.5. The rest of the experimental setup remained unchanged. The non-uniform cold turbulence structure was observed again at around 50 ATDC.

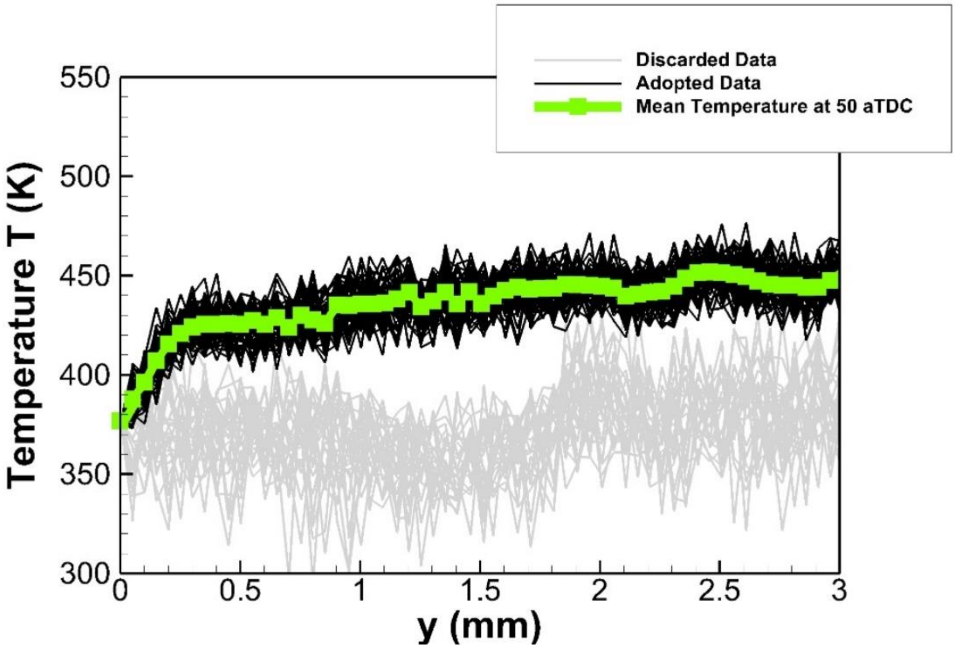

Figure 5.16: Instantaneous temperature profiles at 50 ATDC, with estimated $\overline{Re_s} = 516$

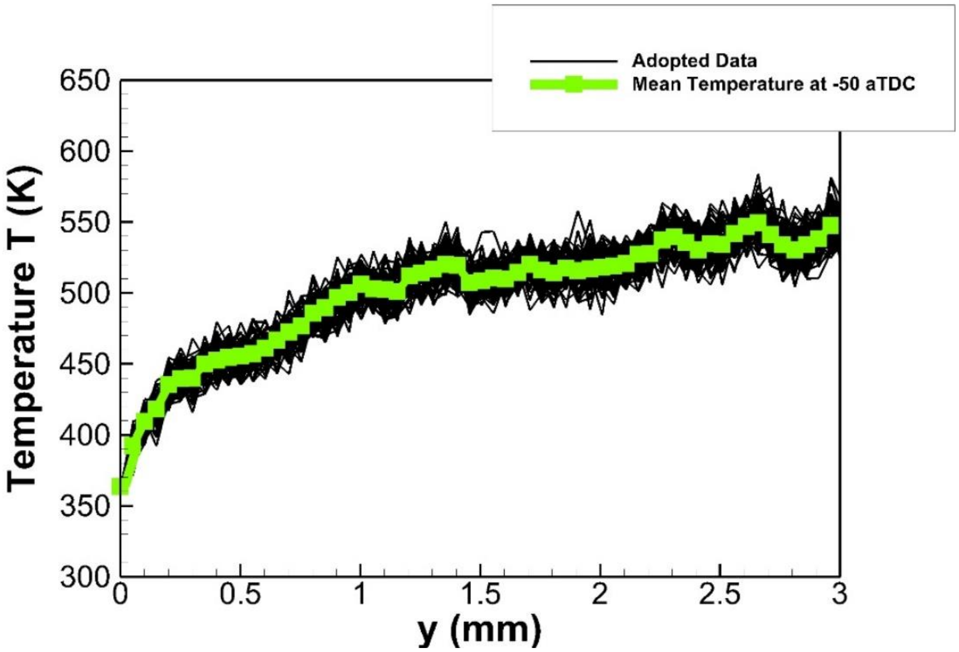

Figure 5.17: Instantaneous temperature profiles at 50 BTDC, with estimated $\overline{Re_s} = 516$

It seems instantaneous temperature profiles collapsed into two groups at 50 ATDC, and the high-temperature group had a narrower distribution than the low-temperature group, as shown in Figure 5.16. Comparing Figure 5.16 and Figure 5.17, a strong cycle-to-cycle variation existed at 50 ATDC, which caused a larger instantaneous temperature variation at 50 ATDC. It is important to point out that this cycle-to-cycle variation was a local event, and it had almost no effect on the cylinder pressure. Combined with the 3D engine CFD results (for details of the engine CFD, please refer to 0), we found that a cold gas "pocket" formed near the wall during the expansion stroke, as shown in Figure 5.18. This cold gas "pocket" moved around the cylinder wall and created local cycle-to-cycle variations. In addition, the measured instantaneous temperature variation was clearly larger than the experimental uncertainty within 50 ATDC to 70 ATDC because of the local cycle-to-cycle variation. However, within 50

ATDC to 70 ATDC, the turbulence temperature fluctuations were still small for most near walls region. The cold gas "pocket" itself had a higher level of turbulence temperature fluctuation. The divergent flow is believed to be the reason for the cold gas formation, but experimental proof is still needed.

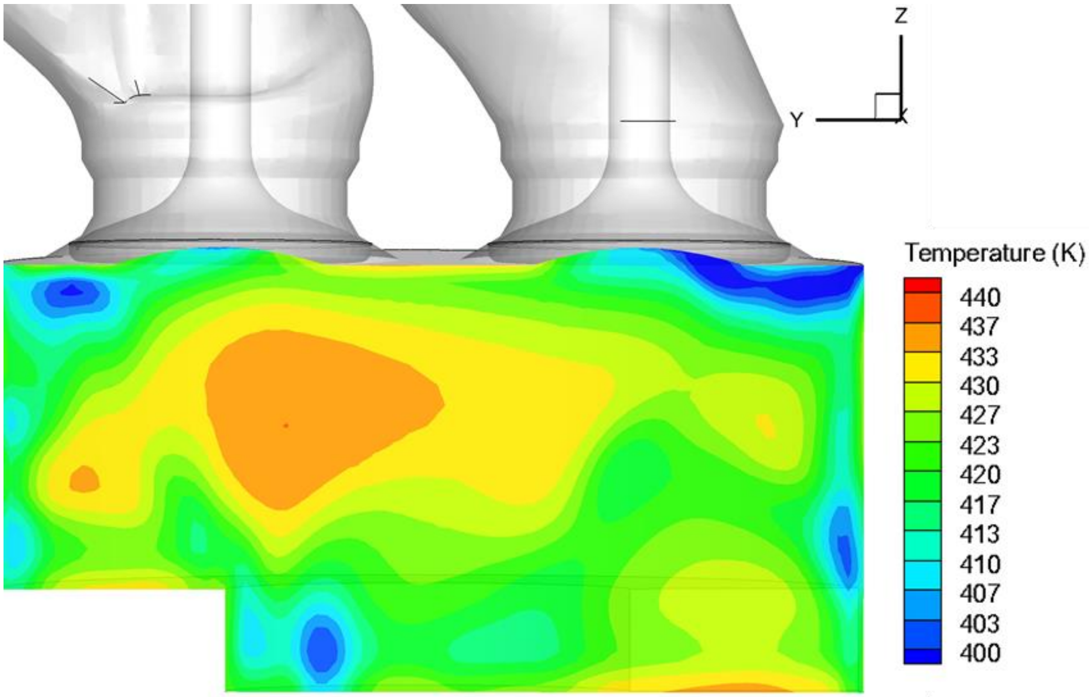

Figure 5.18: Full-size engine CFD simulation results. The non-uniform gas temperature exists during the expansion stroke.

As shown in Figure 5.16, the cold gas profile data was excluded for near wall temperature boundary layer studies because the cold gas "pocket" was a cycle-to-cycle event that had different turbulence flow conditions than the remaining engine boundary layer. 27 out of 100 cycles from 50 ACAD measurements and 4 out of 100 cycles from 70 ACAD measurements were discarded due to the effects of the low-temperature structure.

Figure 5.19 and Figure 5.20 show near-wall temperature profiles in the compression stroke and expansion stroke, respectively. The engine speed was 1200 rpm, and the intake mass flow rate was 8.24 g/s. The inlet gas temperature was 60 ºC (333 K). The estimated $\overline{\boldsymbol{Re_s}} = \mathbf{516}$ was higher than in previously experiments because of higher gas density. In addition, calibration curve 2 was used to calculate the temperature. As shown in Figure 5.7, calibration curve 2 was more temperature sensitive, so more precise temperature profile could be acquired.

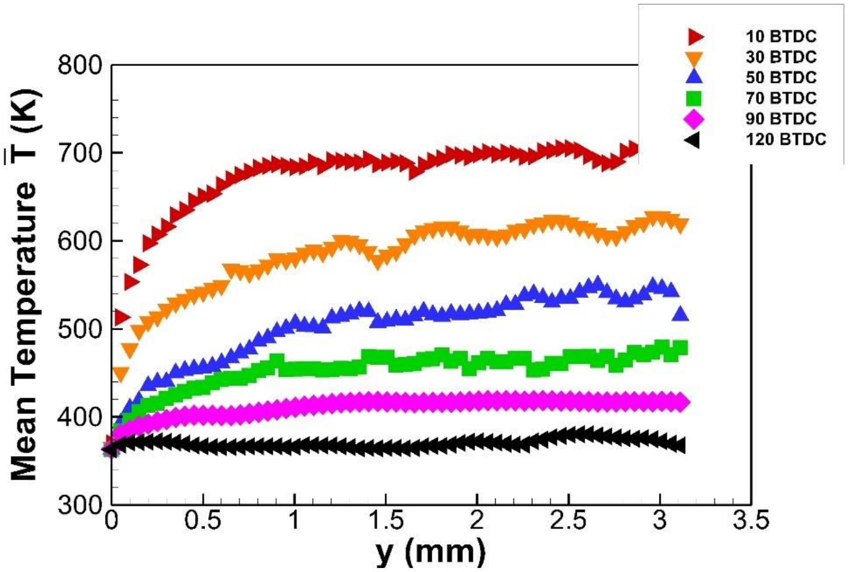

Figure 5.19: Near wall temperature measurements in the compression stroke, using calibration curve 2. The intake mass flow rate was 8.24 g/s, and estimated $\overline{\boldsymbol{Re_s}} = \mathbf{516}$.

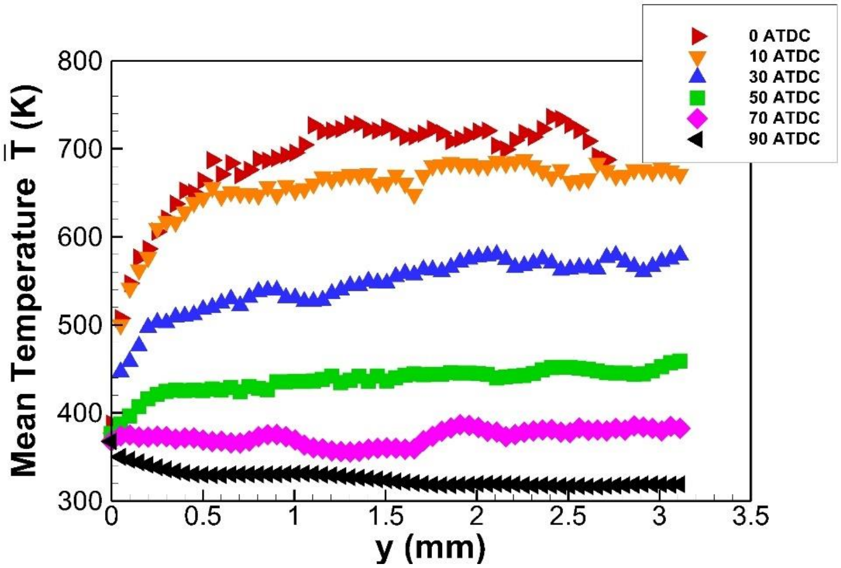

Figure 5.20: Near wall temperature measurements in the expansion stroke using calibration curve 2. The intake mass flow rate was 8.24 g/s, and estimated $\overline{Re_s} = 516$.

Similar to the previous experiment, the gas temperature next to the wall, $\lim_{y\to 0^+} \overline{T(y)}$, varied toward the wall surface temperature, but it did not reach the wall surface temperature, as shown in Figure 5.19 and Figure 5.20. The gas and solid behaviors are described by different governing equation. The PLIF technique can measure gas temperature infinitely close to the solid wall, but it can never reach the solid surface.

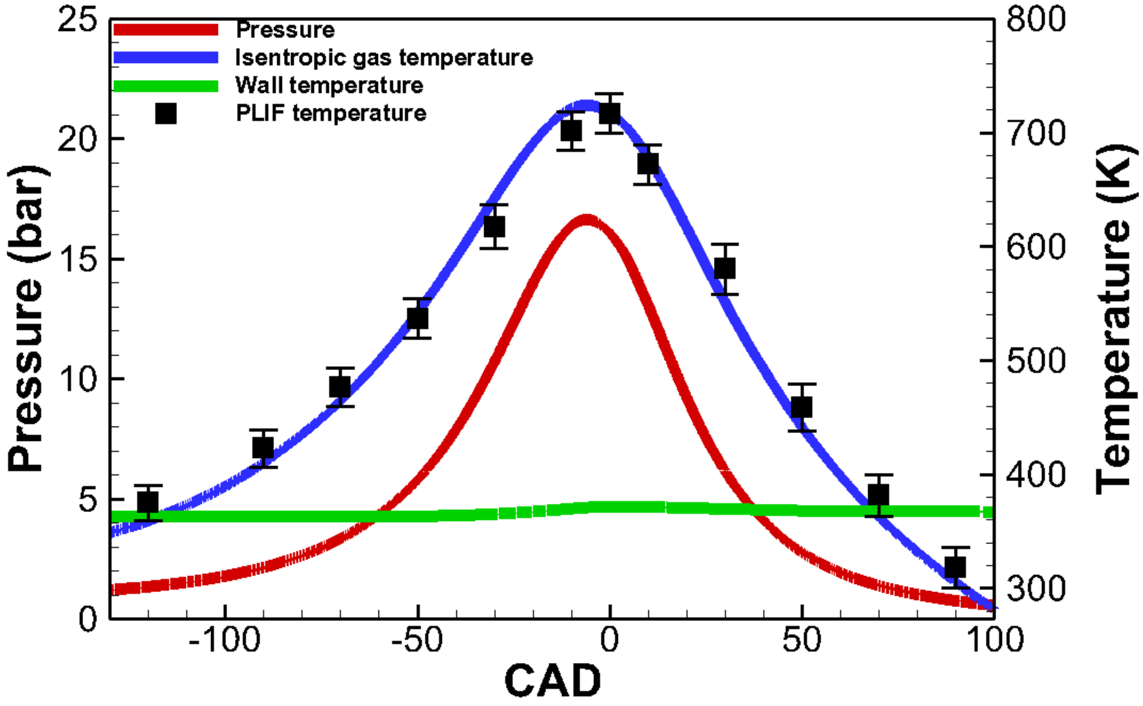

Figure 5.21: Average measured core gas temperature compared with pressure-based isentropic prediction.

Assuming isentropic processes, the core gas temperature was calculated from the measured in-cylinder pressure. In general, the isentropic prediction well matched the measurement, as shown in Figure 5.21. At most of the examined crank angles, the isentropic temperature was within experimental uncertainty, except 10 degree before TDC, where the maximum temperature difference was 31 K.

Usually, the boundary layer thickness, δ_T, is a distance in the wall normal direction from the wall to a point where the flow temperature has reached 99% of free stream temperature. However, the concept of free stream temperature and velocity do not always exist inside an engine cylinder, as shown in Figure 5.19 and Figure 5.20. As mentioned in Chapter 2, the flow inside the engine cylinder is very complex, and the fluid always experiences spatial temperature and pressure variations. It is hard to obtain the boundary layer thickness, δ_T , using traditional methods. Therefore, the thermal displacement thickness δ_T^* was used in this study. The thermal displacement was defined as:

$$\delta_T^* = \int_0^\infty \frac{T_\infty - T(y)}{T_\infty - T_w} dy$$

Equation 5.6

Where T_∞ and T_w is the average center gas temperature and wall surface temperature, respectively. In Equation 5.6, the spatial temperature variations were averaged out by integration, and the accuracy of the thickness was improved. In addition, the displacement thickness also had strong correlations to the outer layer and the weak layer thickness.

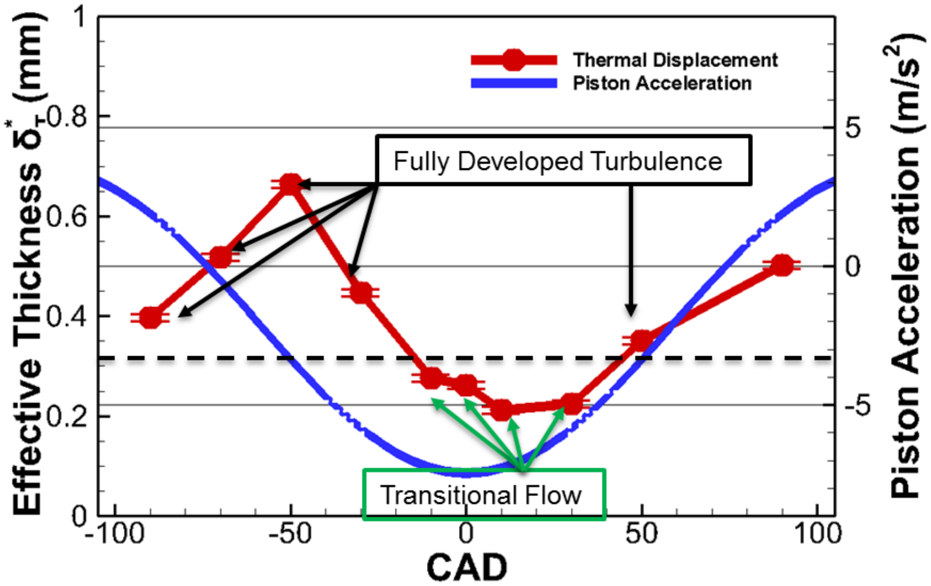

Figure 5.22: Thermal boundary layer displacement thickness

Figure 5.22 shows thermal displacement at each examined crank angle. It is clear that the thermal displacement periodically fluctuates with the engine crank angle. The thermal displacement reached a maximum out at the early piston deceleration phase. A maximum 25 degree phase difference existed between piston acceleration and thermal displacement fluctuation. This phase difference varied with spatial positions and charge density. It is important to know that the instantaneous Re ($\frac{U\delta}{v}$) number is directly proportional to the displacement thickness. Large thermal displacement also coincides with large Re number at the early piston deceleration phase. Therefore, this supports the intermittently turbulent theory that the fully developed boundary layer starts to appear at early decelerating phases. In addition, because of compression effects, the fully developed boundary layer would start to appear in the a later compression stroke in a “motored” IC engine. There is a possibility that the combustion event increases instantaneous Re, but how the combustion event affects turbulence heat flux is still unknown.

To further study the temperature boundary layer, a scaling law was applied to the temperature profile, as shown in Figure 5.23. For fully developed temperature boundary layer, previous studies found that the normalized temperature profiles collapse to a universal profile at different Re numbers in the pipe flow [41]. This phenomenon conforms to the Log-Law, where the nominalized temperature profile is independent of the local Re number. Figure 5.23 shows very interesting results within the “log-region,” $\frac{y}{\delta_T} < 0.3$:

- For the -90 ACAD to -10 ACAD period, the normalized temperature profiles were mostly on top of each other and formed a universal profile independent of the local Re number. It is safe to conclude that the temperature profiles were fully developed within this range of CAD
- For the -10 ACAD to 10 ACAD period, the normalized temperature profiles started to depart from the universal profile at -10 CAD. Then, the normalized temperature profiles varied with thermal displacement. The difference between the normalized temperature profiles and the universal profile increased as the thermal displacement decreased. At 10 CAD, the thermal displacement was shortest within the examined crank angle, and the normalized temperature profile was also farthest away from the universal profile, as shown in Figure 5.23.
- For 10 ACAD to 50 ACAD, the nominalized temperature profiles varied toward the universal profile, as thermal displacement increased. At 50 ACAD, the normalized temperature again matched that of the universal profile.

As mentioned previously, the instantaneous Re ($\frac{U\delta}{v}$) number is directly proportional to the displacement thickness. Therefore, for the -10 CAD to 30 CAD period, the instantaneous Re number was about half of the remaining examined CAD, and the normalized temperature profile varied with the instantaneous Re number. It is fair to say that the temperature boundary layer was at transitional flow around the -10 CAD to 30 CAD period.

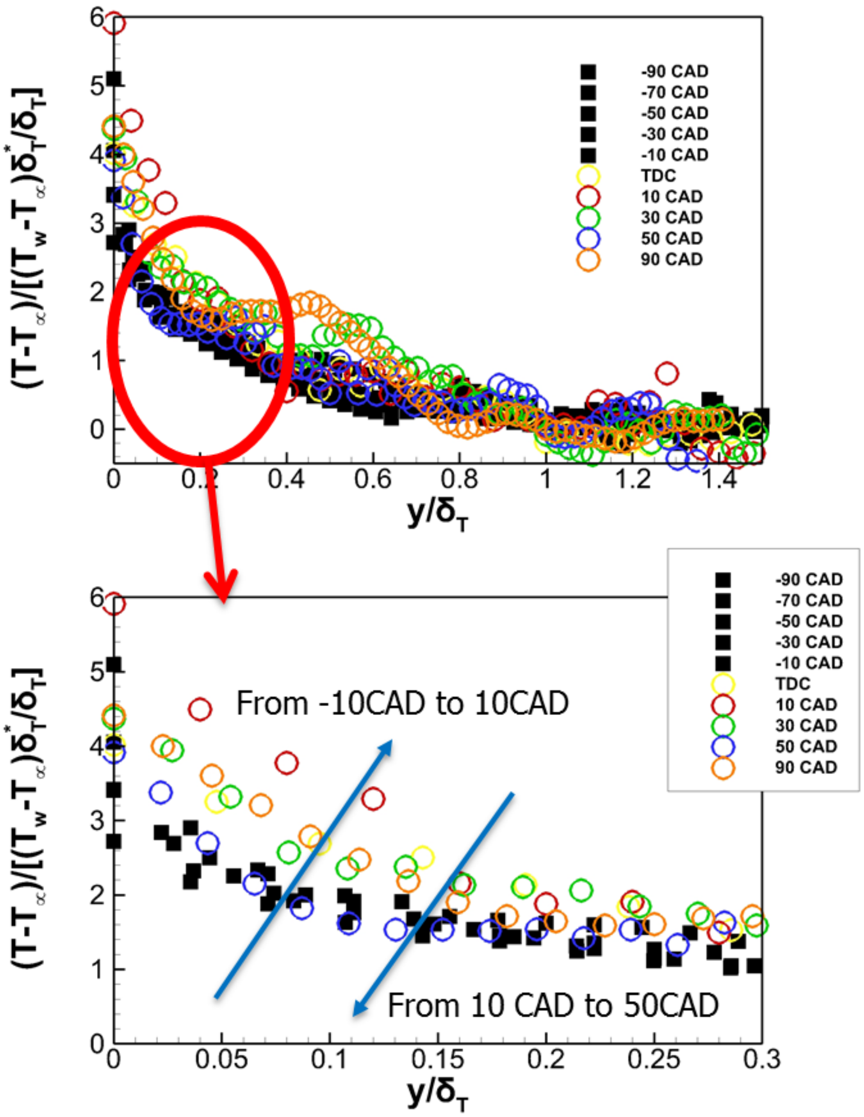

Figure 5.23: Nominalized near wall temperature profile.

The wall temperature was relatively constant, as shown in Figure 5.21. The maximum wall temperature variation was about 9 K. Even considering combustion, the average wall temperature variation was expected to be less than 30 K [141]. The conduction rate through a solid is much higher than for a gas, and the solid wall is able to transfer gas-to-wall energy away almost immediately. This is the reason that many modelers assume a constant surface temperature for engine simulations [119, 120]. However, this is only half of the story. The assumption that wall temperature is constant implies, which means the rate of temperature variation is zero, $\frac{dT_w}{dt} = 0$. From IR temperature measurements, it is clear that $\frac{dT_w}{dt} = 0$ was not always valid, and the maximum rate of temperature change was about 2000 K/s at -15 ATDC as shown in Figure 5.24. The rate of temperature variation was approximately zero for most of the engine cycle, except between the angles -50 ATDC to TDC. -50 ATDC to TDC was a period in which the in-cylinder gas had the highest density, and temperature difference was also the largest. Therefore, the gas-to-wall convocation increased rapidly, and the gas-to-wall heat convection was much larger than the solid heat conduction within the -50 ATDC to TDC period. In addition, as described previously, the thermal boundary layer was fully developed around -50 ATDC, and the fully developed boundary layer had a much larger heat convocation coefficient than the laminar or transitional boundary layer. It is also interesting that the rate of temperature variation dropped around -15 ATDC, where the boundary layer can be characterized as to transitional flow. Most engine modelers assume constant wall temperature $(T_w = canstant\ and\ \frac{dT_w}{dt} = 0)$ or quasi-steady $(\rho_{solid} c_p \frac{dT_w}{dt} \ll k_{solid} \frac{d^2T}{dx^2})$ [26, 119]. Indeed, it is a fairly accurate prediction for most engine cycles, except -50 ATDC to TDC. The constant wall temperature or quasi-steady assumptions would under predict gas-to-wall heat flux $q"_w$ at around the -50 ATDC to TDC period because of positive $\frac{dT_w}{dt}$.

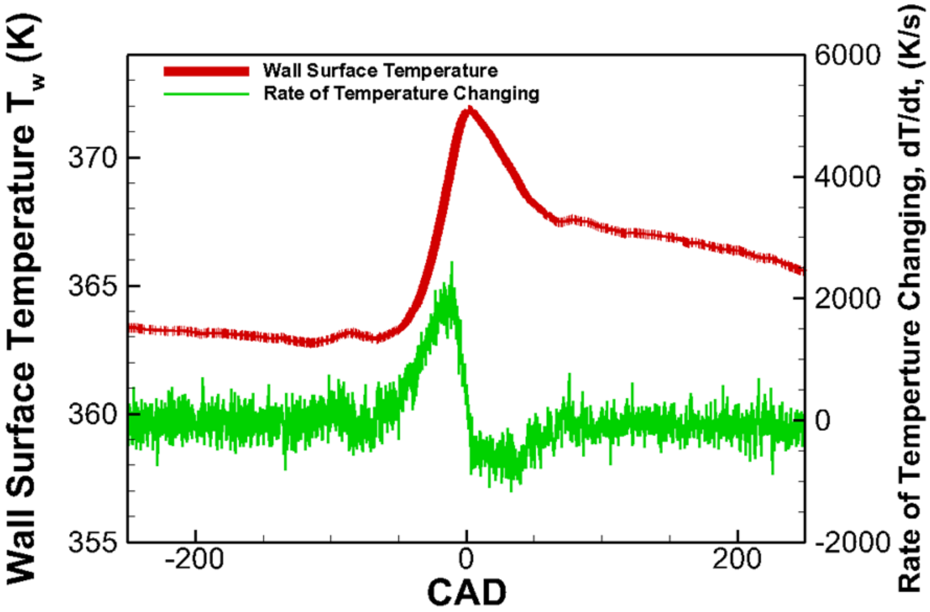

Figure 5.24: Wall surface temperature and rate of temperature variation in a "motoring" engine

The PLIF measurements show that the temperature boundary layers were fully developed within the -90 ACAD to -10 ACAD period, and the temperature boundary layers were transitional regime within the -10 ACAD to 30 ACAD period, as shown in Figure 5.22. The temperature boundary layers became fully developed around 50 ACAD. The -120 ACAD and 70 ACAD were two special cases. The difference between the averaged core gas temperature and the wall surface temperature was almost zero at -120 ACAD and 70 ACAD, as shown in Figure 5.21. The temperature boundary layer was nonexistent at -120 ACAD and 70 ACAD. The PLIF results fit the description of the intermittently turbulent cycle, where the fully developed boundary layer started to appear at the early decelerating phases of the cycle, and the rest of the cycle remained at transitional flow. The average $\overline{Re_s} = 516$ also fits to $\sim 500 < \overline{Re_s} < 3460$ intermittently turbulent range although for an IC engine, the lower limits of average $\overline{Re_s}$ should be much less than 500 when? intermittently turbulent. Because of compression effects, the instantaneous Re_s number, during compression, is much higher than the cycle average $\overline{Re_s}$. For the same reason, the lower limits of engine average $\overline{Re_s}$, for an intermittently turbulent cycle, probability relates to engine compression ratio. Although the detail is still unknown, a bypass mechanism may exist in large compression ratio engines. In addition, the upper limits of average $\overline{Re_s}$, for intermittently turbulent range, remains unchanged because no compression was affected at the bottom dead center (BDC). This means that for most vehicle engine operation conditions, a mix of fully developed and transitional boundary layer conditions exist inside an engine cylinder. The log-law only is not enough to predict the gas-to-wall heat transfer for the entire engine cycle.

The heat transfer cannot resolve without velocity. An in-cylinder micro-PIV was conducted to study velocity profile at the same location and condition as the PILF measurements.

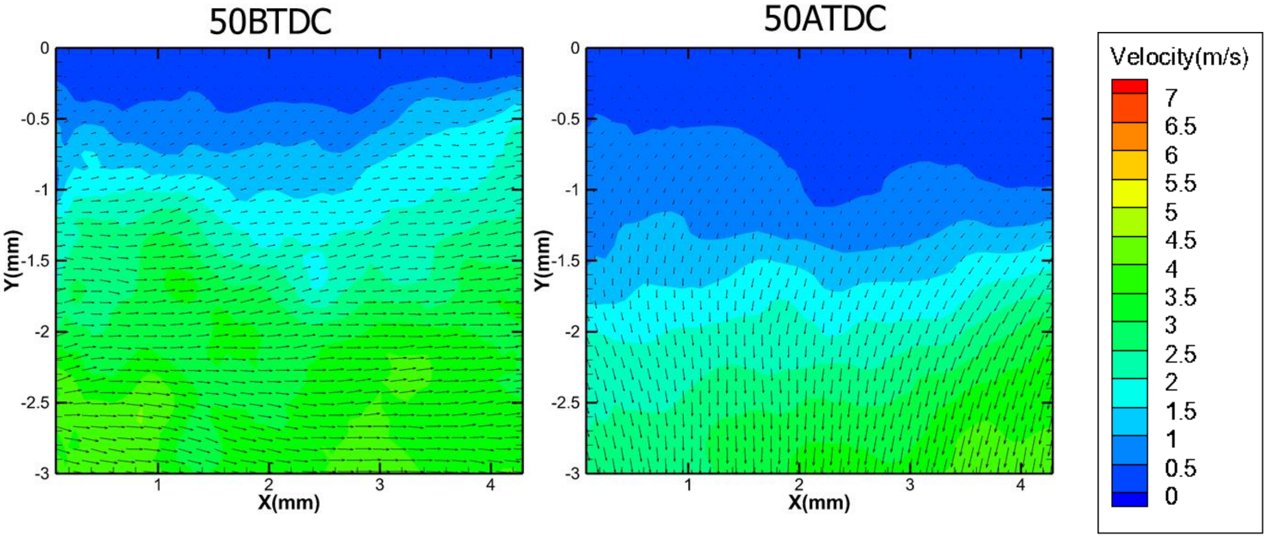

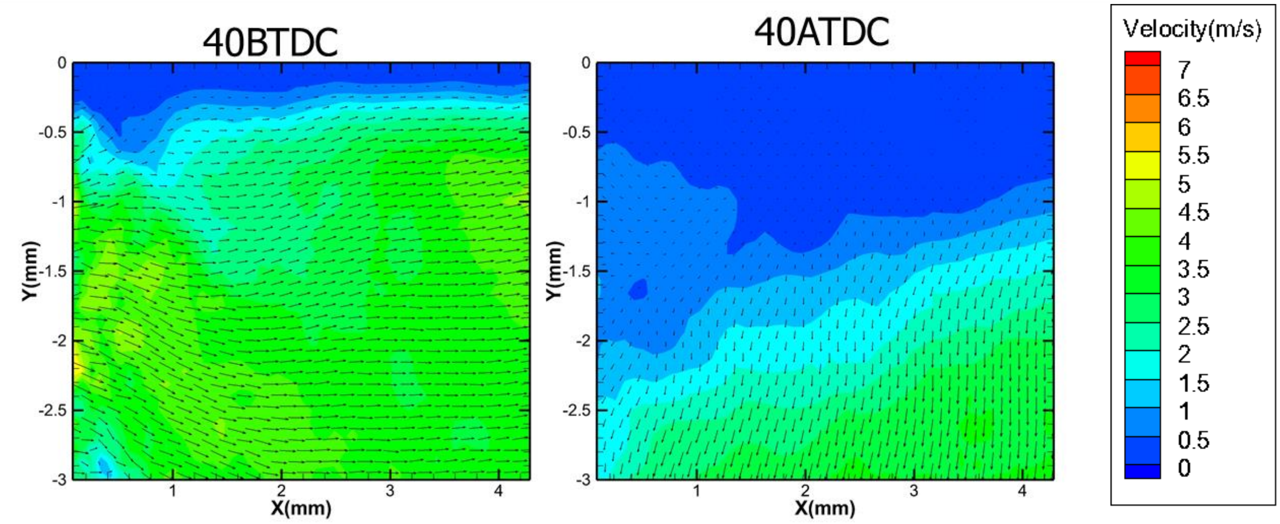
40BTDC
40ATDC
Y(mm)
X(mm)
0
-0.5
-1
-1.5
-2
-2.5
-3
1
2
3
4
Velocity(m/s)
7
6.5
6
5.5
5
4.5
4
3.5
3
2.5
2
1.5
1
0.5
0

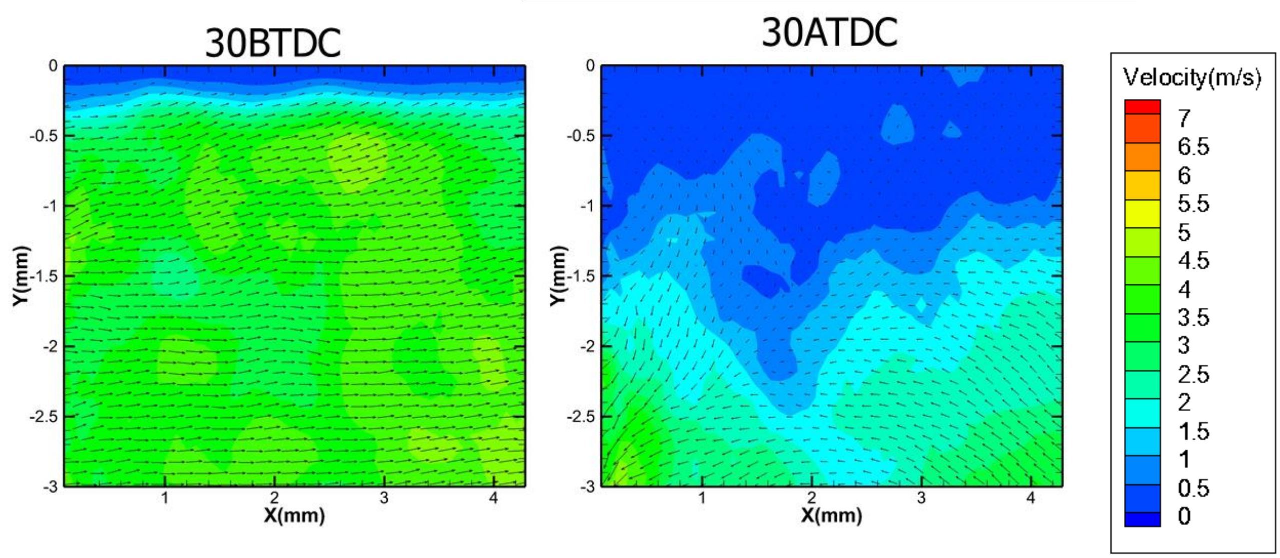
30BTDC
30ATDC
Y(mm)
X(mm)
0
-0.5
-1
-1.5
-2
-2.5
-3
1
2
3
4
Velocity(m/s)
7
6.5
6
5.5
5
4.5
4
3.5
3
2.5
2
1.5
1
0.5
0

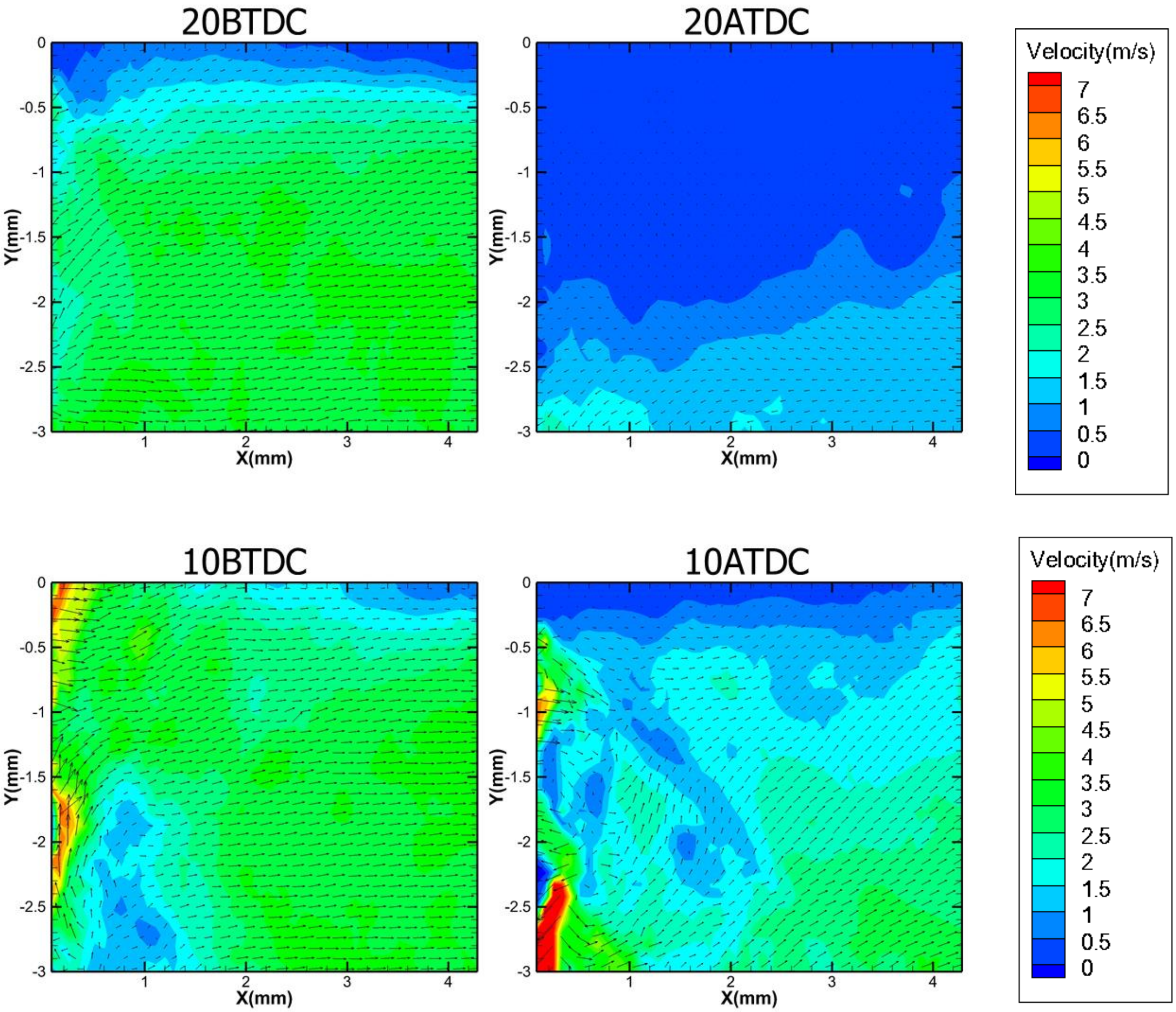
20BTDC
20ATDC
10BTDC
10ATDC
Y(mm)
X(mm)
0
-0.5
-1
-1.5
-2
-2.5
-3
1
2
3
4
Velocity(m/s)
7
6.5
6
5.5
5
4.5
4
3.5
3
2.5
2
1.5
1
0.5
0

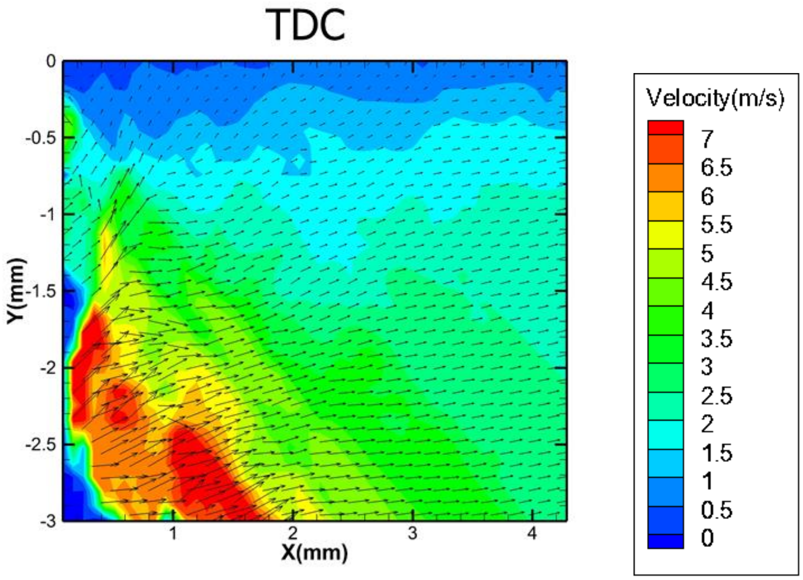

Figure 5.25: PIV measurement at estimated $\overline{Re_s} = 516$. x- direction is parallel to the wall, and y-direction is vertical to the wall.

Figure 5.25 shows the average PIV measurement around -50 CAD to 50 CAD. From the results, the velocity boundary layer decreased within the -50 CAD to -10 CAD period. This is consistent with temperature measurements. Around -10 CAD to 10 CAD, it seems that a high-velocity flow appeared near the edge of the observation window. This probably was an artificial flow. Part of the diesel droplet which was used as a seed particle evaporated around TDC and reduced particle concentration. The poor particle concentration increased the chance of false image correlation, which created the artificial flow near the edge of the observation window. The major components of velocity direction also varied. Although the velocity in the z-direction (z-direction is perpendicular to the observation window) is unknown. for the -50 CAD to -10 CAD period, the major component of the velocity was in the x-direction, and the velocity in they-direction had negligible magnitude. For the -10 CAD to 10 CAD period, velocity in both the x-direction and the y-direction had about the same level magnitude. At 20 CAD, the magnitude of the velocity was practically zero, and the velocity boundary layer was also practically non-existent within the observation window. For the 30 CAD to 50 CAD period, the major component of the velocity was in the y-direction, and the velocity in the x-direction had negligible magnitude. The velocity boundary layer was gradually reformed, and a stable velocity boundary layer was observed at 50 CAD. The PIV results support the PLIF results and the intermittent turbulent theory, where a transitional boundary layer existed within the -10 CAD to 30 CAD period, and a boundary layer was resumed to fully develop around 50 CAD.

To further study the effects of the transitional boundary layer on heat transfer prediction, the law of the wall was applied. Assuming the fire deck was a smooth surface, $\beta = 2.513$ was used for the thermodynamical log-law as shown in Equation 2.33 [120]. Nitrogen has physical properties very similar to air, so the turbulence Prandtl number,Pr_t was 0.9. The experimental gas temperature measurements, at 0.5mm distance from the wall, were used as the first cell temperature, and the first near wall grid size was assumed to be 1mm. The purpose of this study was not to resolve the near wall temperature profile but rather to predict the gas-to-wall heat flux without resolving the full temperature profile. Therefore, using experimental temperature measurements eliminated all possible errors from the turbulence model, except for the law of the wall. Based on the law of the wall (Equation 2.18 and Equation 2.33), The gas-to-wall heat flux can be calculated by the following equations:

$$q_w'' = \begin{cases} \dfrac{u_\tau \rho c_p (T_g - T_w)}{Pr_m y^+} & y^+ < 11.05 \\ \dfrac{u_\tau \rho c_p (T_g - T_w)}{2.14 \ln(y^+) + 2.513} & y^+ > 11.05 \end{cases}$$

Equation 5.7

Where T_g is the gas temperature, and T_w is the wall temperature. Pr_m is the molecular Pr number. Equation 5.7 is the standard law of the wall. Some variations of the law of the wall have been developed by other researchers [26, 76, 119], and the standard law of the wall was used for abase line comparison. In addition to the law of the wall, the non-dimensional Woschni correlation, Equation 2.5, was also used as reference.

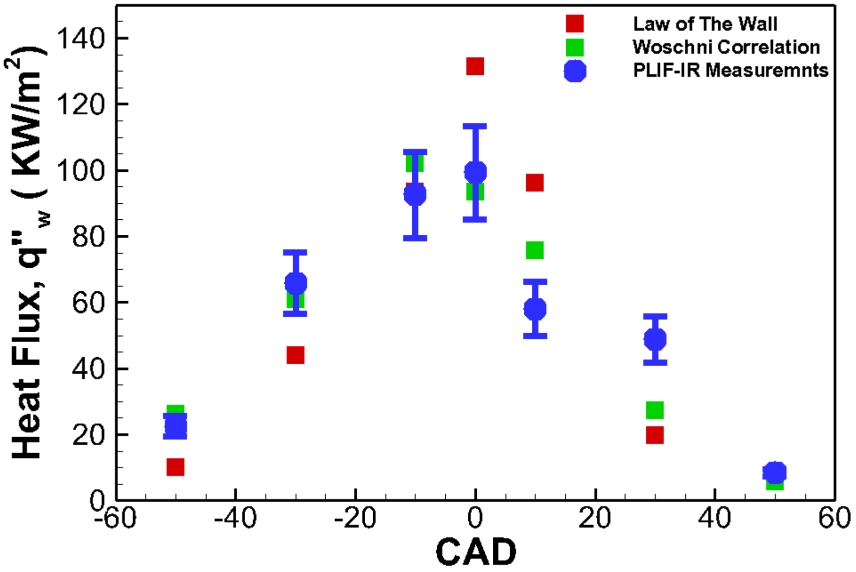

Figure 5.26: Law of the wall heat flux prediction from y=0.5 mm. Non-dimensional Woschni correlation heat flux prediction was used as a reference.

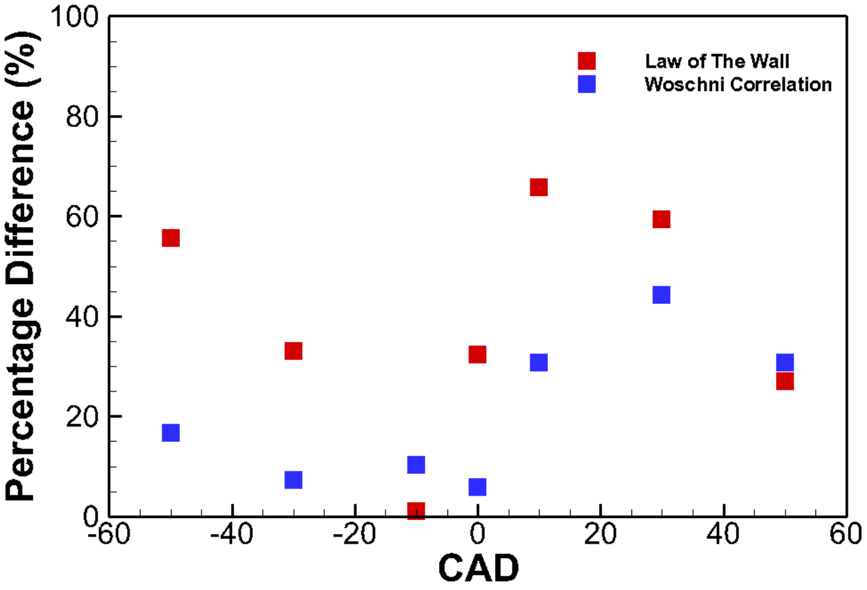

Figure 5.27: The percentage difference between the model prediction and experimental measurements

Figure 5.26 shows a comparison between heat flux predictions and experimental measurements. The experimental gas-to-wall measurements were calculated by definition, $q_w^{"} \equiv -k_g \frac{dT}{dy}\Big|_{y=0}$. Where k_g is the gas heat conductance at wall temperature. The slope $\frac{dT}{dy}\Big|_{y=0}$ was calculated by the best linear fit PLIF gas temperature and the IR wall surface temperature. A MATLAB code was used to find the best window for a linear fit, and minimal 3 points were used for the linear fit. First of all, the Woschni correlation had surprisingly good agreement with the experimental measurements. Especially during the compression stroke, the predictions from the Woschni correlation were within the estimated experimental uncertainty. The law of the wall under predicted the heat flux during the compression stroke. This is mostly due to the compression effects, which were resolved in Han and Reitz's wall model [120]. The law of the wall over predicted more than 70% of heat flux near TDC. This is due to transitional flow. The law of the wall assumed a fully developed boundary layer, but the local boundary layer was at transitional flow around the -10 CAD to 30 CAD period. The transitional flow had less convection heat transfer compared to the fully developed turbulence flow. Therefore, the law of the wall over predicted the heat flux near TDC because of the transitional flow effects. The compression effects and transitional flow effects cancel out each other at -10 CAD, where the law of the wall prediction was right on top of the experimental measurement. Figure 5.27 shows the percentage of difference between model predictions and experimental measurements. It was really surprising that the non-dimensional Woschni correlation had an overall better prediction than stand law of the wall. Although, the Woschni correlation had less than 50% percentage of difference. It is still a pressure-based correlation, and the Woschni correlation did not capture the sudden decrease in the heat flux around 10 CAD to 20 CAD. Both the Woschni correlation and the law of the wall prediction had their max percentage of difference around the 10 CAD to 20 CAD period, where the in-cylinder flow direction changed. The standard law of the wall had a maximum 64% percentage of difference with the observation window.

CHAPTER 6 : MULTI ZONE HEAT TRANSFER MODEL

6.1 Introduction

IC engine simulation is one of the most expensive in terms of computation cost. The complexity of reciprocating engine in-cylinder flow outclasses jet flow and flow over an aircraft [142]. Therefore, cost effectiveness always is an important factor for engine engineers. a number of cells, $N \propto {Re_L}^{1.8}\ to\ {Re_L}^{2.4}$, are required to correct resolve the "inner" boundary layer [143, 144]. For comparison, a number of cells, $N \propto {Re_L}^{3}\ to\ {Re_L}^{3.2}$, are required for DNS [142]. The computation cost for fully resolving the boundary profile is approaching the DNS level. Only DNS and LES-NWR (large-eddy simulation with near wall resolution) have the resolution to resolve the near wall region. Therefore, predicting in-cylinder gas-to-wall heat transfer by resolving the full boundary layer profile has limited practical applications. Other LES models and RANS models lack the resolution even though some of them may have the capability to resolve the near wall region. The wall-functions are the primary solution for predicting in-cylinder gas-to-wall heat transfer, before future "super" computer offers more suitable computation resource for engine DNS or LES-NWR.

The Law of the wall is used as the boundary conditions to solve the system of equations, which contain the continuity equation (Equation 2.43), the momentum equation (Equation 2.44) and the energy equation (Equation 2.45). Usually, the law of the wall has the following assumption:

- Zero or negligible temperature/pressure gradients in the wall parallel direction.

- Viscous dissipation, and the Dufour and enthalpy diffusion effects on energy flux are neglected
- For near wall region, the flow is parallel to the wall.
- Density and other molecular properties are constant within the first grid.
- There is a fully developed boundary layer.
- There are no source terms (non-reaction flow, or work done by pressure).
- Incompressible flow

In the early 1990s, the Reynolds-analogy assumption was also widely used in 3D simulations [145]. The Reynolds-analogy assumption allows for resolving gas temperature and heat transfer without solving the actual energy equation, reducing computation cost for early computers. Today, the Reynolds-analogy assumption has been found to be invalid in engine flow because of nonhomogeneous turbulence, unsteadiness (periodical flow), and chemical heat release [75, 100, 146]. Therefore, the standard Reynolds-analogy is less frequently used in engine simulations. Instead, the constant turbulent Prandtl number, $Pr_t = 0.9$, is assumed for solving the energy equation. In addition, zero or negligible temperature/pressure difference can be achieved by using an adaptive mesh. Engine flow velocity is about 10 m/s magnitude, which is far below the speed of sound, so viscous heating can be neglected. Previously, incompressible flow assumption was considered as a major source of error for in-cylinder gas-to-wall heat prediction [119]. The standard law of the wall under predicted the heat flux in an engine cylinder because of the compression effect [120]. This under prediction can also been found in the PLIF-IR results presented in Chapter 5. The wall function for compressible flow was developed by the Han and Reitz model [120]. However, the difference of heat flux still exists between prediction and experimental measurements [37] after including the compression effect. Radiation heat transfer was a possible candidate for the error source. However, recent studies have shown that only 1% of the total heat transfer is due to radiation heat transfer [11], and it is unlikely that the radiation heat transfer would make up the difference between the wall function prediction and experimental measurements.

From previous PLIF-IR and PIV results (discussed in Chapter 5), the near wall mean temperature profiles and the mean velocity profiles have supported the existence of the transitional boundary layer in an IC engine. In addition, based on cycle averaged Stokes' Reynolds number ($\overline{Re_s}$) analysis, the engine flow motion fits the description of being intermittently turbulent, which is very different from the fully developed turbulent assumption. The traditional log region does not actually exist in the transitional boundary layer [131]. The log-law does not apply to the transitional boundary layer. In addition, the turbulent Prandtl number, Pr_t, varies greatly for reciprocating flow [133]. The exact profile of the near wall turbulent Prandtl number in engine cylinder is not clear. Based on channel flow DNS results, for intermittently turbulence, the turbulent Prandtl number, Pr_t, substantially decreases toward the boundary layer edge [147], and the Re_s number seems to have little effect on the turbulent Prandtl number profile. It can be assumed that the engine flow motion has some similarity to the reciprocating channel flow. The variation in the turbulent Prandtl number, Pr_t, could easily contribute more than 50% of the difference for heat flux prediction. Also, it is important to remember that a full developed boundary exists in the engine cylinder, where the log-law is valid. Therefore, a robust wall model is needed for engine heat transfer prediction. Significant research has been put into the near wall turbulence model [148, 149], but little attention has been given to wall functions. This paper proposed a multi-zone method to improve wall functions. In addition, to further study the in-cylinder gas-to-wall heat transfer, full-sized 3D engine simulations were conducted to study in-cylinder turbulent parameters.

6.2 Theory

According to the first law of thermodynamics, the general energy conservation equation inside an wall adjacent cell, can be written as

$$\frac{\partial q"}{\partial y} = -\rho c_p \frac{\partial T}{\partial t} + \delta W_p - \delta Q_c$$

Equation 6.1

Where total heat flux, $q"$, is

$$q" = -k_g \frac{\partial T}{\partial y} + \rho c_p \overline{T'v'}$$

Equation 6.2

According to the turbulent thermal diffusivity hypotheses, the Reynolds heat flux, $\overline{T'v'}$, is assumed to be tested to the turbulence diffusivity, α_t, through:

$$-\overline{T'v'} = \alpha_t \frac{\partial T}{\partial y} = \frac{v_t}{Pr_t} \frac{\partial T}{\partial y}$$

Equation 6.3

So, Equation 6.2 becomes

$$q" = -(\frac{\rho c_p v}{Pr_m} + \frac{\rho c_p v_t}{Pr_t})\frac{\partial T}{\partial y}$$

Equation 6.4

In Equation 6.1, the first term of the right-hand side, $-\rho c_p \frac{\partial T}{\partial t}$, is the transient term, which represents the rate of energy changes in a controlled volume. The second and third terms of the right-hand side are work done by the pressure (W_p) and the heat released/absorbed by chemical reactions (Q_c), respectively. The work done by pressure and heat released/absorbed by chemical reactions has been ignored by previous modelers to simplify Equation 6.1 for calculations [37, 119]. For this study, the heat released/absorbed by chemical reactions was zero because of non-reaction flow condition (no fuel and pure nitrogen), but the effect of the work done by pressure were studied for compression and expansion. It is obvious that engine heat transfer is unsteady, as described by Equation 6.1. However, a quasi-steady assumption had its useful for solving engine problems. In Chapter 5, the IR results shows $\left.\frac{\partial T}{\partial t}\right|_{y=0} \approx 0$ is valid for almost the entire engine cycle, except the -50 ATDC to TDC period. Therefore, the rate of energy change, $-\rho c_p \frac{\partial T}{\partial t}$, is negligible at the wall. The effects of the $\left.\frac{\partial T}{\partial t}\right|_{y=0}$ variation, within the -50 ATDC to TDC period, will be discussed later.

Integrate Equation 6.1 and substitute for Equation 6.4,

$$-\rho c_p \left(\frac{v}{Pr_m} + \frac{v_t}{Pr_t}\right)\frac{\partial T}{\partial y} = q_w^{"} - \overline{W_p}"y + \overline{Q_c}"y$$

Equation 6.5

For compression and expansion, it is safe to assume that there is uniform pressure inside the engine cylinder during compression and expansion (ZPG flow assumption). The average work done by pressure, $\overline{W_p}$, can be calculated by the specific heat release rate equation [92].

$$\overline{W_p"} = (\frac{\gamma}{\gamma-1}p\frac{dV}{dt} + \frac{1}{\gamma-1}V\frac{dp}{dt} - \frac{pV}{(\gamma-1)^2}\frac{d\gamma}{dt})/V$$

Equation 6.6

Where γ is the specific heat ratio. For conductive sublayer (conductive sublayer is thinner than the viscous sublayer for air), $\frac{v}{Pr_m} \gg \frac{v_t}{Pr_t}$. Therefore, the effect of the turbulent heat flux is negligible. Integrate Equation 6.5 again:

$$q_w^" = \frac{k_g}{y}\theta + \frac{y}{2\rho c_p}\overline{W_p"} - \frac{y}{2\rho c_p}\overline{Q_c"}$$

Equation 6.7

Rewrite Equation 6.7 in wall units:

$$q_w^" = \frac{u_\tau \rho c_p \theta}{Pr_m y^+} + \frac{y^+ v}{2\rho c_p u_\tau}\overline{W_p"} - \frac{y^+ v}{2\rho c_p u_\tau}\overline{Q_c"}$$

Equation 6.8

It is clear to see that the effects of both the work done by both the pressure and chemical heat release are negligible when y^+ is small. The difference between Equation 6.8 and the traditional linear equation (Equation 2.18) is negligible. However, as y^+ increases to log-region, things are different. Let $v^+ = \frac{v_t}{v}; y^+ = \frac{u_\tau y}{v}$; $W_p{}^+ = \frac{\overline{W_p"}v}{q_w^" u_\tau}$, $Q_c{}^+ = \frac{\overline{Q_c"}v}{q_w^" u_\tau}$. Equation 6.5 becomes

$$-\int \frac{u_\tau \rho c_p}{q_w^{"}} dT = \int \frac{1}{\left(\frac{1}{Pr_m} + \frac{v^+}{Pr_t}\right)} dy^+ - \int \frac{{W_p}^+ y^+}{(\frac{1}{Pr_m} + \frac{v^+}{Pr_t})} dy^+ + \int \frac{{Q_c}^+ y^+}{(\frac{1}{Pr_m} + \frac{v^+}{Pr_t})} dy^+$$

Equation 6.9

The solution of this equation was found based on consultation from the previous study of the Han and Reitz model, and the following expression is used for $\frac{v^+}{Pr_t}$ [120]:

$$\begin{cases} \frac{v^+}{Pr_t} = C_a + C_b y^+ + C_c {y^+}^2 & y^+ \leq 40 \\ \frac{v^+}{Pr_t} = C_m y^+ & y^+ > 40 \end{cases}$$

Where the model coefficient $C_a = -0.15, C_b = 0.025, C_c = 0.012, and\ C_m = 0.48$ is used. Therefore, the log-region temperature profile equation can be written as

$$\frac{u_\tau \rho c_p T_g \ln\left(\frac{T_g}{T_w}\right)}{q_w^{"}} = 2.14 \ln(y^+) + 3.26 y^+ \left({W_p}^+ - {Q_c}^+\right) - 67.35\left({W_p}^+ - {Q_c}^+\right) + 3.7$$

Equation 6.10

Solve for $q_w^{"}$

$$q_w^{"} = \frac{u_\tau \rho c_p T_g \ln\left(\frac{T_g}{T_w}\right) - 3.26 y^+ \left(\overline{W_p"} - \overline{Q_c"}\right) \frac{v}{u_\tau} + 67.35\left(\overline{W_p"} - \overline{Q_c"}\right) \frac{v}{u_\tau}}{2.14 \ln(y^+) + 3.7}$$

Equation 6.11

In this study, $\overline{Q_c"} = 0$. The effect of $\overline{W_p"}$ will be discussed in the results section. It is important to point out that $y^+ > 40$ is a hidden assumption for Equation 6.11.

Speaking of wall units, the usual two-zone wall function used $y^+ < 11$ for the linear equation and $y^+ > 11$ for the log- region. Although most of the time, it may not affect the heat flux predictions, the physical phenomenon is really not captured for heat transfer.

The originally around $y^+ \approx 11$ is the velocity linear equation and the velocity log equation crossing point, so mathematically it seems to work. The problems are: $y^+ \approx 11$ is not the crossing point of the temperature equations, and the temperature linear sublayer is about 30% thinner than the velocity boundary linear sublayer. For temperature profiles, $y^+ \approx 7.7$ is the crossing point. It is a small problem, but one that should be fixed. The instantaneous Re number varies a lot in an engine cycle, and the value of y^+ also substantially varies with constant grid size. The changes of mistaken equations are not small in practical applications. In addition, the turbulence boundary sublayer varies for periodical flow [131, 133], such as the flow motions in engine cylinder. Using wall-unit-based thickness is not enough to describe the physical phenomenon. It is more reasonable to use the ratio between turbulent thermal diffusivity and molecular thermal diffusivity, $\frac{\alpha_t}{\alpha_m}$.

- For $y^+ < 8$, the linear sublayer layer, work done by pressure and chemical heat release are negligible because of ${y^+}^2$ factor. $q_w^{"} = \frac{u_\tau \rho c_p (T_g - T_w)}{Pr_m y^+}$
- For $y^+ > 8\ and\ \frac{\alpha_t}{\alpha_m} < 0.2$, it is possible that turbulent heat flux is still negligible when y^+ is outside the traditional linear sublayer range because of the transitional boundary layer effects. As y^+ increases, the effects of the work done by pressure and chemical heat release increases. $q_w^{"} = \frac{u_\tau \rho c_p \theta}{Pr_m y^+} + \frac{y^+ v}{2\rho c_p u_\tau} \overline{W_p"} - \frac{y^+ v}{2\rho c_p u_\tau} \overline{Q_c"}$

- For $y^+ > 8\, and\; 0.2 < \frac{\alpha_t}{\alpha_m} < 5$, the turbulent heat flux and conduction heat transfer are at about the same magnitude. Currently, no wall function can predict the accurate heat flux without fully resolving the boundary layer profile.
- For $y^+ > 8\, and\; \frac{\alpha_t}{\alpha_m} > 5$, conduction heat transfer is negligible. The Log-law reasonably predicts heat flux. This study proposed a log-law variation for IC engines only, which includes the effects of work done on pressure, $\overline{W_p"}$. Heat transfer during combustion still relies on further studies. $q_w^{"} = \frac{u_\tau \rho c_p T_g\, ln\left(\frac{T_g}{T_W}\right) - 3.26 y^+ \left(\overline{W_p"} - \overline{Q_c"}\right)\frac{v}{u_\tau} + 67.35\left(\overline{W_p"} - \overline{Q_c"}\right)\frac{v}{u_\tau}}{2.14\, ln(y^+) + 3.7}$, and $\overline{W_p"}$ is given in Equation 6.6 for compression and expansion, and $\overline{W_p"} = 0$ for the gas exchange period. $Q_c" = 0$ for non-reaction flow.
- The $\frac{dU^+}{dy^+} \leq 0\; and\; y^+ > 11$ is a position where the boundary layer phenomenon is weak. If the first computation grid is within this range, increasing te near wall resolution is recommended for improving heat flux prediction.

There are several ways to compute turbulent thermal diffusivity, α_t. Algebraic models are the most commonly used in engine simulations [37, 120], where $\alpha_t = \frac{v_t}{Pr_t}$. Although turbulent viscosity, v_t, was not included in this study, the non-equilibrium method (mentioned in Chapter 2) fits the engine applications better. For the turbulent Pr number, the following model was developed by Wassel and Catton [150].

$$Pr_T = \frac{C_{p3}}{C_{p1}Pr}\left[1 - \exp\left(\frac{-C_{p4}}{\frac{v_t}{v}}\right)\right][1 - \exp(\frac{-C_{p2}}{Pr\frac{v_t}{v}})]^{-1}$$

Equation 6.12

where the coefficients are given as $C_{p1} = 0.21, C_{p2} = 5.25, C_{p3} = 0.2, and\ C_{p4} = 5.0$. The turbulent thermal diffusivity, α_t , can also be computed from Two-equation models[151, 152], which solve transport equations. The difference between Two-equation models and Algebraic models are practically non-exist for pipe/channel flow, jet flow, and the flat plate boundary layer [147]. According to the author’s knowledge, the difference between Two-equation models and algebraic models are not yet known for engine flow or periodical flow. For this study, the Wassel and Catton’s algebraic model was used because two-equation models required more near wall resolution for solving transport equations. As discussed in Chapter 2, the resolution for properly solve near wall transport equations in an engine is approaching the DNS level and fits well for LES. Using two-equation models for RANS has poor cost effectiveness.

6.3 Engine Simulation

In this study, Converge CFD package was used for engine simulation. The Renormalized $k - \varepsilon$ model was used as the turbulent model. No combustion and spray event. The simulation reproduced the PLIF-IR experimental engine conditions, where the engine motored at 1200RPM with pure nitrogen. The engine simulation contained completed engine intake systems, including surge tank and intake pipe geometry, as shown in Figure 6.1.

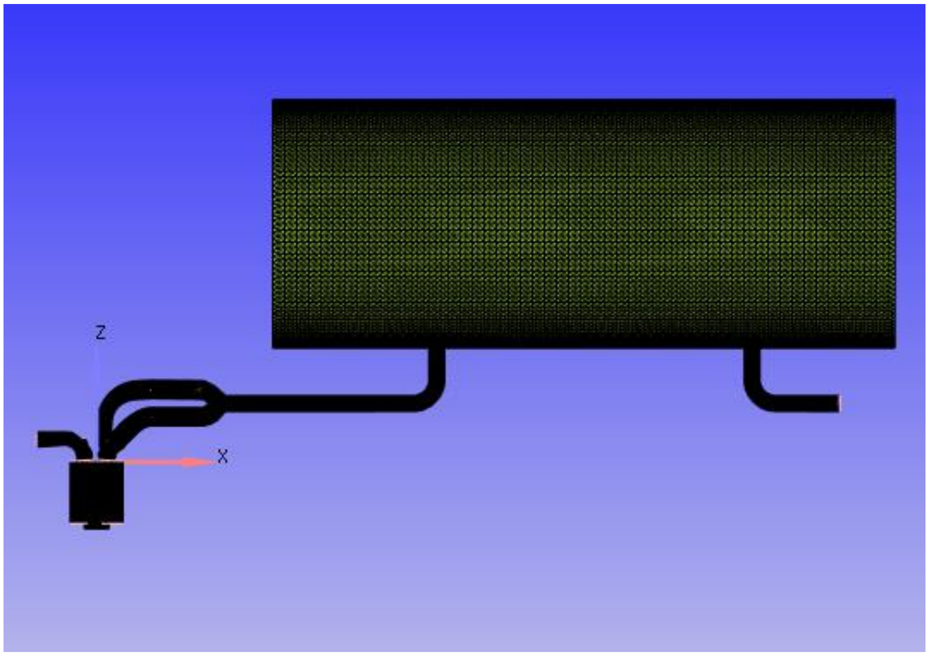

Figure 6.1: Schematic of 3D engine simulation

The geometry of the engine intake manifold, exhaust port, and fire deck were acquired by 3D scanning the actual engine head. Figure 6.2 shows the cylinder mesh geometry at BDC. To balance the computational time and reach steady results, the results from 3 continuous cycles with coarse mesh simulation results were mapped to new CFD with fine mesh as an initial condition. The coarse mesh model had 4 mm×4 mm×4 mm uniform grid size for the intake and exhaust systems, as well as 2 mm×2 mm×2 mm uniform grid size for the in-cylinder. For the fine mesh model, 2 mm×2 mm×2 mm was the base grid size for intake and exhaust systems. 1 mm×1 mm×1 mm was the base grid size for the in-cylinder with adaptive mesh refinement near the wall. The total cell number was 533,026 at TDC and 2,703,390 at BDC.

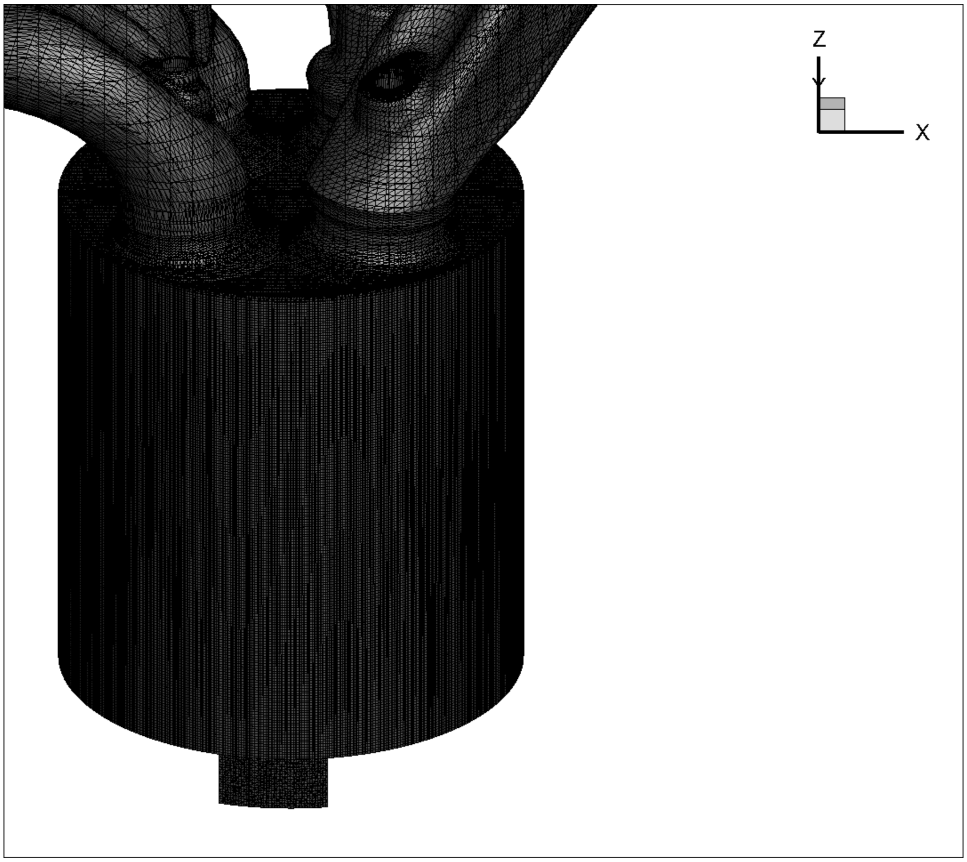

Figure 6.2: Computational mesh applied in engine simulation

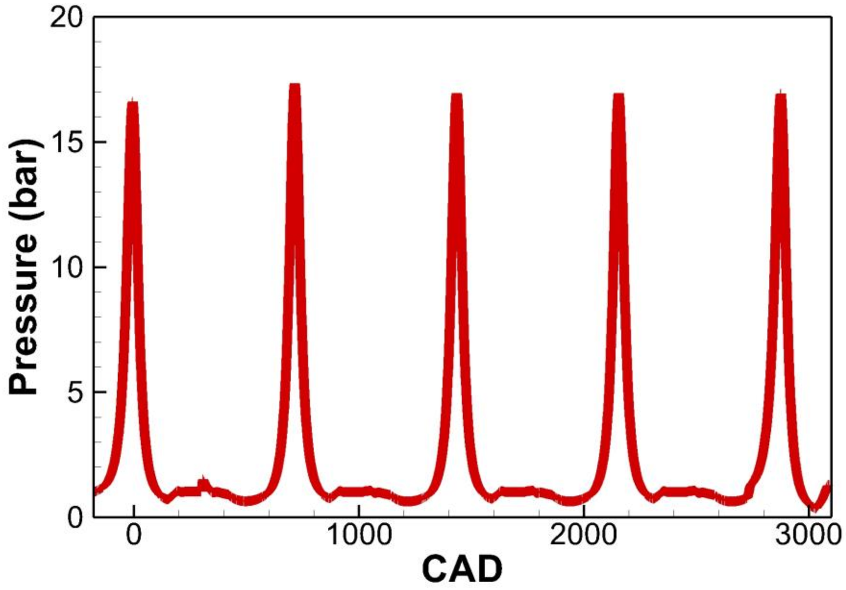

Figure 6.3: Cylinder pressure from simulation results

A total 5 continuous cycles were conducted, as shown in Figure 6.3. only the fifth cycle’s results are used for the study. A1D crevice model is used to match motoring pressure. Inlet and exhaust back flow gas temperature is tuned to 60 °C to match the motoring gas temperature. 3D engine CDF coupled with 1D conjugate heat transfer, and it is used for wall temperature prediction. Aluminum used as wall material, and 40 cell points used in 1D conjugate heat transfer at each wall-adjacent cell. The wall-back temperature was set to coolant temperature, 90 ºC (363 K).

6.4 Results and Discussion

The engine 3D simulation results were used to compare with the PLIF-IR and PIV results. In addition, turbulent parameters from the simulation results were also used for interpretation because turbulent parameters have a much shorter time scale, where present PLIF-IR and PIV techniques lack time resolution.

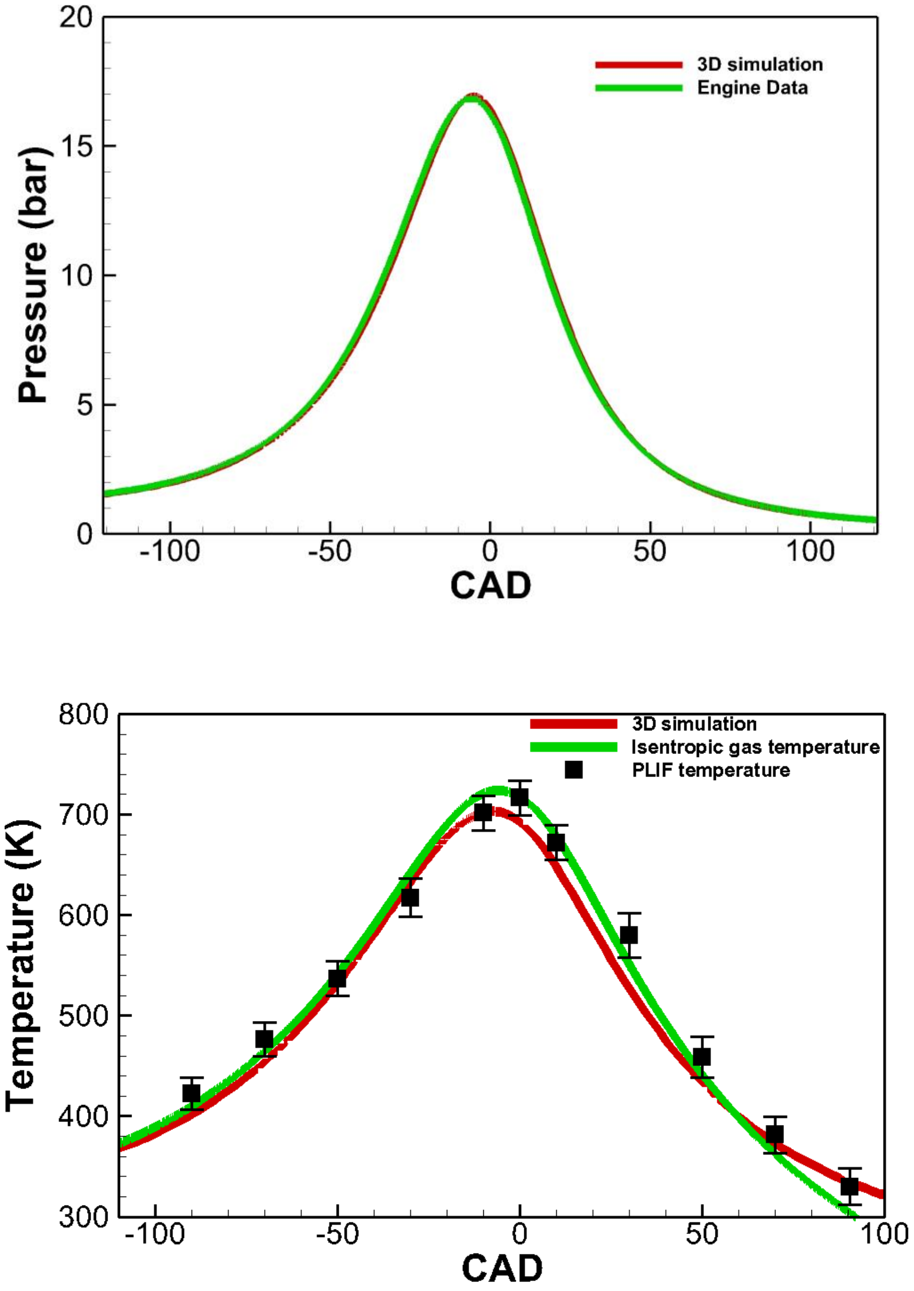

Figure 6.4: Comparison of simulated in-cylinder pressure/temperature with experimental results.

Figure 6.4 shows that simulated in-cylinder pressure and measured cylinder pressure well matched. The simulated in-cylinder gas temperature matched with both PILF measurements and isentropic gas temperature. The simulated gas temperature had better agreement with the measured temperature around TDC and later exhaust stroke. Figure 6.5 shows that the wall temperature from 1D conjugate heat transfer prediction matched the IR measurements. The cycle mean temperature difference between the prediction and IR measurement was less than 1 degree. IR measurement had an8 K max temperature swing, and the conjugate heat transfer prediction had about a 4.5 K max temperature swing.

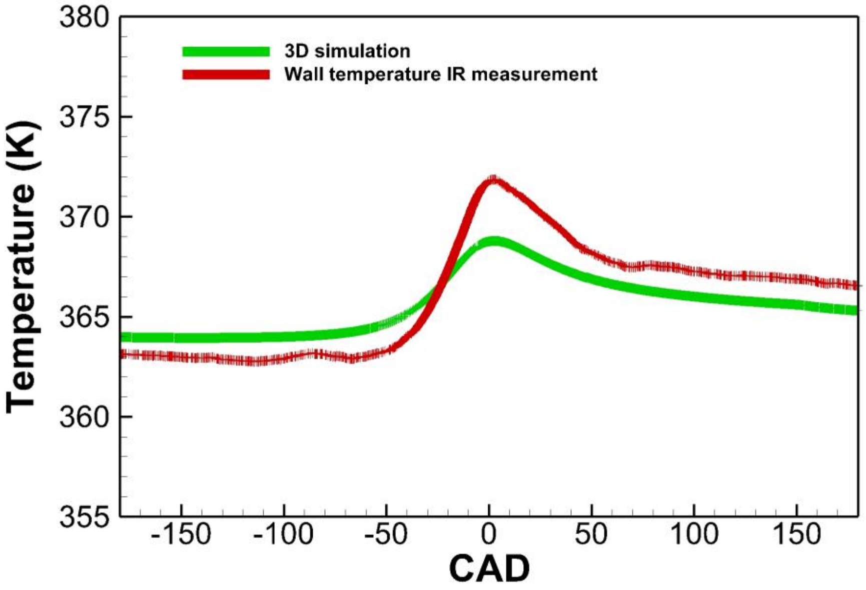

Figure 6.5: Comparison of simulated wall temperature with experimental result

Figure 6.6 shows the heat flux prediction from the 3D engine simulation with the Han and Reitz model [120]and the Angleberger model [119]. Local heat flux is calculated over an average $3\,cell \times 3\,cell$ area, which is the same place as with the PLIF-IR measurements. From the results, the Angelberger model predictions were consistently lower than those of the Han and Reitz model. The Han and Reitz model’s predictions were almost on top of experimental results during compressions, but over predicted around TDC. The Angelberger model's predictions were consistently lower than the PLIF-IR measurements. Both models predicted that the wall heat flux would substantially drop after 20 ATDC, and the direction of heat flux would reverse at 40 ATDC. Clearly, a contradiction exists in current engine simulation methods. Both measurements and simulation predictions had positive gas-to-wall temperature differences until 70 ATDC. The negative heat flux prediction around 50 ATDC was unrealistic.

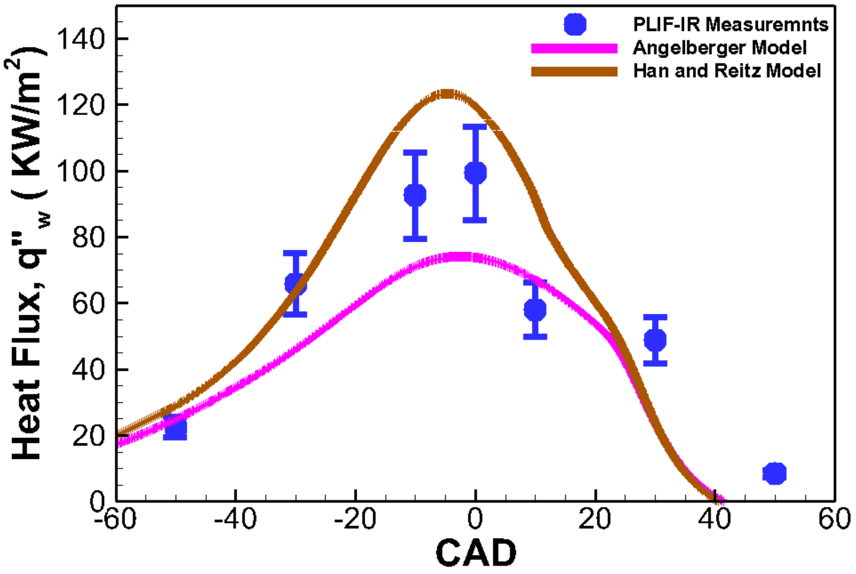

Figure 6.6: Prediction of heat flux from 3D engine simulation compared to PLIF-IR measurements

The negative heat flux prediction around 50 ATDC also had affected near temperature profile results. Figure 6.7 shows the comparison between the measurements and CFD predictions. The 3D simulated predictions well matched the near temperature profiles for y>~1mm, and the 3D simulated predictions departed away from the measured temperature profiles as y<~1mm. The renormalized $k-\varepsilon$ model was used for the present studies. No additional wall-enhanced turbulent model was applied, and poor near wall temperature profile predictions were expected. Closer to the wall, the slope of the temperature profile was steeper, and more cell points were required to resolve that slope changing, even with the wall-enhanced turbulent model. On the other hand, adding 10~20 cell points within the boundary, the average grid side was around $(50\ \mu m \sim 100\ \mu m)^3$, which fit for LES. In other words, RANS may t not be the best choice for resolving the near wall *temperature* profile in terms of cost-effectiveness. The temperature profile at 50 ATDC had a negative slope because of the negative heat flux prediction. This is certainly an artificial temperature profile, and it does not reflect any physical phenomena.

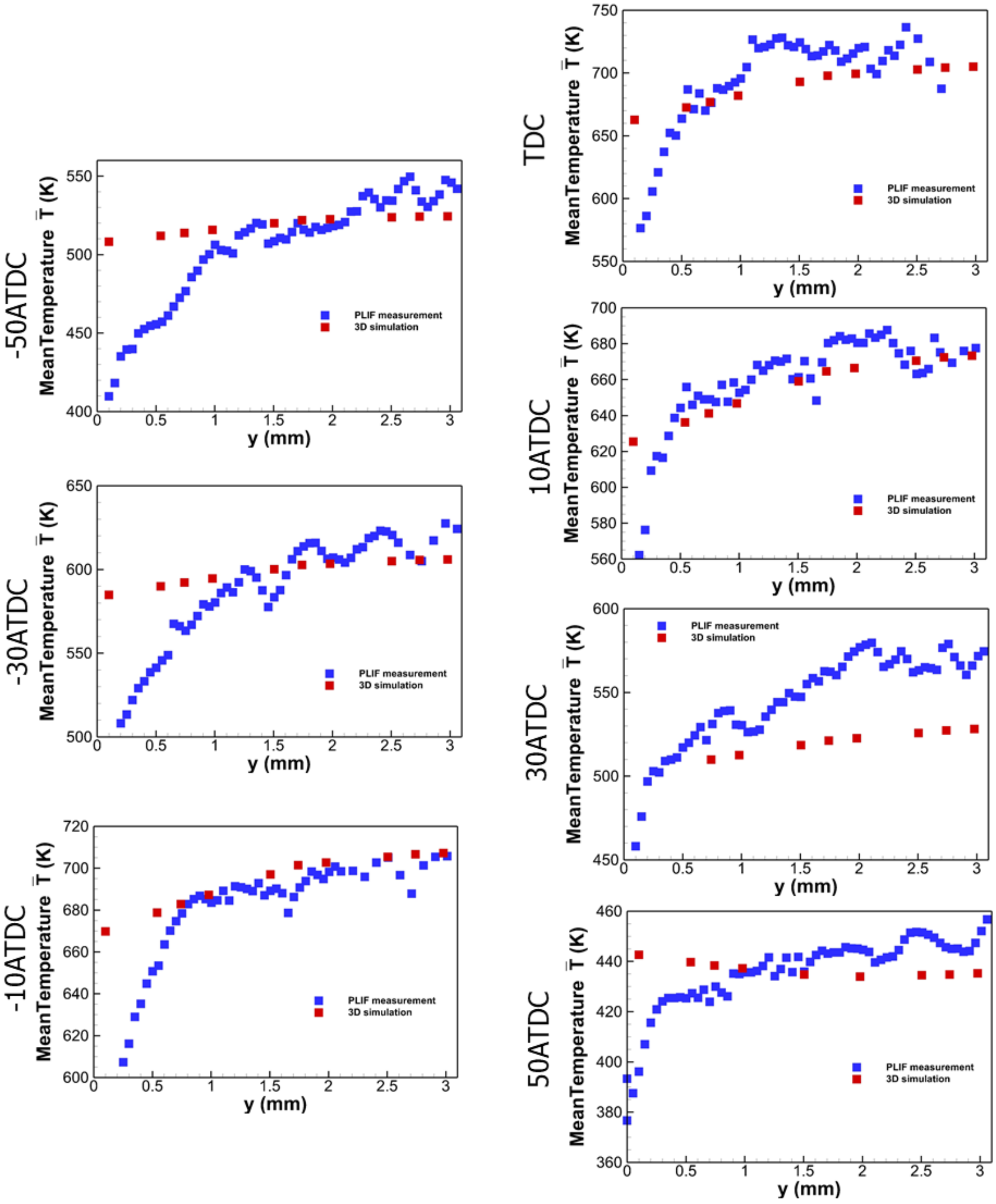

Figure 6.7: Near wall temperature profile

3D engine CDF only had an accurate temperature prediction for y>~1 mm. For y<1 mm, the CFD results were considered as invalid data and were discarded. Figure 6.8 shows the ratio between turbulent viscosity and molecular viscosity at y=1 mm away from the wall. The contradiction method was used to support the transitional boundary layer theory. The 3D engine simulation assumed a fully developed boundary layer, and 1mm was larger than the displacement thickness (shown in Chapter 5). The computed turbulent viscosity was much larger than the molecular viscosity, but the molecular viscosity still had significant effects on flow motion. This contradicted with the original assumption that the effects of molecular viscosity can be neglected in the "outer layer" of the fully developed boundary layer. In addition, the contradicted spatial average turbulent viscosity was about two magnitudes larger than the contradicted near wall turbulent viscosity. The overall turbulent intensity level was large enough to neglect the molecular viscosity effect near the center of the engine cylinder, where the boundary layer phenomenon is weak and negligible.

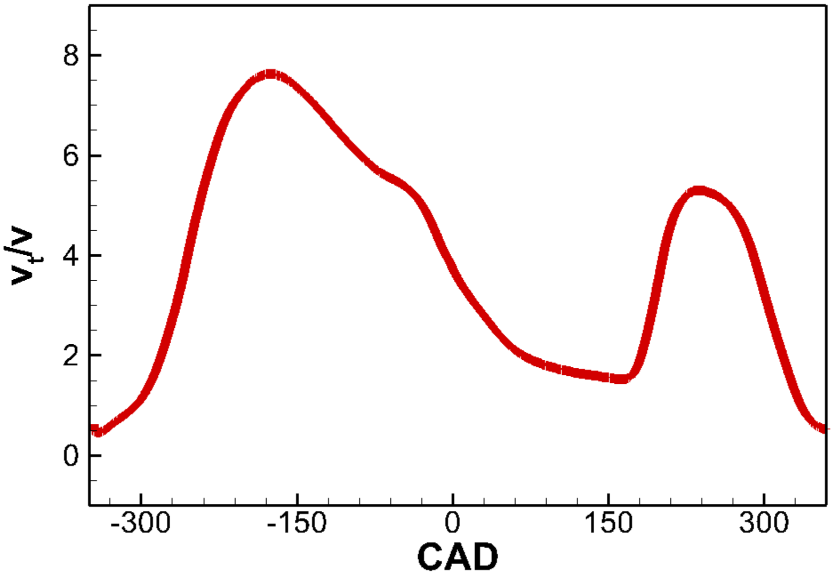

Figure 6.8:Ratio between turbulent viscosity and molecular viscosity y=1 mm away from the wall

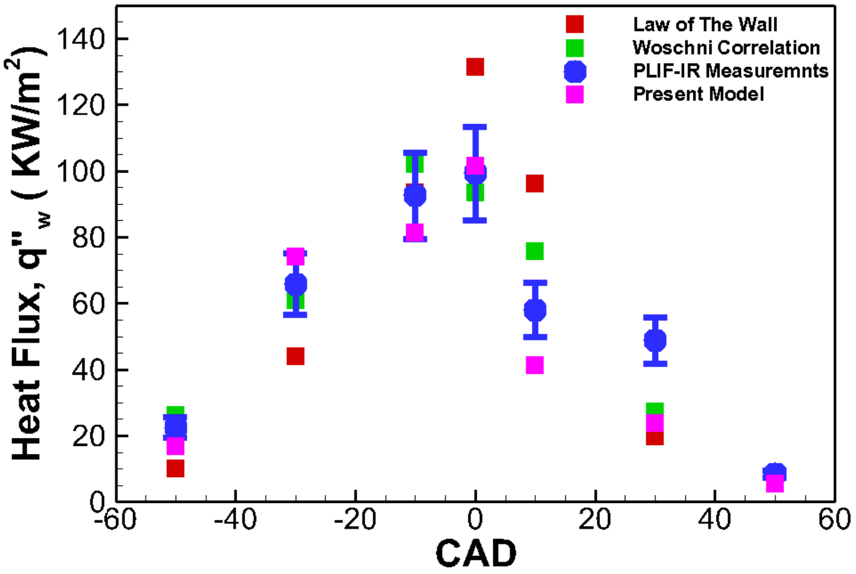

Figure 6.9: The present heat transfer model compared to experimental results and standard Law of the Wall. Both wall functions were calculated at y=1 mm.

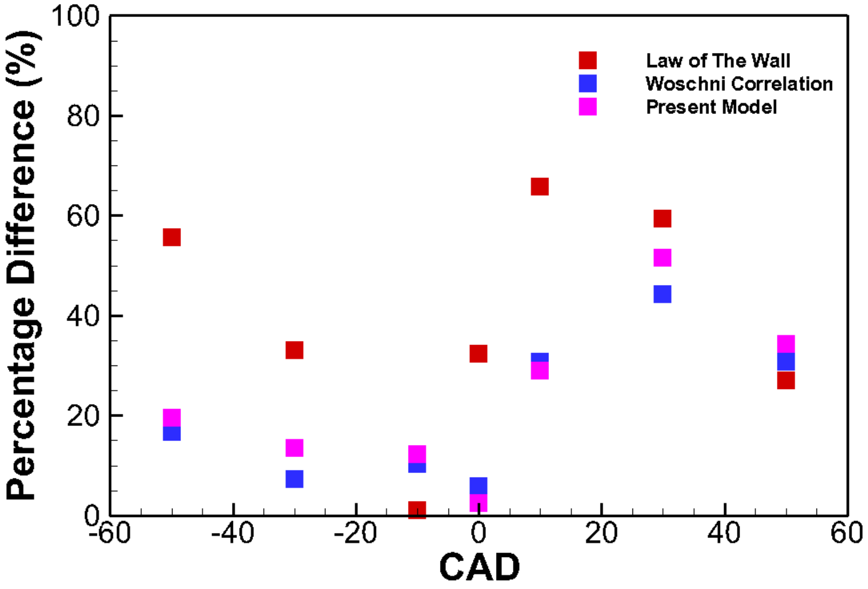

Figure 6.10: The percentage difference between model prediction and experimental measurements

Figure 6.9 shows the results from the present model. The present model had better agreement with experimental measurements compared to the standard law of the wall.

However, it still failed to predict the gas-to-wall heat transfer around 30ATDC, where the boundary layer was transitional flow. The present model assumed a constant wall temperature of, $\left.\frac{\partial T}{\partial t}\right|_{y=0} \approx 0$. For most engine motor cycles, this is a valid assumption, and the present model is expected to overpredict the heat flux for positive $\left.\frac{\partial T}{\partial t}\right|_{y=0}$, such as during combustion or the engine warm up period. This effect may be overcome by other factors, such as surface roughness and non- isochoric flow, which are not included in this study. The work done by pressure had max 20% effects on wall-function heat flux prediction around ±30 CAD, but had almost no effect at TDC because of zero piston speed and zero pressure. The pressure wave wasnot modeled in the present work, and work done by pressure had more effect during combustion, where a uniformed pressure assumption may not valid. Figure 6.10 shows the percentage difference between the model prediction and experimental measurements. The present study resulted in a relatively flat percentage difference curve during compression. This is evidence that the model coefficient can be further improved, and the method itself is valid. The challenge still exists to predict accurate heat flux when the near wall flow direction changes. The transitional boundary layer exists in the first half of the expansion stock, and all examined heat transfer models had their worst heat flux prediction within this period. This shows how strongly the transitional boundary layer affects the gas-to-wall heat transfer. However, this problem cannot be solved without a complete understanding of transition turbulence. In addition, periodical flow is a characteristic of engine flow, so engine angle velocity, ω, could be useful for further modeling.

CHAPTER 7 : CONCLUSIONS AND FUTURE WORK

7.1 In-Cylinder Wall Temperature Influence on Unburned Hydrocarbon Emissions During the Transitional Period

A laser induced phosphorescence technique is used to measure the bowl temperature and cylinder wall temperature during the warm up process in an optical engine. Experiments are performed at three TDC charge densities of 19, 21 and 24 kg/m3. Wall temperature effects on UHC and combustion phasing are determined by the simultaneous engine out UHC measurements.

During the warm up process, combustion phasing is more sensitive to bowl surface temperatures, which experience significant increases as compared to the squish zone cylinder wall temperatures. Since convection heat transfer rates are nearly scale with the in-cylinder pressure, increasing charge densities can accelerate engine heating. However, increasing in cylinder pressure has little impact on steady state temperature. The temperature difference between the piston bowl and the squish zone cylinder surface can be as large as 100 °C during the engine warm up process. However, this difference decreases after the bowl temperature reaches the steady state values since the cylinder wall temperatures rise much less rapidly than the bowl temperatures. Combustion phasing continues to advance after bowl temperatures attain steady values, indicating the influence of presumably transient thermal boundary conditions of surfaces other than in the piston bowl.

The steady state bowl temperature is 257 °C, a value very close to the critical point of the n-heptane fuel, ($T_{critical}$ for n-heptane is 267 °C). It is unknown whether the critical point or boiling point of the fuel could have an effect on steady state temperature through fuel wall impingement and subsequent evaporative cooling.

Increased bowl temperature and in-cylinder pressure can advance combustion phasing. Decreased bowl surface temperatures characterize cycles immediately flowing misfired cycles. Combustion phasing of these cycles, however, is more advanced than in the cycles immediately preceding the misfire. Thus increased reactivity, presumed to result from the availability of residual fuel of the cycle immediately flowing a misfire, dominates over the retarding effects of lower bowl surface temperatures. Although misfires occur even at elevated bowl surface temperatures, such events are more frequent at low bowl temperatures.

At the injection timing considered (-5 ATDC), squish zone cylinder wall temperature shows significant influence on engine out UHC emissions during the warm-up process. Higher surface temperatures correlate with lower levels of engine-out UHC. Moreover, the UHC emissions are more sensitive to wall temperatures at lower charge densities. Engine-out UHC is less sensitive to bowl surface temperatures, which are observed to quickly attain values nearly 100 °C greater than those measured in the squish zone. Kinetic simulations confirm that UHC concentration of rich mixtures is more sensitive to temperature than for lean mixtures, particularly when the gas temperature is in the range of 750-800 °C. Results indicate an ideal starting strategy for reducing UHC would elevate initial boost levels that decrease as engine temperatures rise.

7.2 Duel Band Infrared Diagnostic application in Optical Engine

IR diagnosis is a powerful technique for heat transfer researchers, especially when studying heat flux on hard to reach the surface. New numerical auto background noise correction two-color infrared pyrometry has been developed for engine in-cylinder surface temperature measurement. This numerical mechanism is designed to suppress relatively low-frequency background noise and provide an accurate in-cylinder surface temperature measurements with error less than 1.4% inside IC engine. The optical coating is the key for IR diagnosis application. A proper designed optical coating could reduce time delay error by 50% compared to more conventional techniques. However, the durability of the optical coating is only adequate at best. further work is needed to increase the life time of optical coating under combustion environment.

7.3 Near Wall Temperature Distribution for Engine Reciprocating Flow

A comprehensive experiment has been conducted in an optical IC engine to study gas-to-wall heat transfer. The experiment has achieved the following findings:

- A cycle averaged $\overline{Re_s}$ number has been developed for the IC engine. The cycle averaged $\overline{Re_s}$ number is capable to capture the characteristics of engine flow. Comparison and scaling between different engine flow parameters are available by matching averaged $\overline{Re_s}$ number. The Cycle averaged $\overline{Re_s}$ number also can establish a link between engine experiments and foundational experiments.
- Both fully developed turbulent and transitional flows have been found existing in engine flow. This fits the description of intermittent turbulent, but it is far

different than the original fully developed turbulent assumption, which is/was? used in almost all engine simulation.

- Turbulence temperature fluctuation, T', was less than 6% around TDC for a motor engine.
- For a "motor" engine, the constant wall temperature assumption, $T_w = canstant\ and\ \frac{dT_w}{dt} = 0$, was valid for most engine cycles, except in the -50 ATDC to TDC period, where the rate of wall temperature variation, $\frac{dT_w}{dt}$, reached 2000 K/s under the present engine condition, and the solid wall was not able to transfer the gas-to-wall energy away quick enough .
- A cold turbulence structure existed around 50 ATDC to 70 ATDC., which can cause strong cycle-to-cycle variation. The gas temperature was highly non-uniform during this period. Although there is a lack of experimental support, the divergent flow is believed to be the cause of cold gas formation.
- The non-dimensional Woschni correlation had an overall good agreement with the experimental results. The predicted heat flux has less than 50% percent of error.
- The standard law of the wall provided a reasonable heat flux prediction. During the compression stroke, the standard law of the wall under predicted the heat flux because of the compression effect. Around TDC the standard law of the wall over predicted the heat flux because of transitional flow effects. Compared to experimental results, the standard law of the wall had a maximum of 64% percent

of the difference at 10 ATDC, where the in-cylinder flow direction changed around the 10 ATDC to 20 ATDC period.

7.4 Multi Zone Heat Transfer Model

A multi zone engine heat transfer model is proposed. The model coefficient can be further improved by future work. The present model had improved heat flux prediction during the compression stroke to TDC, and it has potential to improve heat flux prediction for later expansion stroke. The multi zone mechanism is used to capture engine boundary layer characteristics, where the traditional two zone mechanism may cause more error.

A 3D engine simulation model was completed and conducted to study near wall turbulent heat transfer. A contradiction method was used to further prove traditional boundary layer, where traditional engine simulation always assumes fully developed turbulent boundary layer. The effects of viscous and heat conduction cannot be neglected during the TDC~30 ATDC period.

The temperature profiles from simulation results had good agreement with PILF measurements for y>1 mm. The simulated temperature profile started to depart from measurement at 1mm. The heat flux predictions from the simulation results had reasonable agreement with PILF measurements, except after 40 ATDC, where the predicted heat flux dropped below zero with a positive gas to wall temperature difference. The numerical error is believed to be the reason, but further refining near wall resolution would lose the advantage of RANS.

All the examined models failed to predict accurate heat flux around 10 ATDC to 40 ATDC. The primary reason is transitional flow effects. The transitional flow was formed because of flow dictation period changes, and engine flow had a low stock Re number, which fits in the intermediate turbulent flow stock Re number range. Effective thermal conduction cannot be neglected, even in the “outer layer” of the boundary layer. Future studies are needed to solve the heat flux in the transitional flow.

7.5 Future Work

The possible future works include the following:

- In-cylinder optical coating has been proved useful for engine research. Increasing the durability of the in-cylinder optical coating has value. An optimized contact surface structure has been reported to increase the life time of surface coating, and it has the potential to increase the durability of the in-cylinder optical coating.
- A catadioptric optical system could potentially increase the accuracy of IR measurements. The current optical set does not fully reveal the potential of the IR technique.
- To resolve heat flux in transitional flow, three physical phenomena need to be understood. Transitional flow had several stages and paths to fully developed turbulence (probability more than we know), and each stage has its own characteristic. It is unclear how the engine flows progress to each stage. Turbulent thermal diffusivity profile in period flow would improve heat flux prediction. Currently, only a flat plate or a jet flow is available, and it does not fit engine

applications. The near wall chemical reaction is also a key to predicting heat flux during combustion, and heat transfer during combustion is the most important part of future engine heat transfer study.

APPENDIX: NOMENCLATURE

Table 1A: Nomenclature.

q'' : heat flux	τ: shear stress
k: thermal conductivity	ρ: fluid density
$\bar{T}$: time mean temperature	$< U >$: average of velocity
t: time	V： volume
h: convection coefficient	Re: Reynolds number
A,B,C: model coefficients	Re$_s$: Stokes’ Reynolds number
ϵ: measurement uncertainty	Re$_L$: Turbulence Reynolds number
σ: the Stefan-Boltzmann constant	Pr, Pr$_t$: molecular and turbulence Prandtl number
ε : emissivity	P: pressure
c_m: mean piston speed	c$_p$: specific heat at constant pressure
y: coordinate normal to the wall	y$^+$: distance in wall units
α: thermal diffusivity	δ_v: viscous length-scale
St: Stanton number	u_τ: friction velocity
u^+: dimensionless velocity	θ^+: dimensionless temperature
θ: temperature difference	T$_\tau$: wall conduction temperature
$f(y^+)$, $f_1\left(\frac{y}{\delta}\right), f_2(\frac{u_\tau\delta}{v})$: velocity profile functions in term of inner layer units, outer layer units, and intermediary units.	$g(y^+), g_1\left(\frac{y}{\delta}\right), g_2\left(\frac{u_\tau\delta}{v}\right)$: temperature profile functions in term of inner layer units, outer layer units, and intermediary units.
ƙ: Karman constant	c_f: skin friction coefficient
U_∞: free steam velocity	T_∞: core temperature
v, v$_t$: molecular and turbulence viscosity number	E^* : an empirical constant
C_μ: a model constant for turbulent viscosity	Ƥ$_k$: production of kinetic energy
η: outer layer units	ζ: intermediate units
$\mathcal{k}_p$: turbulent kinetic energy	ϵ: dissipation rate
$< u'v' >$: Reynolds stress vector	$< T'v' >$: turbulent heat flux vector
W_p: work done by pressure	Q_c : heat released/absorbed by chemical reactions
ω: angle velocity	T’: turbulence temperature fluctuation
V’: turbulence velocity fluctuation	α$_t$: turbulence thermal diffusivity
γ: the specific heat ratio.	S$_0$, S$_1$,: ground stage and excited stage
$\phi(\lambda,T)$: quantum yield	δ_T, and δ_T^*: boundary layer thickness and thermal displacement

PREVIOUS PUBLICATIONS

- Luo, X., Yu, X., Zha, K., Jansons, M. et al., "In-Cylinder Wall Temperature Influence on Unburned Hydrocarbon Emissions During Transitional Period in an Optical Engine Using a Laser-Induced Phosphorescence Technique," SAE Int. J. Engines 7(2):995-1002, 2014, doi:10.4271/2014-01-1373.
- Luo, X., Yu, X., and Jansons, M., "Simultaneous In-Cylinder Surface Temperature Measurements with Thermocouple, Laser-induced Phosphorescence, and Dual Wavelength Infrared Diagnostic Techniques in an Optical Engine," SAE Technical Paper 2015-01-1658, 2015, doi:10.4271/2015-01-1658.
- Yu, X., Luo, X., Jansons, M., Kim, D. et al., "A Fuel Surrogate Validation Approach Using a JP-8 Fueled Optically Accessible Compression Ignition Engine," SAE Int. J. Fuels Lubr. 8(1):119-134, 2015, doi:10.4271/2015-01-0906.
- Yu, X., Zha, K., Luo, X., Taraza, D. et al., "Simulation and Experimental Measurement of CO2*, OH* and CH2O* Chemiluminescence from an Optical Diesel Engine Fueled with n-Heptane," SAE Technical Paper 2013-24-0010, 2013, doi:10.4271/2013-24-0010.

REFERENCES

1. *Energy Consumption by Sector*. 2015 [cited 2016 Sept. 11]; Available from: http://www.eia.gov/totalenergy/data/monthly/pdf/sec2_3.pdf.
2. Dunn, D.R., *Monthly Energy Review July 2016*, U.S.D.o. Energy, Editor. 2016: Washington, DC
3. Jörg Kühlwein, J.G., and Anup Bandivadekar. *Global passenger vehicle standards*. 2015; Available from: http://www.theicct.org/info-tools/global-passenger-vehicle-standards.
4. Heywood, J., *Internal Combustion Engine Fundamentals*. 1988: McGraw-Hill Education.
5. Borman, G. and K. Nishiwakit, *Internal-combustion engine heat transfer*. Progress in Energy and Combustion Science, 1987. **13**(1): p. 1-46.
6. Fitch, J. *The Effects of Temperature on Lubricants*. industrial lubricants 2007 [cited 2016; Available from: http://www.machinerylubrication.com/Read/993/oil-egg.
7. Ezekoye, O., R. Greif, and R.F. Sawyer. *Increased surface temperature effects on wall heat transfer during unsteady flame quenching*. in *Proceedings of the 24th International Symposium On Combustion, July 5, 1992 - July 10, 1992*. 1992. Sydney, Engl: Publ by Combustion Inst.
8. Cleary, D.J. and P.V. Farrell. *The effects of wall temperature on flame structure during flame quenching*. in *1994 SAE International Congress and Exposition,*

February 28, 1994 - March 3, 1994. 1994. Detroit, MI, United states: SAE International.

9. LeFeuvre, T., P.S. Myers, and O.A. Uyehara, *Experimental Instantaneous Heat Fluxes in a Diesel Engine and Their Correlation*. 1969, SAE International.

10. Gingrich, E., J. Ghandhi, and R.D. Reitz, *Experimental Investigation of Piston Heat Transfer in a Light Duty Engine Under Conventional Diesel, Homogeneous Charge Compression Ignition, and Reactivity Controlled Compression Ignition Combustion Regimes.* SAE Int. J. Engines, 2014. **7**(1): p. 375-386.

11. Benajes, J., et al., *An Investigation of Radiation Heat Transfer in a Light-Duty Diesel Engine.* SAE International Journal of Engines, 2015. **8**(5): p. 2199-2212.

12. Chen, C. and A. Veshagh, *A One-Dimensional Model for In-Cylinder Heat Convection Based on the Boundary Layer Theory*. 1992, SAE International.

13. Borgnakke, C., V.S. Arpaci, and R.J. Tabaczynski, *A Model for the Instantaneous Heat Transfer and Turbulence in a Spark Ignition Engine*. 1980, SAE International.

14. Jenkin, R.J., E.H. James, and W.M. Malalasekera, *Modelling Near Wall Temperature Gradients in "Motored" Spark Ignition Engines*. 1996, SAE International.

15. Annand, W.J.D., *Heat transfer in cylinders of reciprocating internal combustion engines.* Institution of Mechanical Engineers -- Proceedings, 1963. **177**(36): p. 973-996.

16. Woschni, G. *A universally applicable equation for the instantaneous heat transfer coefficient in the internal combustion engine*. 1967. SAE International.

17. Jackson, N.S., A.D. Pilley, and N.J. Owen, *Instantaneous Heat Transfer in a Highly Rated DI Truck Engine*. 1990, SAE International.

18. Chang, J., et al., *New Heat Transfer Correlation for an HCCI Engine Derived from Measurements of Instantaneous Surface Heat Flux*. 2004, SAE International.

19. Hohenberg, G.F., *Advanced Approaches for Heat Transfer Calculations*. 1979, SAE International.

20. George, W.K. and L. Castillo, *Zero-pressure-gradient turbulent boundary layer.* Appl. Mech.

Rev., 1997: p. 50.

21. Fujita, H., *Fully developed turbulent flow and heat transfer in a square duct with two roughened facing walls.* Chemical Engineering Communications, 1988. **74**(1): p. 95-110.

22. Long, R.R. and T.-C. Chen, *Experimental evidence for the existence of the 'mesolayer' in turbulent systems.* Journal of Fluid Mechanics, 1981. **105**: p. 19-59.

23. Afzal, N., *Fully developed turbulent flow in a pipe: an intermediate layer.* Ingenieur-Archiv, 1982. **52**(6): p. 355-77.

24. Afzal, N., *Mesolayer theory for turbulent flows.* AIAA Journal, 1984. **22**(3): p. 437-439.

25. Gersten, K., *Hermann Schlichting and the Boundary-Layer Theory*, in *Hermann Schlichting – 100 Years: Scientific Colloquium Celebrating the Anniversary of His Birthday, Braunschweig, Germany 2007*, R. Radespiel, C.-C. Rossow, and B.W. Brinkmann, Editors. 2009, Springer Berlin Heidelberg: Berlin, Heidelberg. p. 3-17.

26. George, W.K. and L. Castillo, *Zero-Pressure-Gradient Turbulent Boundary Layer.* Applied Mechanics Reviews, 1997. **50**(12): p. 689-729.

27. Tollmien, W., et al., *Zur turbulenten Strömung in Rohren und längs Platten*, in *Ludwig Prandtl Gesammelte Abhandlungen: zur angewandten Mechanik, Hydro- und Aerodynamik*, F.W. Riegels, Editor. 1961, Springer Berlin Heidelberg: Berlin, Heidelberg. p. 632-648.

28. Karman, T.v., *Mechanische Ähnlichkeit und Turbulenz, nach Ges.* Wiss. Gottingen. Math. Physik. Klasse, 1930.

29. Von Karman, T., *Mechanische Ahnlichkeit und Turbulenz*, D. National Advisory Committee for Aeronautics; Washington, United States, Editor. Mar 01, 1931, Germany.

30. Coles, D., *The young person's guide to the data*. 1968, DTIC Document.

31. Kader, B.A. and A.M. Yaglom, *Heat and mass transfer laws for fully turbulent wall flows.* International Journal of Heat and Mass Transfer, 1972. **15**(12): p. 2329-51.

32. Nagib, H., et al. *Can we ever rely on results from wall-bounded turbulent flows without direct measurements of wall shear stress?* in *24th AIAA Aerodynamic*

Measurement Technology and Ground Testing Conference 2004, June 28, 2004 - July 1, 2004. 2004. Portland, OR, United states: American Institute of Aeronautics and Astronautics Inc.

33. Zagarola, M.V. and A.J. Smits, *Mean-flow scaling of turbulent pipe flow*. Journal of Fluid Mechanics, 1998. **373**: p. 33-79.

34. George, W.K., *Is there a universal log law for turbulent wall-bounded flows?* Philosophical Transactions of the Royal Society of London A: Mathematical, Physical and Engineering Sciences, 2007. **365**(1852): p. 789-806.

35. Squire, H.B., *The friction temperature: A useful parameter in heat-transfer analysis*. Heat Transfer, 1951: p. 185-186.

36. Tamilporai, P., et al., *Simulation and Analysis of Combustion and Heat Transfer in Low Heat Rejection Diesel Engine Using Two Zone Combustion Model and Different Heat Transfer Models*. 2003, SAE International.

37. Park, H.J., D.N. Assanis, and D. Jung, *Development of an In-Cylinder Heat Transfer Model with Compressibility Effects on Turbulent Prandtl Number, Eddy Viscosity Ratio and Kinematic Viscosity Variation*. 2009, SAE International.

38. Jennings, M.J. and T. Morel, *A Computational Study of Wall Temperature Effects on Engine Heat Transfer*. 1991, SAE International.

39. Liu, Z., et al., *3-D Numerical Simulation of Transient Heat Transfer among Multi-Component Coupling System in Internal Combustion Chamber*. 2008, SAE International.

40. Puzinauskas, P. and C. Borgnakke, *Evaluation and Improvement of an Unsteady Heat Transfer Model for Spark Ignition Engines*. 1991, SAE International.

41. Wang, X., L. Castillo, and G. Araya, *Temperature Scalings and Profiles in Forced Convection Turbulent Boundary Layers.* Journal of Heat Transfer, 2008. **130**(2): p. 021701-021701.

42. Ebadi, A., F. Mehdi, and C.M. White, *An exact integral method to evaluate wall heat flux in spatially developing two-dimensional wall-bounded flows.* International Journal of Heat and Mass Transfer, 2015. **84**: p. 856-861.

43. Zagarola, M.V., A.E. Perry, and A.J. Smits, *Log laws or power laws: The scaling in the overlap region.* Physics of Fluids, 1997. **9**(7): p. 2094-2100.

44. Mckeon, B.J., et al., *Further observations on the mean velocity distribution in fully developed pipe flow*. Journal of Fluid Mechanics, 2004. **501**: p. 135-147.

45. Cheng, W. and R. Samtaney, *Power-law versus log-law in wall-bounded turbulence: A large-eddy simulation perspective.* Physics of Fluids, 2014. **26**(1): p. 011703.

46. Wosnik, M., L. Castillo, and W.K. George, *A theory for turbulent pipe and channel flows.* Journal of Fluid Mechanics, 2000. **421**: p. 115-145.

47. George, W.K., *Recent advancements toward the understanding of turbulent boundary layers.* AIAA journal, 2006. **44**(11): p. 2435-2449.

48. Wei, T., et al., *Properties of the mean momentum balance in turbulent boundary layer, pipe and channel flows.* Journal of Fluid Mechanics, 2005. **522**: p. 303-27.

49. Churchill, S.W. and C. Chan, *Turbulent flow in channels in terms of local turbulent shear and normal stresses.* AIChE Journal, 1995. **41**(12): p. 2513-2521.

50. Reynolds, O., *On the Extent and Action of the Heating Surface for Steam Boilers.* Manchester, 1874. **14**: p. 7–12.

51. Blasius, H., *Grenzschichten in Flüssigkeiten mit kleiner Reibung*. 1907: Druck von BG Teubner.

52. Colburn, A.P., *A method of correlating forced convection heat-transfer data and a comparison with fluid friction.* International Journal of Heat and Mass Transfer, 1964. **7**(12): p. 1359-1384.

53. Bons, J., *A Critical Assessment of Reynolds Analogy for Turbine Flows.* Journal of Heat Transfer, 2005. **127**(5): p. 472-485.

54. Vigdorovich, I.I., *New formulations of the temperature defect law for turbulent boundary layers on a plate.* International Journal of Heat and Mass Transfer, 2015. **84**: p. 653-659.

55. Liu, J.T.C., *An extended Reynolds analogy for excited wavy instabilities of developing streamwise vortices with applications to scalar mixing intensification.* Proceedings of the Royal Society A: Mathematical, Physical and Engineering Science, 2007. **463**(2083): p. 1791-1813.

56. T. Wang, J.C. and S.F. Shen, *Unsteady Boundary Layers with Flow Reversal and the Associated Heat-Transfer Problem.* AIAA Journal, 1978. **16**(10): p. 1025-1029.

57. Ma, P.C., et al., *Development and Analysis of Wall Models for Internal Combustion Engine Simulations Using High-speed Micro-PIV Measurements.* Flow, Turbulence and Combustion, 2016: p. 1-27.

58. Raghunathan, B.D. and R.G. Kenny. *CFD simulation and validation of the flow within a motored two-stroke engine*. in *International Congress and Exposition, February 24, 1997 - February 27, 1997*. 1997. Detroit, MI, United states: SAE International.

59. Schlichting, H., et al., *Boundary-layer theory*. Vol. 7. 1960: Springer.

60. Chapman, D.R., *Computational Aerodynamics Development and Outlook.* AIAA Journal, 1979. **17**(12): p. 1293-1313.

61. and, U.P. and E. Balaras, *WALL-LAYER MODELS FOR LARGE-EDDY SIMULATIONS.* Annual Review of Fluid Mechanics, 2002. **34**(1): p. 349-374.

62. Barenblatt, G.I., *Scaling laws for fully developed turbulent shear flows. Part 1. Basic hypotheses and analysis.* Journal of Fluid Mechanics, 1993. **248**: p. 513-520.

63. Cipra, B., *A New Theory of Turbulence Causes a Stir Among Experts.* Science, 1996. **272**(5264): p. 951-951.

64. OBERLACK, M., *A unified approach for symmetries in plane parallel turbulent shear flows.* Journal of Fluid Mechanics, 2001. **427**: p. 299-328.

65. Michael Frewer, G.K., Holger Foysi, *Is the log-law a first principle result from Lie-group invariance analysis* ArXiv e-prints, 2014.

66. Jainski, C., et al., *High-speed micro particle image velocimetry studies of boundary-layer flows in a direct-injection engine.* International Journal of Engine Research, 2013. **14**(3): p. 247-259.

67. Moffat., W.M.K.B.F.B.a.R.J., *The turbulent boundary layer on a porous plate: an experimental study of the heat transfer behavior with adverse pressure gradients*. 1972.

68. Kong, H., H. Choi, and J.S. Lee, *Dissimilarity between the velocity and temperature fields in a perturbed turbulent thermal boundary layer.* Physics of Fluids, 2001. **13**(5): p. 1466-1479.

69. Launder, B.E. and D. Spalding, *The numerical computation of turbulent flows.* Computer methods in applied mechanics and engineering, 1974. **3**(2): p. 269-289.

70. Schmitt, F.G., *About Boussinesq's turbulent viscosity hypothesis: historical remarks and a direct evaluation of its validity.* Comptes Rendus Mécanique, 2007. **335**(9-10): p. 617-627.

71. Absi, R., *A simple eddy viscosity formulation for turbulent boundary layers near smooth walls.* Comptes Rendus Mécanique, 2009. **337**(3): p. 158-165.

72. Viegas, J., M. Rubesin, and C. Horstman, *On the use of wall functions as boundary conditions for two-dimensional separated compressible flows.* AIAA paper, 1985. **180**: p. 1985.

73. *FLUENT 6.3 User's Guide* 12.10.2 Standard Wall Functions [cited 2016; Available from: https://www.sharcnet.ca/Software/Fluent6/html/ug/node512.htm.

74. Jayatilleke, C.L.V., *The influence of Prandtl number and surface roughness on the resistance of the laminar sub-layer to momentum and heat transfer*. 1966, University of London.

75. Reitz, R.D., *Assessment of wall heat transfer models for premixed-charge engine combustion computations*. 1991, SAE Technical Paper.

76. Jenkin, R., E. James, and W. Malalasekera, *Modelling near wall temperature gradients in" motored" spark ignition engines.* 1996.

77. Rakopoulos, C.D. and E.G. Giakoumis, *Study of the transient operation of low heat rejection turbocharged diesel engine including wall temperature oscillations*. 2007, SAE Technical Paper.

78. Kim, S.-E. and D. Choudhury, *A near-wall treatment using wall functions sensitized to pressure gradient.* Separated and complex flows- 1995, 1995: p. 273-280.

79. Dronniou, N. and J.E. Dec, *Investigating the Development of Thermal Stratification from the Near-Wall Regions to the Bulk-Gas in an HCCI Engine with Planar Imaging Thermometry.* SAE International Journal of Engines, 2012. **5**(3): p. 1046-1074.

80. Bendersky, D., *Special thermocouple for measuring transient temperatures.* Mechanical Engineering, 1953. **75**(2): p. 117-121.

81. Assanis, D.N., et al., *A Prototype Thin-Film Thermocouple for Transient Heat Transfer Measurements in Ceramic-Coated Combustion Chambers*. 1990, SAE International.

82. Wimmer, A., R. Pivec, and T. Sams, *Heat Transfer to the Combustion Chamber and Port Walls of IC Engines - Measurement and Prediction*. 2000, SAE International.

83. Terzis, A., et al., *Thermocouple thermal inertia effects on impingement heat transfer experiments using the transient liquid crystal technique.* Measurement Science & Technology, 2012. **23**(11): p. 115303 (13 pp.).

84. Towle, L.C. and C.J. Burkitt. *Some effects of low frequency interference when using thermocouples for industrial temperature measurement*. in *Conference on electrical interference in instrumentation, 9-11 June 1970*. 1970. London, UK: IEE.

85. Chan, K.W. and C.K. Chou, *Use of thermocouples in the intense fields of ferromagnetic implant hyperthermia.* International Journal of Hyperthermia, 1993. **9**(6): p. 831-48.

86. Chakraborty, D.P. and I.A. Brezovich, *Error sources affecting thermocouple thermometry in RF electromagnetic fields.* Journal of Microwave Power, 1982. **17**(1): p. 17-28.

87. Feist, J.P., et al. *Phosphor thermometry for high temperature gas turbine applications*. in *Instrumentation in Aerospace Simulation Facilities, 1999. ICIASF 99. 18th International Congress on*. 1999.

88. Knappe, C., et al., *Laser-Induced Phosphorescence and the Impact of Phosphor Coating Thickness on Crank-Angle Resolved Cylinder Wall Temperatures.* SAE Int. J. Engines, 2011. **4**(1): p. 1689-1698.

89. Feist, J., et al. *Phosphor thermometry for high temperature gas turbine applications*. in *Instrumentation in Aerospace Simulation Facilities, 1999. ICIASF 99. 18th International Congress on*. 1999. IEEE.

90. Allison, S., et al., *Development of temperature-sensitive paints for high-temperature aeropropulsion applications*, in *37th Joint Propulsion Conference and Exhibit*. 2001, American Institute of Aeronautics and Astronautics.

91. Bielaczyc, P., J. Merkisz, and J. Pielecha, *Investigation of Exhaust Emissions from DI Diesel Engine During Cold and Warm Start*. 2001, SAE International.

92. Heywood, J.B., *Internal combustion engine fundamentals*. 1988: New York : McGraw-Hill, [1988] ©1988.

93. Krauss, R.H., R. Hellier, and J.C. McDaniel, *Surface temperature imaging below 300 K using La 2 O 2 S: Eu.* Applied optics, 1994. **33**(18): p. 3901-3904.

94. Eckbreth, A.C., *Laser diagnostics for combustion temperature and species*. Vol. 3. 1996: CRC Press.

95. Cates, M., *YAG: Dy and YAG: Tm Fluorescence Above 1400 C*. 2003, ORNL.

96. Colban, W.F., et al., *A detailed comparison of emissions and combustion performance between optical and metal single-cylinder diesel engines at low temperature combustion conditions.* SAE International Journal of Fuels and Lubricants, 2008. **1**(2008-01-1066): p. 505-519.

97. Shionoya, S., W.M. Yen, and H. Yamamoto, *Phosphor handbook*. 2006: CRC press.

98. Knappe, C., et al., *Laser-induced phosphorescence and the impact of phosphor coating thickness on crank-angle resolved cylinder wall temperatures.* SAE International Journal of Engines, 2011. **4**(2011-01-1292): p. 1689-1698.

99. Kim, D., et al., *In-cylinder CO and UHC imaging in a light-duty diesel engine during PPCI low-temperature combustion.* SAE International Journal of Fuels and Lubricants, 2008. **1**(2008-01-1602): p. 933-956.

100. Borman, G. and K. Nishiwaki, *Internal-combustion engine heat transfer.* Progress in energy and combustion science, 1987. **13**(1): p. 1-46.

101. Bendersky, D.A., *A Special Thermocouple for Measuring Transient Temperatures.* Mechanical Engineering, 1953. **75**: p. 117-121.

102. Biddulph, P., et al., *Inferring the thermal resistance and effective thermal mass of a wall using frequent temperature and heat flux measurements.* Energy and Buildings, 2014. **78**: p. 10-16.

103. Kozarek, R.L. *Effect of case temperature measurement errors on the junction-to-case thermal resistance of a ceramic PGA*. in *1991 Seventh Annual IEEE Semiconductor Thermal Measurement and Management Symposium, 12-14 Feb. 1991*. 1991. New York, NY, USA: IEEE.

104. Steinberg, A.M., et al. *Diagnostic requirements for the development of low-emission, fuel-flexible gas turbine combustors*. in *50th AIAA Aerospace Sciences Meeting Including the New Horizons Forum and Aerospace Exposition, January 9, 2012 - January 12, 2012*. 2012. Nashville, TN, United states: American Institute of Aeronautics and Astronautics Inc.

105. Agnew, W.C., *End-gas temperature measurement by two-wavelength infrared radiation method.* Society of Automotive Engineers -- Journal, 1960. **68**(10): p. 62-67.

106. Childs, P.R.N., J.R. Greenwood, and C.A. Long, *Review of temperature measurement.* Review of Scientific Instruments, 2000. **71**(8): p. 2959-2978.

107. Khan, M.A., C. Allemand, and T.W. Eagar, *Noncontact temperature measurement. I. Interpolation based techniques.* Review of scientific instruments, 1991. **62**(2): p. 392-402.

108. Maldague, X. and M. Dufour, *Dual imager and its applications to active vision robot welding, surface inspection, and two-color pyrometry.* Optical engineering, 1989. **28**(8): p. 288872-288872-.

109. Crane, K. and P.J. Beckwith, *IR radiation pyrometer*. 1984, Google Patents.

110. Eyal, O. and A. Katzir, *Temperature measurements utilizing two-bandpass fiber optic radiometry.* OPTICAL ENGINEERING-BELLINGHAM-INTERNATIONAL SOCIETY FOR OPTICAL ENGINEERING-, 1995. **34**: p. 470-470.

111. *The HITRAN 2004 molecular spectroscopic database.* Journal of Quantitative Spectroscopy & Radiative Transfer, 2005. **96**.

112. Gatowski, J., et al., *Heat release analysis of engine pressure data*. 1984, SAE Technical paper.

113. Marr, M.A., et al., *A fast response thermocouple for internal combustion engine surface temperature measurements.* Experimental Thermal and Fluid Science, 2010. **34**(2): p. 183-189.

114. Spalvins, T. and W.A. Brainard, *Nodular growth in thick-sputtered metallic coatings.* Journal of Vacuum Science and Technology, 1974. **11**(6): p. 1186-1192.

115. Zhang, D.-P., et al., *Defect-induced failure of optical coating filters.* Optics & Laser Technology, 2006. **38**(8): p. 654-657.

116. Tench, R.J., R. Chow, and M.R. Kozlowski, *Characterization of defect geometries in multilayer optical coatings.* Proceedings of SPIE - The International Society for Optical Engineering, 1994. **2114**: p. 415-425.

117. Kaiser, N., et al., *High damage threshold Al2O3SiO2 dielectric coatings for excimer lasers.* Thin Solid Films, 1995. **260**(1): p. 86-92.

118. Singh, A.P., S. Gadekar, and A.K. Agarwal, *In-Cylinder Air-Flow Characteristics Using Tomographic PIV at Different Engine Speeds, Intake Air Temperatures and Intake Valve Deactivation in a Single Cylinder Optical Research Engine*. 2016, SAE International.

119. Angelberger, C., T. Poinsot, and B. Delhay, *Improving Near-Wall Combustion and Wall Heat Transfer Modeling in SI Engine Computations*. 1997, SAE International.

120. Han, Z. and R.D. Reitz, *A temperature wall function formulation for variable-density turbulent flows with application to engine convective heat transfer modeling.* International journal of heat and mass transfer, 1997. **40**(3): p. 613-625.

121. Einecke, S., et al., *Two-Dimensional Temperature Measurements in an SI Engine Using Two-Line Tracer LIF*. 1998, SAE International.

122. Einecke, S., C. Schulz, and V. Sick, *Measurement of temperature, fuel concentration and equivalence ratio fields using tracer LIF in IC engine combustion.* Applied Physics B: Lasers and Optics, 2000. **71**(5): p. 717-723.

123. Fujikawa, T., et al., *2-D Temperature Measurements of Unburned Gas Mixture in an Engine by Two-line Excitation LIF Technique*. 2006, SAE International.

124. Koban, W., et al., *Absorption and fluorescence of toluene vapor at elevated temperatures.* Physical chemistry chemical physics, 2004. **6**(11): p. 2940-2945.

125. Zha, K., et al., *Characterization of Flow Asymmetry During the Compression Stroke Using Swirl-Plane PIV in a Light-Duty Optical Diesel Engine with the Re-entrant Piston Bowl Geometry.* SAE International Journal of Engines, 2015. **8**(4): p. 1837-1855.

126. Schlichting, H., et al., *Boundary-layer theory*. Vol. 7. 1955: Springer.

127. Alharbi, A.Y. and V. Sick, *Investigation of boundary layers in internal combustion engines using a hybrid algorithm of high speed micro-PIV and PTV.* Experiments in fluids, 2010. **49**(4): p. 949-959.

128. Menter, F.R., *Improved two-equation k-omega turbulence models for aerodynamic flows.* 1992.

129. Akhavan, R., R. Kamm, and A. Shapiro, *An investigation of transition to turbulence in bounded oscillatory Stokes flows Part 1. Experiments.* Journal of Fluid Mechanics, 1991. **225**: p. 395-422.

130. Akhavan, R., R. Kamm, and A. Shapiro, *An investigation of transition to turbulence in bounded oscillatory Stokes flows Part 2. Numerical simulations.* Journal of fluid mechanics, 1991. **225**: p. 423-444.
131. Ozdemir, C.E., T.-J. Hsu, and S. Balachandar, *Direct numerical simulations of transition and turbulence in smooth-walled Stokes boundary layer*. Physics of Fluids, 2014. **26**(4): p. 045108.
132. Pond, I., *Toward an Understanding of the Breakdown of Heat Transfer Modeling in Reciprocating Flows.* 2015.
133. Ebadi, A., et al. *Flow structure in self-sustaining and intermittently turbulent reciprocating channel flow*. in *APS Meeting Abstracts*. 2016.
134. Jensen, B., B. Sumer, and J. Fredsøe, *Turbulent oscillatory boundary layers at high Reynolds numbers.* Journal of Fluid Mechanics, 1989. **206**: p. 265-297.
135. Kays, W.M., *Turbulent Prandtl number—where are we?* Journal of Heat Transfer, 1994. **116**(2): p. 284-295.
136. Lee, J. and P.V. Farrell, *Intake Valve Flow Measurements of an IC Engine Using Particle Image Velocimetry*. 1993, SAE International.
137. Mythealias. *Schematic of laser-induced fluorescence*. 12 May 2013 [cited 2017 8]; Available from: https://commons.wikimedia.org/wiki/File:Laser-induced_fluorescence.png.
138. Chu, T., W. Ranson, and M.A. Sutton, *Applications of digital-image-correlation techniques to experimental mechanics.* Experimental mechanics, 1985. **25**(3): p. 232-244.

139. Miles, P.C., et al., *The Evolution of Flow Structures and Turbulence in a Fired HSDI Diesel Engine*. 2001, SAE International.

140. Dronniou, N. and J.E. Dec, *Investigating the development of thermal stratification from the near-wall regions to the bulk-gas in an HCCI engine with planar imaging thermometry*. SAE International Journal of Engines, 2012. **5**(2012-01-1111): p. 1046-1074.

141. Köpple, F., et al., *Experimental Investigation of Fuel Impingement and Spray-Cooling on the Piston of a GDI Engine via Instantaneous Surface Temperature Measurements.* SAE International Journal of Engines, 2014. **7**(3): p. 1178-1194.

142. Pope, S.B., *Turbulent flows*. 2001, IOP Publishing.

143. Chapman, D.R., *Computational aerodynamics development and outlook.* AIAA J, 1979. **17**(12): p. 1293-1313.

144. Piomelli, U., et al., *The inner–outer layer interface in large-eddy simulations with wall-layer models.* International Journal of Heat and Fluid Flow, 2003. **24**(4): p. 538-550.

145. Amsden, A.A., P. O'rourke, and T. Butler, *KIVA-II: A computer program for chemically reactive flows with sprays*. 1989, Los Alamos National Lab., NM (USA).

146. Borman, G. *at the UW Engine Research Center*. in *International Symposium C0M0DIA*. 1990.

147. Yoder, D.A. *Comparison of Turbulent Thermal Diffusivity and Scalar Variance Models*. in *54th AIAA Aerospace Sciences Meeting*. 2016.

148. Ma, P.C., et al., *Development and analysis of wall models for internal combustion engine simulations using high-speed micro-PIV measurements.* Flow, Turbulence and Combustion, 2017. **98**(1): p. 283-309.

149. Ma, P., et al. *Analysis of Wall Models for Internal Combustion Engine Simulations Using High-speed Micro-PIV Measurements*. in *APS Meeting Abstracts*. 2014.

150. Wassel, A. and I. Catton, *Calculation of turbulent boundary layers over flat plates with different phenomenological theories of turbulence and variable turbulent Prandtl number.* International Journal of Heat and Mass Transfer, 1973. **16**(8): p. 1547-1563.

151. Sommer, T., R. So, and H. Zhang, *Near-wall variable-Prandtl-number turbulence model for compressible flows.* AIAA journal, 1993. **31**(1): p. 27-35.

152. Wilcox, D.C., *Comparison of two-equation turbulence models for boundary layers with pressure gradient.* AIAA journal, 1993. **31**(8): p. 1414-1421.

ABSTRACT

STUDY OF PERIODICAL FLOW HEAT TRANSFER IN AN INTERNAL COMBUSTION ENGINE

by

XI LUO

December 2017

Advisor: Dr. Marcis Jansons

Major: Mechanical Engineering

Degree: Doctor of Philosophy

In-cylinder heat transfer is one of the most critical physical behaviors which has a direct influence on engine out emission and thermal efficiency for IC engine. In-cylinder wall temperature has to be precisely controlled to achieve high efficiency and low emission. However, this cannot be done without knowing gas-to-wall heat flux. This study reports on the development of a technique suitable for engine in-cylinder surface temperature measurement, as the traditional method is “hard to reach.” A laser induced phosphorescence technique was used to study in-cylinder wall temperature effects on engine out unburned hydrocarbons during the engine transitional period (warm up). A linear correlation was found between the cylinder wall surface temperature and the unburned hydrocarbons at mediate and high charge densities. At low charge density, no clear correlation was observed because of miss-fire events. A new auto background

correction infrared (IR) diagnostic was developed to measure the instantaneous in-cylinder surface temperature at 0.1 CAD resolution. A numerical mechanism was designed to suppress relatively low-frequency background noise and provide an accurate in-cylinder surface temperature measurements with an error of less than 1.4% inside the IC engine. In addition, a proposed optical coating reduced time delay errors by 50% compared to more conventional thermocouple techniques. A new cycle-averaged $\overline{\mathrm{Re}_s}$ number was developed for an IC engine to capture the characteristics of engine flow. Comparison and scaling between different engine flow parameters are available by matching the averaged $\overline{\mathrm{Re}_s}$ number. From experimental results, the engine flow motion was classified as intermittently turbulent, and it is different from the original fully developed turbulent assumption, which has previously been used in almost all engine simulations. The intermittent turbulence could have a great impact on engine heat transfer because of the transitional turbulence effect. Engine 3D CFD model further proves the existence of transitional turbulence flow. A new multi zone heat transfer model is proposed for IC engines only. The model includes pressure work effects and improved heat transfer prediction compared to the standard Law of the wall model.

AUTOBIOGRAPHICAL STATEMENT

XI LUO

- 1988, Born in Wuhan, P.R. China
- 2004-2007, Attended Shiyan High School, Wuhan, P.R. China
- 2007-2012, B.S. in Mechanical Engineering, University of Nevada, Reno, NV2, USA.
- 2012-2014, M.S. in Mechanical Engineering, Way State University, Detroit, MI, USA.
- 2014-2017, PhD. in Mechanical Engineering, Way State University, Detroit, MI, USA.